G^0 Spectrometer Magnetic and Optical Design

R. M. Laszewski

UIUC/NPL Technical Report 93-02, 30 October, 1993

1 Introduction
- 1.1 Spectrometer Design Goals
- 1.2 Toroidal Spectrometer-Configuration
- 1.3 Overview of Optics Considerations
  - 1.3.1 Conventional Focus: $(x \mid \theta) = 0$
  - 1.3.2 Zero Magnification: $(x \mid x) = 0$
  - 1.3.3 Forward-Proton vs. Backward-Electron Measurements

2 Optics Design and Optimization
- 2.1 Optimization Criteria
  - 2.1.1 Dipole Fields
  - 2.1.2 Ideal-Toroid Field Approximation
  - 2.1.3 Modified-Gaussian Field Approximation
- 2.2 Realistic Fields
  - 2.2.1 Normal vs. Super-Conducting Options
  - 2.2.2 Normal-Conducting Spectrometer Optimization
  - 2.2.3 Super-Conducting Spectrometer Optimization

3 Expected Performance
- 3.1 Description of the Proposed Spectrometer
- 3.2 Magnetic Field and Trajectory Computations
- 3.3 Focal Surface
- 3.4 Optics Characterization
  - 3.4.1 Proton Optics
  - 3.4.2 Electron Optics
- 3.5 Acceptances and Collimation
- 3.6 Fringe Fields
- 3.7 Magnetic Forces
- 3.8 Alignment & Deflection Tolerances
- 3.9 Beam Motion & Rastering
- 3.10 Current Stability Requirements
- 3.11 Extended Q^2-range: Forward Protons

4 Summary

5 References

G^0 Spectrometer Magnetic and Optical Design

R. M. Laszewski

UIUC/NPL Technical Report 93-02, 30 October, 1993

1. Introduction

We have proposed a measurement of parity-violating electron scattering asymmetries at both forward and backward angles in the range $0.1 < Q^2 < 0.5$ GeV^2 in order to separate the elastic flavor singlet charge and magnetic form factors, G^0_E and G^0_M [PR92]. The asymmetries are expected to be between about 3×10^{-6} and 3×10^{-5}, and statistical and helicity-correlated systematic uncertainties need to be held to $\Delta A/A \sim 5\%$, and $\Delta A < 2.5 \times 10^{-7}$ respectively. A specialized spectrometer system is required to achieve the desired precision in a reasonable period of time.

1.1. Spectrometer Design Goals

Either elastically scattered electrons or the corresponding recoil protons could be detected and used for the forward- and backward-angle asymmetry measurements. In the case of the forward measurement, the electrons are at small angles and have very high energies. This can imply significant experimental difficulties with backgrounds, spectrometer and beam-line geometry, and detector shielding. By contrast, the corresponding forward-proton kinematics are much more tractable as can be seen from Table 1. For the backward-angle measurements, Table 2 shows that the electron kinematics can be chosen so that the fore (proton) and aft (electron) scattering-angles are roughly symmetric with respect to 90°, at ~70° and ~110° respectively. This permits a spectrometer to have the same orientation relative to the entrance beam line for the backward measurement as it does to the exit beam line for the forward

Table 1. Forward Proton Kinematics

Q^2 (GeV^2/c^2)	$E_0 = 3.0$ (GeV)	P_p (MeV/c)	θ_p
0.1		320.7	77.4°
0.2		459.7	72.3°
0.3		570.6	68.4°
0.4		667.4	65.2°
0.5		755.6	62.4°

Table 2. Backward Electron Kinematics

Q^2 (GeV^2/c^2)	E_0 (GeV)	P_e (MeV/c)	$\theta_e = 110°$ ($\equiv 70°$)
0.1	-	-	
0.2	0.335	226	
0.3	0.428	265	
0.4	0.512	295	
0.5	0.590	320	

measurement. In particular, an axially symmetric detector system can simply be turned front-to-back to accommodate the two sets of measurements.

In addition to having the appropriate kinematic range, a number of requirements for an optimal G^0 spectrometer arise from the need for good counting statistics, from the presence of competing inelastic processes, and from the importance of limiting systematic errors. These can be summarized:

i) Extended target capability:	Nominal 20-cm target length
ii) Very high counting rates:	Trajectory reconstruction precluded
iii) Line-of-sight shielding:	Sets the minimum bend-angle
iv) Large azimuthal acceptance:	Maximum possible fraction of 2π
v) Modest resolution:	$1\% < \Delta Q^2/Q^2 < 10\%$
vi) Systematic error control:	Axial-symmetric particle detection B = 0 at cryo-target Iron-free environment

1.2. Toroidal Spectrometer-Configuration

Many of the features that are listed in the previous section as being desirable for the G^0 experiment can be realized with a toroidal spectrometer. The large acceptance arising from a relatively unobstructed geometry, and the intrinsic axial symmetry of a toroid are particularly attractive. In addition, there need be no iron return yokes or pole faces, and the magnetic field is negligible near the axis where the target is located. Also, a toroidal spectrometer will allow both the

forward proton and the backward electron measurements to be made with the same instrumentation.

Cost considerations imply that super-conducting coils are probably the most reasonable means by which to realize a device of this kind. Although, as will be discussed in Section 2.2, the initial fabrication expenditure can be greater for a super-conducting device than for a normal one, it is clear that operating costs will be very much lower for the former in the context of realistic estimates of the utilization and lifetime of the spectrometer. This consideration becomes even more important if, as is likely, there are additional experiments and programs for which a toroid might be found to be useful. The extension of the backward (and perhaps forward) measurements to much higher Q^2 and the possibility of out-of-plane coincidence measurements come readily to mind [La91b], [CD90], [ST89].

1.3. Overview of Optics Considerations

1.3.1. Conventional Focus: $(x \mid \theta) = 0$.

For a point target, excellent focal behavior (i.e. momentum dispersion along a focal plane with $(x \mid \theta) \sim 0$) can be achieved with a toroid. However, there are two important reasons why this optical configuration is less than optimal for the proposed G^0 measurements. First, for a toroid, the $(x \mid \theta) = 0$ focus has rather bad extended target (t) characteristics, particularly at larger scattering angles. In a typical example, a matrix element $(x \mid t) \sim 8$ compares with a dispersion $(x \mid \delta) \sim 3$ cm/%, so that a 20-cm target length would translate into a momentum uncertainty of about 50%. In general, the resolution required by the experiments would preclude the use of a long target. The second difficulty with $(x \mid \theta) = 0$ optics involves a limitation on the configuration of the spectrometer. Because the magnetic fields of a toroid decrease with increasing radius over most of its useful volume, except for very limited kinematic ranges, the $(x \mid \theta) = 0$ condition can be achieved external to the toroid only if the particle trajectories are bent outward, away from the symmetry axis. This results in a spectrometer with very long focal surfaces, situated at large radii. Also, relatively more coil is required to provide an outward than an inward bend-angle that is adequate for line-of-sight shielding.

These considerations argue that a conventional optical configuration is not particularly appropriate for the proposed G^0 experiment.

1.3.2. Zero Magnification: $(x \mid x) = 0$.

By basing the optical design of the toroidal spectrometer on a zero-magnification condition, it is possible to avoid many of the problems that are associated with employing a conventional focus. By definition, long targets are easily accommodated if $(x \mid x) = 0$ (zero magnification). Then, in general, both $(x \mid \delta)$ and $(x \mid \theta)$ will be non-zero. This permits the design of a spectrometer that disperses the kinematic variable Q^2 directly along the physical focal-surface. Every point on the focal surface defined by the zero-magnification condition will correspond to a family of coordinate pairs (p, θ). If the detectors can measure both position and time-of-flight, then both p and θ can be uniquely determined for non-relativistic particles. In fact, simple plastic-scintillators can provide the necessary position and timing information, at very high event rates, for the proposed proton experiment. It is also important to recognize that, unlike the conventional focusing toroid, a zero-magnification toroidal spectrometer can be configured to bend the particles of interest inward, toward the symmetry axis. This permits the construction of a more compact spectrometer, with a much smaller over-all area of focal surface to be instrumented and shielded.

We note that the backward electrons are more nearly relativistic than are the forward protons, and that time-of-flight measurements will be of little use in determining θ for the backward experiment. However, the electron momentum resolution only needs to be sufficient to separate the elastic scattering from the inelastic electrons associated with pion production. As will be discussed in Sections 3.4.2 and 3.5, this resolution can be obtained by using collimation to define the scattering-angle acceptance of the spectrometer. Such a restriction on the backward θ-acceptance might appear to present something of a disadvantage with respect to what could be achieved with an $(x \mid \theta) = 0$ optical configuration; but in fact, the effects of geometric aberrations always put a limit on the angular acceptance of the latter as well. When the shorter target-length and the real scattering-angle acceptance associated with a simply-instrumented conventional-focusing toroid are considered, it is likely that both the conventional device and one configured for zero magnification would require similar amounts of running time to make comparable sets of backward measurements. These issues are discussed again in Section 3.4.2.

Table 3. Extended Backward Electron Kinematics

Q^2 (GeV^2/c^2)	E_0 (GeV)	P_e (MeV/c)	$\theta_e = 110°$ ($\equiv 70°$)
1.0	0.395	401	
2.0	1.547	482	
3.0	2.125	526	
4.0	2.686	555	

We conclude that the $(x|x) = 0$ optical configuration is very advantageous for high counting rates, long targets, the reduction of backgrounds with particle time-of-flight, and the minimization of spectrometer cost. We consider zero-magnification optics to be particularly suitable for the proposed G^0 measurements.

1.3.3. Forward-Proton vs. Backward-Electron Measurements

The forward-proton measurements make the greatest demands on the spectrometer design. There are three reasons for this. First, the proton momenta are substantially larger than those of the electrons at corresponding values of Q^2 as can be seen from a comparison of Tables 1 and 2. An implicit consequence of this kinematic asymmetry is that it will be possible to extend the backward measurements to much higher Q^2 than the 0.5 GeV^2/c^2 proposed for the forward measurement. Examples of kinematics for this option are given in Table 3, and it will be discussed below in Section 3.4.2. Second, the forward measurement demands better intrinsic kinematic resolution than is required by the backward measurement. This can be seen from Table 4 which compares $\frac{\partial p}{\partial Q^2}$ and $\frac{\partial \theta}{\partial Q^2}$ for the proton and electron experiments. The relative change in θ for a given change in Q^2 is an order of magnitude greater for the backward-electrons than it is for the forward-protons. We note that, because a restriction of the scattering-angle acceptance with collimation is used to provide the necessary backward momentum-resolution, the possibility of trading a somewhat larger angular-acceptance for the backward measurement against the forward resolution-requirement does not drive the optimization of the spectrometer. These issues will be examined in more quantitative detail in Section 3.4.2.

Table 4. Kinematic Sensitivity to Changes in Q^2.
(Forward protons and backward electrons)

	$\frac{\partial p}{\partial Q^2}$ (GeV/c)/(GeV/c)^2		$\frac{\partial \theta}{\partial Q^2}$ degree/(GeV/c)^2	
Q^2	proton	electron	proton	electron
0.3	1.05	-0.53	-34.5	434.8
0.4	0.91	-0.53	-29.4	344.8
0.5	0.83	-0.53	-26.3	294.1

Third, competing background-processes in the forward direction are more problematic than those in the backward, and tend to define the overall demands for count-rate, resolution, and line-of-sight shielding.

The only electron-specific demands that are made on the optimization of the $(x \mid x) = 0$ spectrometer are that the $(x \mid \delta)$ matrix element be made as relatively large, and the $(x \mid \theta)$ as relatively small as is reasonably consistent with the more stringent set of demands made on the proton optimization.

2. Optics Design and Optimization

2.1. Optimization Criteria

The geometry and magnetic fields of a toroidal spectrometer are not easily visualized. Examined in the familiar context of dipole magnets, all of the fields of a toroid tend to look like fringe fields. For this reason, we begin a discussion of the criteria used in the optimization of the G^0-spectrometer design by first considering in Section 2.1.1 the general characteristics of a dipole spectrometer configured to meet the required $(x \mid x) = 0$ optical condition. Then, the performance-optimization of a zero-magnification toroidal spectrometer is examined in two different approximations in Sections 2.1.2 and 2.1.3. The fundamental differences between normal- and super-conducting realizations of the spectrometer are discussed in Section 2.2.1, and, for purposes of comparison, a reference normal-conducting design is examined in Section 2.2.2. Finally, the detailed modeling and optimization of a realistic super-conducting toroid for the G^0 experiment is presented in Section 2.2.3. The expected

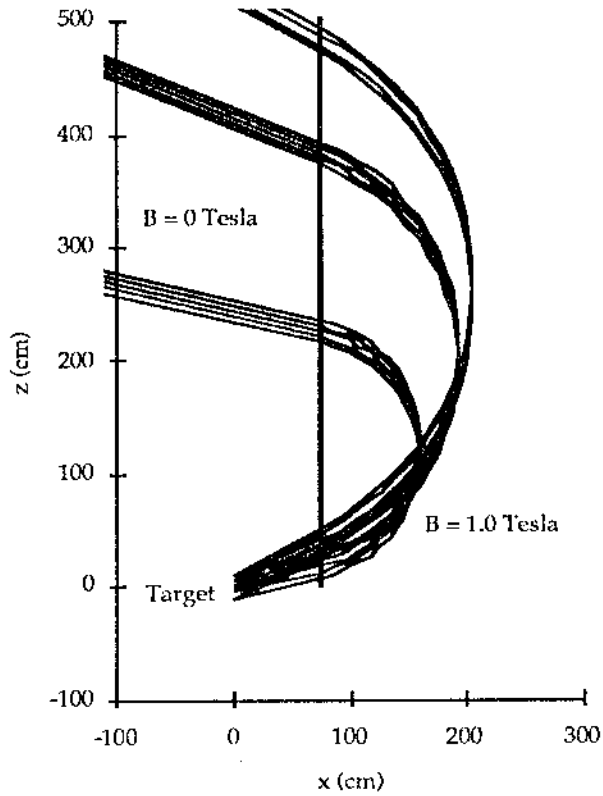

Figure 1. Proton trajectories corresponding to $Q^2 = 0.1$, 0.3, and 0.5 GeV^2 from a 20-cm long target entering an uniform 1.0-Tesla dipole field. Note the zero-magnification foci.

performance of the G^0 spectrometer will be discussed in Section 3 of this document.

2.1.1 Dipole Fields

In lowest order, zero magnification is a consequence of a magnetic field distribution that is invariant with respect to translation along the length of the target. This can be seen in Figure 1 which plots the trajectories of protons that emerge from a 20-cm long target and enter a region with a constant magnetic field of B = 1.0 Tesla which is oriented in a direction normal to the plane of the figure. The rays reflect proton momenta, p, and scattering angles, θ, corresponding to $Q^2 = 0.1$, 0.3, and 0.5 GeV^2/c^2. Note that the maximum bend angle that can be achieved for an $(x \mid x) = 0$ focus is $\theta_{bend} = \theta$. It can be shown

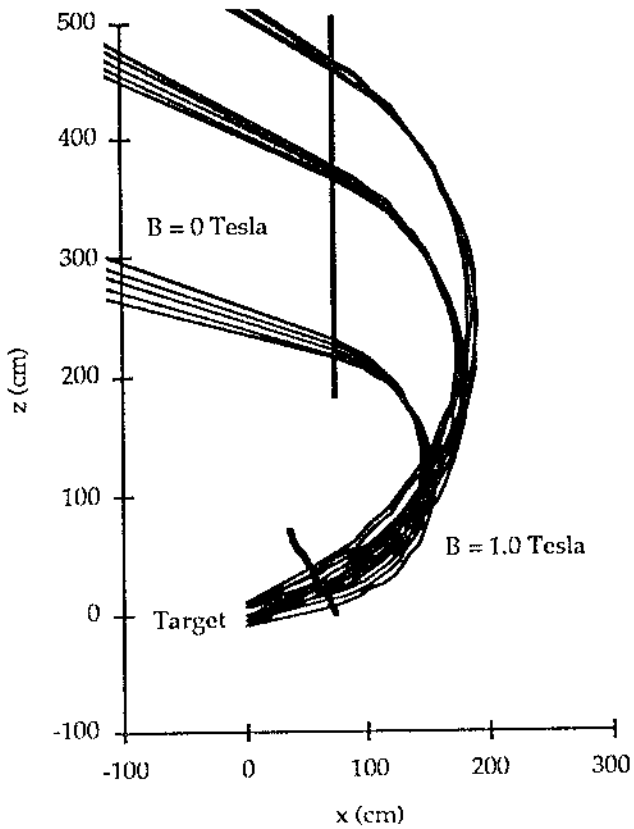

Figure 2. Proton trajectories corresponding to $Q^2 = 0.1$, 0.3, and 0.5 GeV^2 from a 20-cm long target entering an uniform 1.0-Tesla dipole field. The entrance-edge is rotated by 30°.

that for a target of length Δ, the dispersion and the intrinsic momentum resolution are respectively

$$(x|\delta) \approx (.0334)\cdot\left(\frac{p(\mathrm{MeV}/c)}{B(\mathrm{kG})}\right)\cdot(1-\cos\theta) \qquad (\mathrm{cm}/\%) \qquad (1)$$

and

$$\frac{\Delta p}{p} \approx \frac{(1.12)}{(1-\cos\theta)}\cdot\Delta^2(\mathrm{cm}^2)\cdot\left(\frac{B(\mathrm{kG})}{p(\mathrm{MeV}/c)}\right)^2 \qquad (\%) \qquad (2).$$

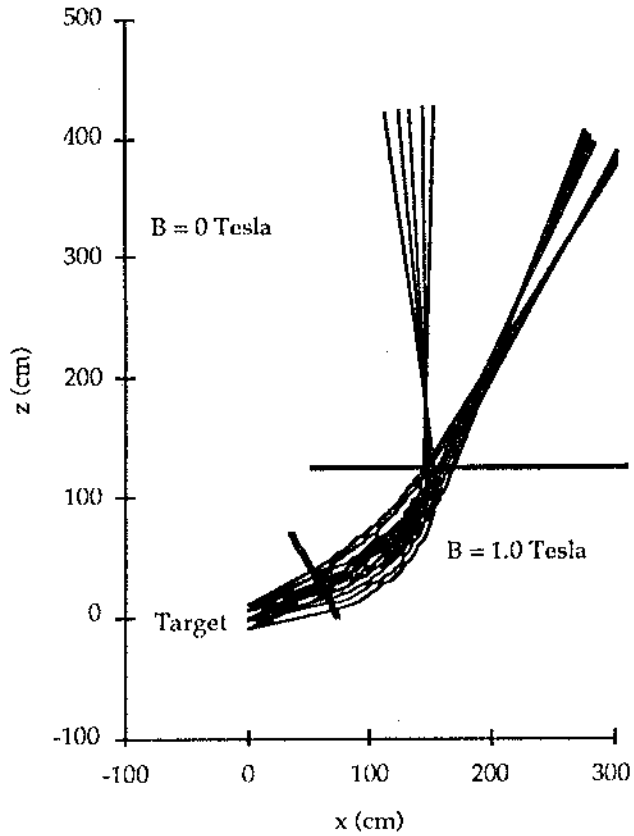

Figure 3. Proton trajectories corresponding to $Q^2 = 0.1$, 0.3, and 0.5 GeV^2 from a 20-cm long target entering an uniform 1.0-Tesla dipole field. The extent of the constant field region is reduced relative to that shown in Figure 2.

High fields are not an advantage for resolution, but they reduce the size of the spectrometer which scales with the bending radius, $R = (3.34)p/B$. Figure 1 shows that respective focal-points tend to lie very close to trajectories of particles with higher relative momentum. However, an entrance edge rotation can be used to move the focal plane outward and also to increase the Q^2 dispersion. This can be seen from a comparison of the trajectories of Figure 2 with those of Figure 1.

As the extent of the area with non-zero field is reduced, the focal surface moves outside of the boundaries of the magnet. Both the Q^2 dispersion and the deflection angle of the trajectories are also reduced significantly. These effects are illustrated in Figure 3.

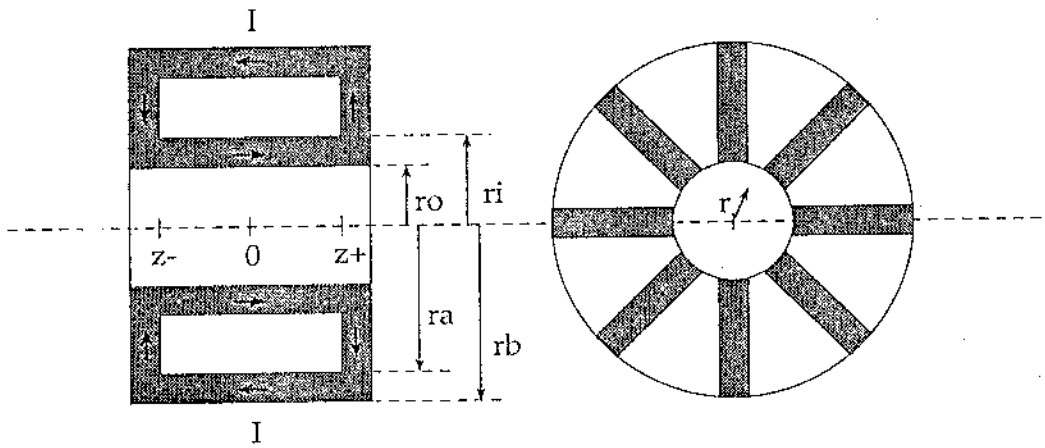

Figure 4. Ideal toroid with a rectangular section showing azimuthal gaps between sectors with windings.

2.1.2. Ideal-Toroid Field Approximation

Next we consider the analytically simple example of an ideal toroid with a rectangular cross section carrying a current I as indicated in Figure 4. The azimuthal component of the magnetic field for an uniform current distribution is given by

$$B_\phi(r,z) = \frac{\mu_o}{2\pi} \cdot \frac{I(r,z)}{r} \qquad \left(\frac{\mu_o}{2\pi} = 0.2 \text{ gauss-cm/A}\right) \qquad (3)$$

where I(r,z) is the total current linked by the field circuit. Even with the introduction of periodic gaps between the coil windings as shown in the figure, the expression can serve as an useful approximation.

From equation (3) it is clear that for a given current density, the largest field will be produced by placing the current distribution as close to the axis (r = 0) as possible. However, for a real toroidal spectrometer, the amount of current that can be situated near the axis is restricted by two geometric considerations. The first is the space that is needed about the axis for the electron beam, the target, and the coil support, and the second is the importance of providing maximal azimuthal acceptance through the open gaps between the coils.

The most compact configuration of near-axis currents will have conductors in radial wedges ($r_i > r > r_o$) occupying a fraction, f, of the full azimuthal range.

Note that the fields depend on f, and not on the number of discrete coils involved. For a current density σ, and for $z_- < z < z_+$, the field in an unoccupied gap between coils is

$$B_\phi(r) \approx 0 \qquad (r_o > r > 0) \qquad (4)$$

$$B_\phi(r) \approx \frac{\mu_o}{2\pi} \cdot \pi \cdot \sigma \cdot f \cdot \frac{(r^2 - r_o^2)}{r} \qquad (r_i > r > r_o) \qquad (5).$$

Within the torus:

$$B_\phi(r) \approx \frac{\mu_o}{2\pi} \cdot \pi \cdot \sigma \cdot f \cdot \frac{(r_i^2 - r_o^2)}{r} \qquad (r_a > r > r_i) \qquad (6).$$

The field rises almost linearly to a maximum value at the radius of the inside edge of the conductor at $r = r_i$, and then begins to fall like $1/r$ through the region of the central aperture. Beyond the aperture in the idealized case, the field falls, again almost linearly, to zero.

Although the magnetic fields of the toroid are far from uniform in the radial direction, they are translationally invariant with respect to the symmetry axis for $z_- < z < z_+$; and by analogy with the dipole case discussed above, one might expect to find similar $(x \mid x) = 0$ focal properties. That this is in fact the case can be seen from Figure 5 which again shows plots of extended target proton trajectories corresponding to $Q^2 = 0.1$, 0.3, and 0.5 GeV^2/c^2. The radial disposition of the conductors with respect to the symmetry axis is indicated. In this simple model, the cross-sectional area of the conductor is held constant and is assumed to occupy the full angular bite in alternating azimuthal sectors. This constraint results in different radial widths for the inner and outer runs of the coil. We can use the ideal toroid to understand some of the conditions that lead to the most efficient use of currents and associated fields. For illustration, we will consider a fixed current density, $\sigma = 1.0$ kA/cm^2, and set $f = 0.5$. The most compact set of proton trajectories is obtained when r_i is made so large that all of the rays fall within the $B \sim r$ region. This configuration is shown in Figure 6. The total amount of conductor can be reduced substantially by allowing the trajectories to move into the $B \sim 1/r$ region as is illustrated in Figure 5. The

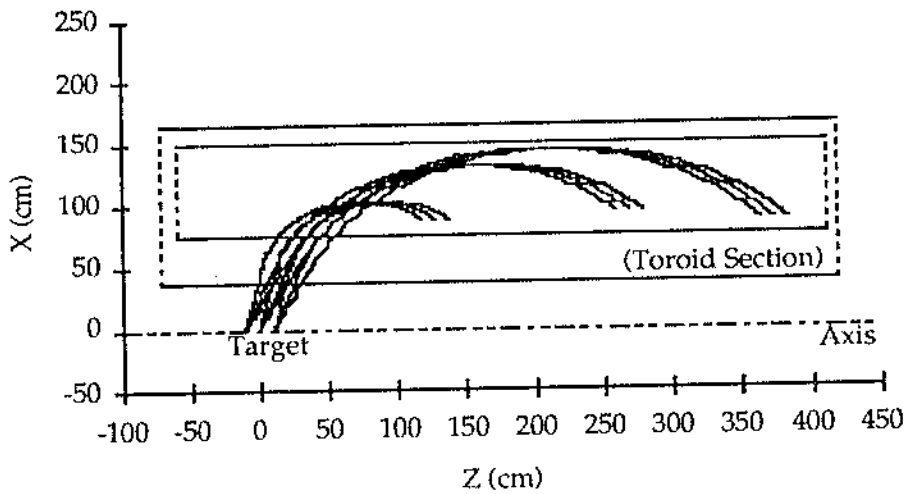

Figure 5. Ideal toroid: $(x \mid x) = 0$ optics for proton trajectories corresponding to $Q^2 = 0.1$, 0.3, and 0.5 GeV^2 from a 20-cm target. Conductors fill radial wedges in the areas indicated by the solid lines ($f = 0.5$). The symmetry axis is indicated by the dot-dash line. The focus is in the $B \sim 1/r$ region.

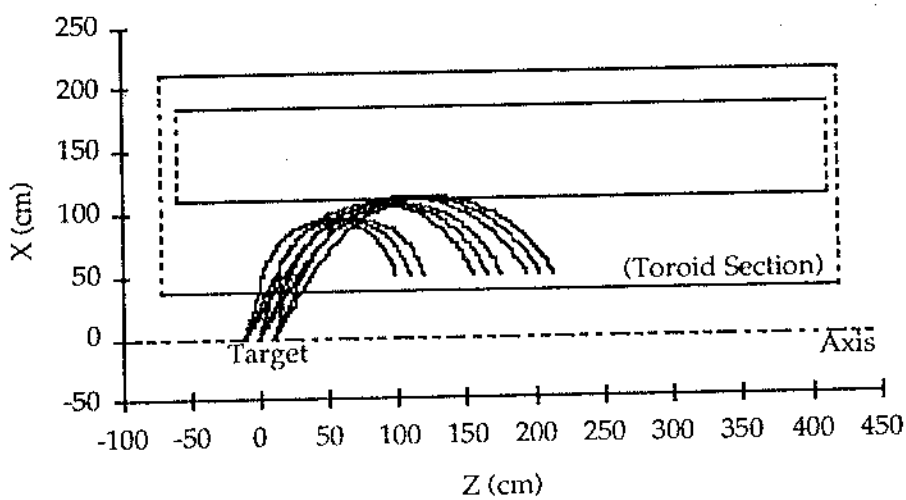

Figure 6. Ideal toroid: the focus is in the $B \sim r$ region.

$(x \mid x) = 0$ foci move progressively outward as the amount of conductor is decreased. With a further reduction however, Figure 7 shows that the focus fails for larger Q^2. Figure 8 indicates that this focus can be restored if the aperture of the toroid is also increased. Partial compensation for additional reductions in the conductor cross-section can be made by progressive

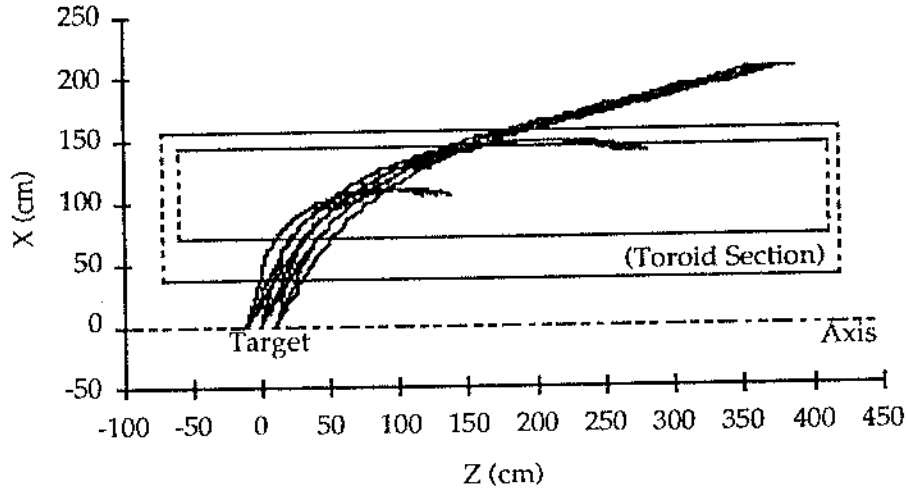

Figure 7. Ideal Toroid: reduced conductor cross section. For large values of Q^2 the focus is lost.

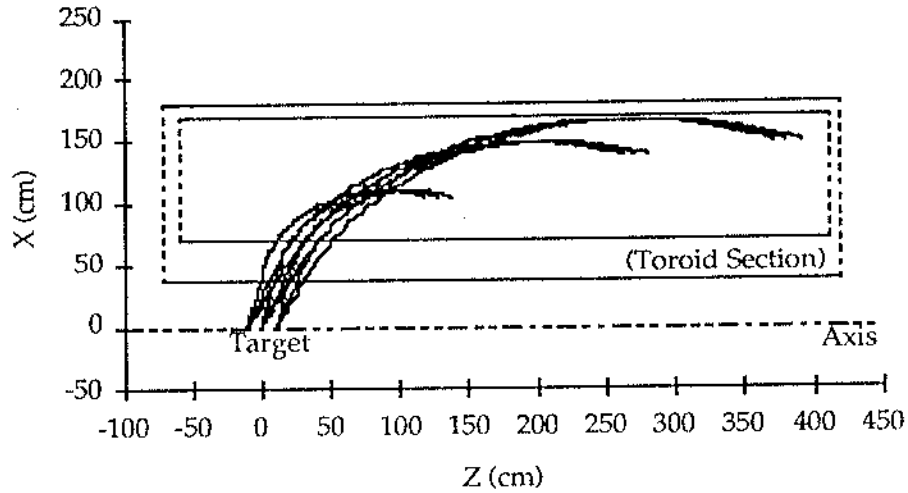

Figure 8. Ideal toroid: The focus at large Q^2 is retained if the size of the coil is increased as the amount of conductor is reduced.

enlargements of the aperture and thus the overall size of the coil. With these changes, the focal plane continues to move outward, and the dispersion is increased. It is clear that there are both performance and cost trade-offs between the amount of conductor (Amp-turns) and the overall size of the coil. We will return to these issues when the coil is modeled in greater detail in section 2.2.

2.1.3. Modified-Gaussian Field Approximation

In order to be able to examine entrance- and exit-edge effects, we need to consider a more realistic magnetic field distribution than that of the simple ideal toroid. In particular, a reasonable representation of the median-plane fields of a toroid with extended windings is given by a gaussian function, peaked at (a, b), that is modified to vanish at the z (symmetry) axis:

$$B_\phi(z,x) = D(x) \cdot B_{max} \cdot e^{-\left(\frac{(z-a)^2}{\sigma_z^2} + \frac{(x-b)^2}{\sigma_x^2}\right)} \qquad (7)$$

$$D(0) = 0$$
$$D(b) = 1$$

$$a = z_- \qquad (z < z_-)$$
$$a = z \qquad (z_- < z < z_+)$$
$$a = z_+ \qquad (z > z_+)$$

$$b \sim r_i$$

The moments σ_z and σ_x reflect the extent of the windings, and the moment σ_x reflects, in addition, the radial size of the toroid (e.g.. the location of r_a relative to r_i in Figure 4). There is considerable latitude in the choice of the form of the modification function D(x), and for convenience we have chosen a form that gives simple analytic expressions for the constant-field contour lines.

$$D(x) = e^{\left(1-\left(\frac{b}{x}\right)^{2/3}\right)\cdot\frac{(x-b)^2}{\sigma_x^2}} \qquad (8).$$

Plots of the distribution for a peak field of 1.0 Tesla are given in Figure 9 for (a, b) = (110, 90) and $\sigma_z = \sigma_x = 57$. From equation (5) we would expect B_{max} to scale as $(b\text{-}r_o^2/b)$.

The simple analytic expression for the median-plane fields given by equation (7) can be used to trace trajectories and examine in a general way the dependence of the optics on the dimensions of the toroid.

We begin by observing that the size or extent of the field region will be governed by the minimum deflection angle, θ_{bend}, that can both provide the required

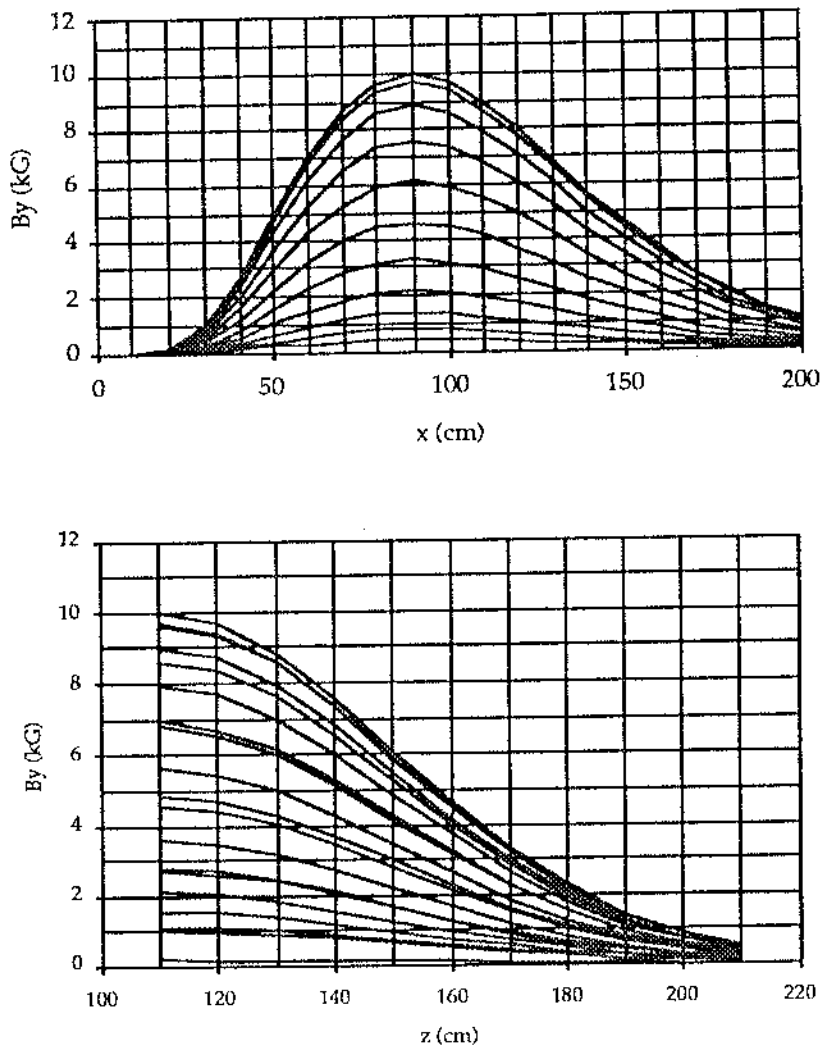

Figure 9. Modified-gaussian median plane fields, B_{max} = 1.0 Tesla. In this case, (a,b) = (110,90), and $\sigma_z = \sigma_x = 57$.

dispersion and permit reasonable line-of-sight shielding for the particles with the highest momentum

$$\int B \cdot dL(kG - cm) = (3.34) \cdot p(MeV / c) \cdot \theta_{bend} \qquad (9).$$

As an example, for $\theta_{bend} = 35°$, protons corresponding to $Q^2 = 0.5$ need to traverse an integral field of 1.6 Tesla-m.

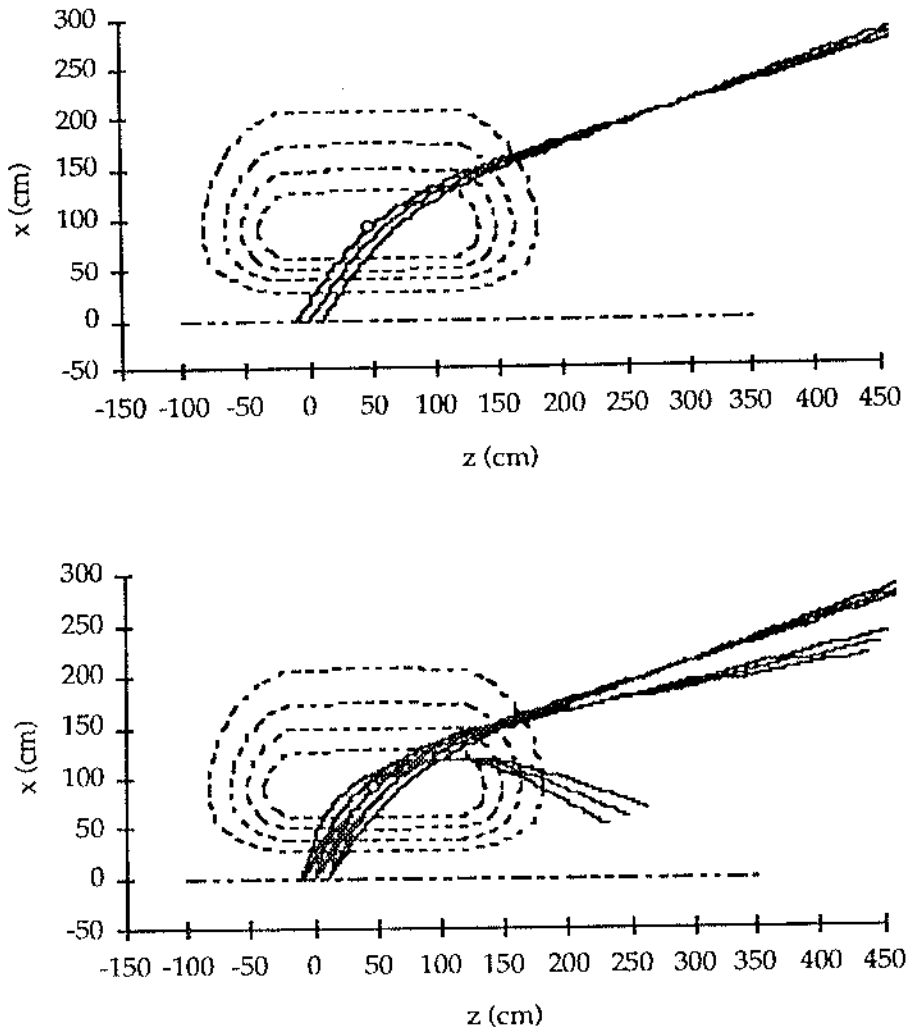

Figure 10. Modified-gaussian: $r_i \sim 90$ cm, and $B_{max} \sim 11.5$ kG. Above, $Q^2 = 0.5$, $\theta_{bend} = 40°$. Below, $Q^2 = 0.1, 0.3, 0.5$. The dashed lines indicate the contours corresponding to 20 %, 40 %, 60 %, and 80 % of maximum magnetic-field.

It is clear that for the most efficient use of the field distribution of the toroid, the trajectories of particles with the highest momentum needing the largest deflection should pass through the peak magnetic field. Specifically, protons corresponding to the largest Q^2 of interest and coming from the up-stream end of the target should pass near the point (a, b). This is illustrated in Figure 10(a) ($Q^2 = 0.5$: $\theta_{bend} \sim 40°$) for a conductor cross section specified by $r_i \sim 90$ cm and a current density specified by $B_{max} \sim 11.5$ kG. The dashed lines indicate contours that correspond to 20 %, 40 %, 60 %, and 80 % of the maximum magnetic-field,

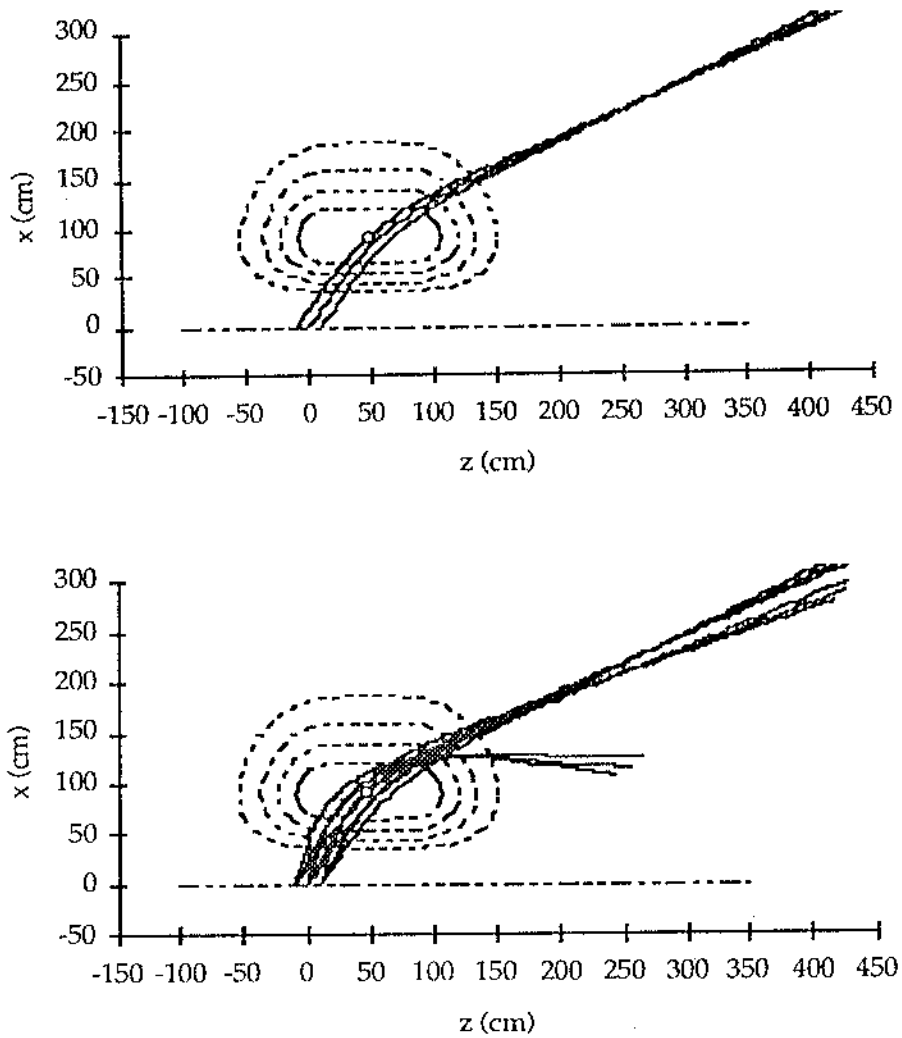

Figure 11. Modified-gaussian: $r_i \sim 90$ cm, and $B_{max} \sim 11.5$ kG. Above, $Q^2 = 0.5$, $\theta_{bend} = 30°$. Below, $Q^2 = 0.1, 0.3, 0.5$.

and the point (a, b) is indicated by the small open circle. The extent of the field distribution can be reduced until the targeted bend-angle and dispersion are achieved as is shown in Figure 11 ($Q^2 = 0.5$: $\theta_{bend} \sim 30°$). Notice, from a comparison of Figures 10(b) and 11(b), that in reducing the limiting bend-angle from 40° to 30° the Q^2 dispersion at the high end of the focal surface is also reduced by perhaps a factor of two. What is gained is a reduction of about 25 % in both the longitudinal and radial dimensions of the field distribution. We note that for a fixed value of $\theta_{bend}(Q^2_{max})$, certain trade-offs are possible between the radial (x) and longitudinal (z) dimensions of the field distribution. To some degree, increases in radius can compensate for reductions in length and vice

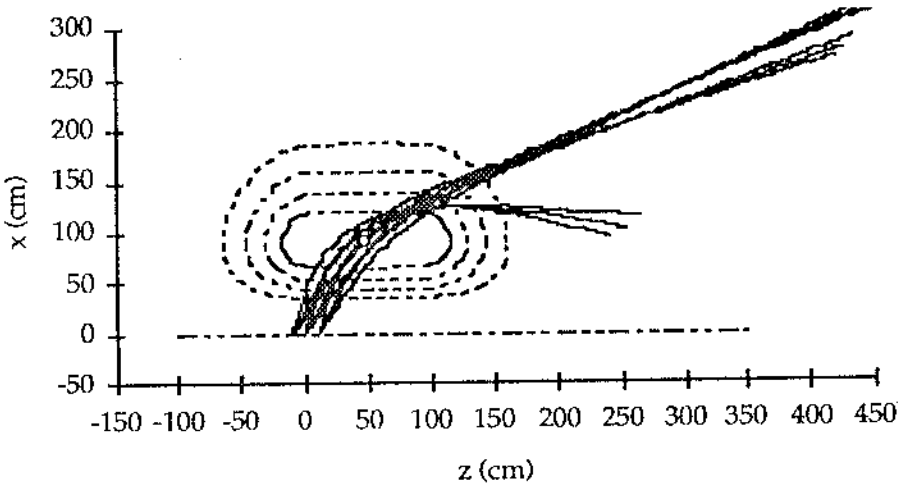

Figure 12. Modified-gaussian: $r_i \sim 90$ cm, and $B_{max} \sim 11.5$ kG. Less effective entrance-edge rotation than in Figure 11(b).

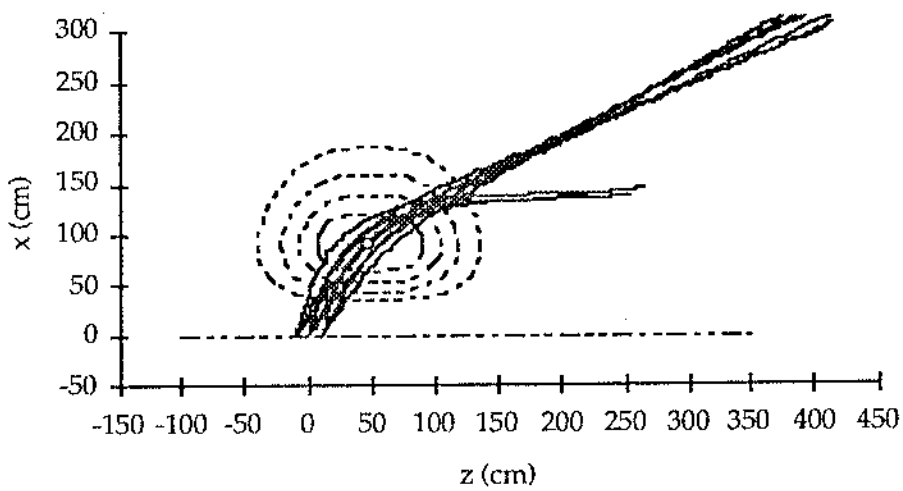

Figure 13. Modified-gaussian: $r_i \sim 90$ cm, and $B_{max} \sim 11.5$ kG. Too much effective entrance-edge rotation; the low Q^2 focus is lost.

versa. This is important for the detailed tailoring of the optics because as the length of the field distribution is reduced below a certain point, the translational invariance of the field seen by rays from the target is broken in a manner that corresponds to an effective entrance edge rotation. As in the previously discussed case of the dipole (Figure 2), this effective rotation can be used to move the focal plane outward. A comparison of Figure 12 with Figure 11(b) shows the low-Q^2 focus falling much closer to high-Q^2 trajectories in the case of

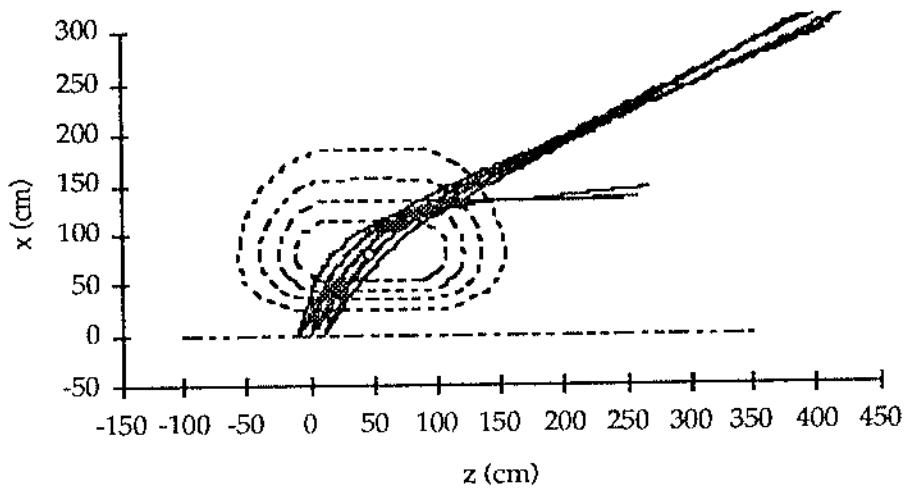

Figure 14. Modified-gaussian: $r_i \sim 80$ cm, and $B_{max} \sim 10.0$ kG. The field must fill a larger volume than the example of Figure 11(b) to achieve comparable performance.

the former (less effective edge-rotation) than in the case of the latter. With additional reductions in length however, the focus starts to deteriorate beginning with low Q^2, and both the resolution and the kinematic acceptance rapidly erode. This point is illustrated by a comparison of Figure 11(b) with Figure 13. The latter has more effective edge-rotation.

The practical usefulness of a physical rotation of the inner edge of the conductor that makes up the coil depends on the size of the field gradient that can be achieved with a particular spectrometer geometry. This is one area in which there are significant differences between the normal- and super-conducting options. The issue will be discussed in section 2.2.

It is also of interest to consider again the effect of a reduction in the conductor cross-section for fixed current density. For $r_i \sim 80$ cm ($B_{max} \sim 10$ kG from equation (5)), comparable performance to the $r_i \sim 90$ cm case can be achieved if the dimensions of the field distribution are also increased as shown in Figure 14. The magnetic-field effective length needs to be increased by about 10 % and the radius by about 5 % to permit this reduction in conductor area of order 25 % ($f \sim 0.5$). The implications of this kind of conductor-size vs. spectrometer-size trade-off for fabrication and power costs will be examined in detail in section 2.2.

2.2. Realistic Fields

In the previous Section 2.1, we explored ways in which the gross dimensions and lowest order moments of the magnetic-field distribution, $B_\phi(r)$, are determined by the required Q^2 dispersion and acceptance, and by the deflections needed for line-of-sight shielding. In order to proceed with the design and optimization of a realistic spectrometer it is necessary to compute the fields that arise from reasonable dispositions of actual conductors. We have chosen to model the spectrometer with current filaments arrayed to approximate the real geometry of the coils. The position of a current filament in 3-space is easily specified, and its contribution to the magnetic field anywhere can be determined by a simple Biot-Savart computation. Details of the techniques employed in the field and trajectory calculations will be discussed in Section 3.2. The way in which the cost of the spectrometer scales with the actual number of discrete coils is less than linear because, in lowest order, the total number of windings is independent of their azimuthal disposition. However, the need for axial symmetry dictates that the number of coils be even. Also, if there are too few coils, the fields will have a strong azimuthally-dependent radial component. This component will tend to defocus entrant rays in the non-dispersion direction (i.e. $(y \mid z) > 0$, $(y \mid \phi) > 1$) and, reduce both the azimuthal acceptance of the spectrometer and the extended-target performance at large values of ϕ. We have chosen an eight-coil configuration as a reasonable compromise in this regard. It also should be noted that consideration was given to the fact that one can imagine using a toroid as an out-of-plane spectrometer [La91b]. Because the out-of-plane response functions enter the coincidence cross-section with sine and cosine dependences on ϕ and 2ϕ, it is desirable, for optimal separation, to be able to make measurements at eight symmetric angles: $\phi = n\pi/4$ ($n = 0$ to 7).

The actual design of an optimized winding distribution is a computation intensive process that can be guided by the observations made in the present section and in Sections 2.1.1, 2.1.2, and 2.1.3 above.

2.2.1. Normal- vs. Super-Conducting Options

Because the current densities that are achieved with super conductors (SC) can be at least an order of magnitude greater than those attained with normal conductors (NC), we might expect there to be significant differences between

spectrometer designs that are optimized in the two different contexts. But it is also clear from the discussion of optimization criteria above, that in lowest order, the overall physical size of the spectrometer (the extent of the magnetic fields) and even the total current (integral BdL) will be roughly comparable in the two cases if they are to have similar performance characteristics.

There are two important considerations that will cause the respective designs to diverge. The first of these is that the conductor cross-section of an NC coil will be much larger than that of a corresponding SC. Consequently, it will be more difficult to place large currents near the symmetry axis in the former case without also significantly reducing the azimuthal acceptance. In addition, the physical restrictions on the distribution of currents will limit the maximum field gradients that can be achieved. The optical 'edges' of the NC spectrometer will tend to be relatively diffuse. The second consideration relates to the cryogenic accommodation of SC coils. The provision of an individual cryostat for each coil is an expensive proposition. A large common cryostat is much more cost effective, but it also will have a greater impact on the optics of the spectrometer. In particular, if the detector array is to be kept outside of the common cryogenic tank, the focal surface will need to be located somewhat farther from the coils than it otherwise would need to be. It is important to note in this regard that magnetic-field gradients can be much larger for compact SC coils than for corresponding NC coils, and as a result an optical 'edge', particularly near the symmetry axis, can be relatively well defined. This opens up the possibility of incorporating a physical entrance-edge rotation into the SC design to help shift the focal surface. This will be discussed in Section 2.2.3.

It was noted in Section 1.2 that a justification for the potentially larger initial cost of an SC spectrometer relative to an NC alternative comes from the much higher operational costs associated with the latter. In order to be able to quantify this trade off, a reference design for a normal-conducting spectrometer is discussed in Section 2.2.2. The design of the proposed super-conducting G^0-spectrometer is presented in Section 2.2.3. The expected performance of this SC spectrometer will be detailed in Section 3.

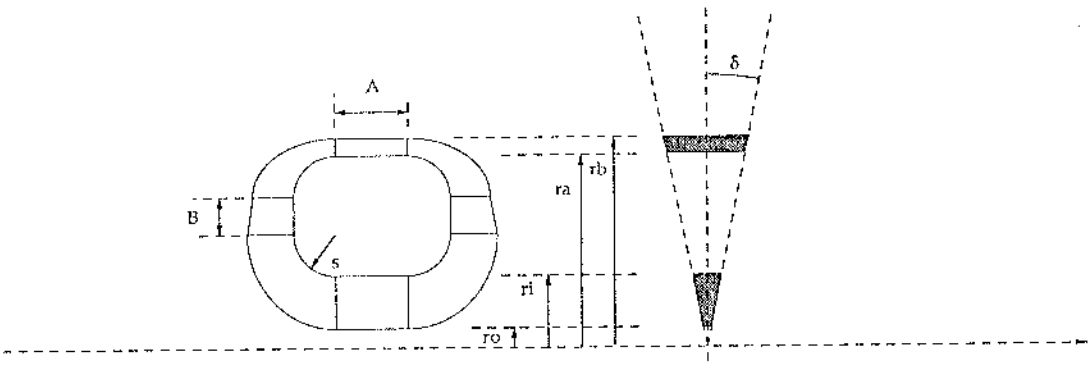

Figure 15. Compact coil geometry.

2.2.2. Normal-Conducting Spectrometer Optimization

For the normal-conducting spectrometer optimization, the currents and spacing of filaments were fixed to correspond to an effective average current density of $\sigma = 0.56\ \mathrm{kA/cm^2}$ in the coil section. This is a reasonable value for insulated Cu windings that are provided with water-cooling channels. As was noted in the discussion of the ideal toroid above, the most compact configuration of near-axis currents will have conductors in radial wedges occupying a fraction, f, of the full azimuthal range. Because we want to maximize both the amount of current at small radii and the total azimuthal acceptance, we take f = 0.5. The compact coil geometry is illustrated in Figure 15. This is a limiting case, and likely would be

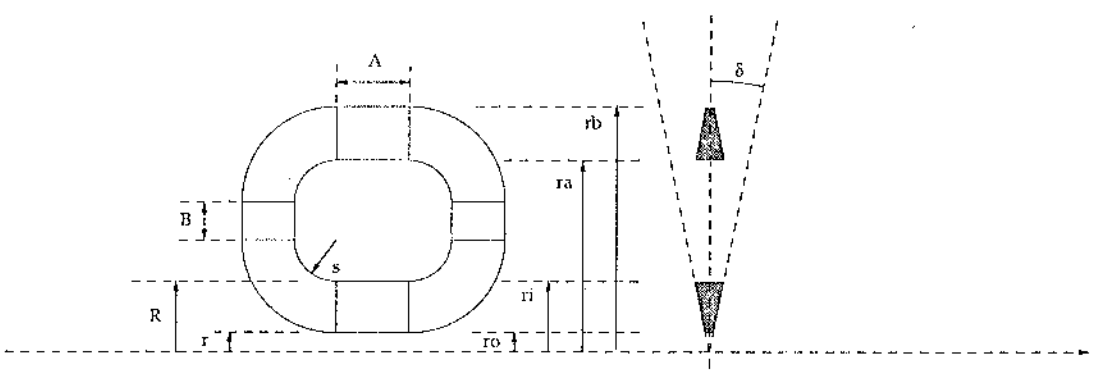

Figure 16. Planar coil geometry.

rather expensive to fabricate with real conductors because of the constantly changing shape of the coil cross-section. A mechanically simpler geometry which retains a uniform conductor cross-section and permits planar windings is shown in Figure 16. In addition to being simpler, away from the axis this planar geometry does not occupy the full azimuthal wedge allocated to the conductor, and thus provides for a relatively larger ϕ-acceptance (i.e. $(y \mid y), (y \mid \phi) > 1$). We note that a planar coil requires about 10 % more conductor volume than a roughly equivalent compact coil. Because the fabrication cost of a normal-conducting coil of fixed design scales with the volume of the conductor, V, we would expect that the materials for the planar coil would be about 10 % more expensive than those for a compact coil, but that the greater fabrication costs for the latter would more than compensate for this difference. The power required also scales with the volume of conductor:

$$P \sim \sigma^2 \rho V \tag{10}$$

where σ is the current density and ρ is the resistivity of Cu.

The geometry of the optimized coil is shown in Figure 17. The total current is 0.8 MA-turns in each of the eight coils. Median-plane proton trajectories, corresponding to $Q^2 = 0.1$, 0.3, and 0.5 MeV^2/c^2, are shown coming from a 20-cm target. Note that the focus for low Q^2 falls within the boundary of the coils. Figure 18 shows a contour plot of the median-plane magnetic fields, B_ϕ, overlaid by the trajectories of Figure 17. Note the similarity of these contours to the approximate modified-gaussian contours of Section 2.1.3. It can be seen that the $Q^2 = 0.5$ ray from the up-stream end of the target passes through the peak field region. This is the efficient field-use condition of Section 2.1.3. The bend angle for this extreme ray is 30°. This spectrometer design was presented and discussed in some detail in the G^0 proposal to CEBAF [PR92], and before the CEBAF PAC5 [CEBAF Nov. 18-22, 1991], the CEBAF Strange Currents/Parity Review Committee [CEBAF July 6-8, 1992], and the CEBAF Internal Technical Review Committee [CEBAF Oct. 25-26, 1992; [La92]]. Some of the more important optical and physical characteristics of the spectrometer are summarized in Table 5. In particular, we note the power consumption figure of 4.6 MW. Using a CEBAF estimate of $ 85/MW-hr, this would corresponds to an expenditure of about

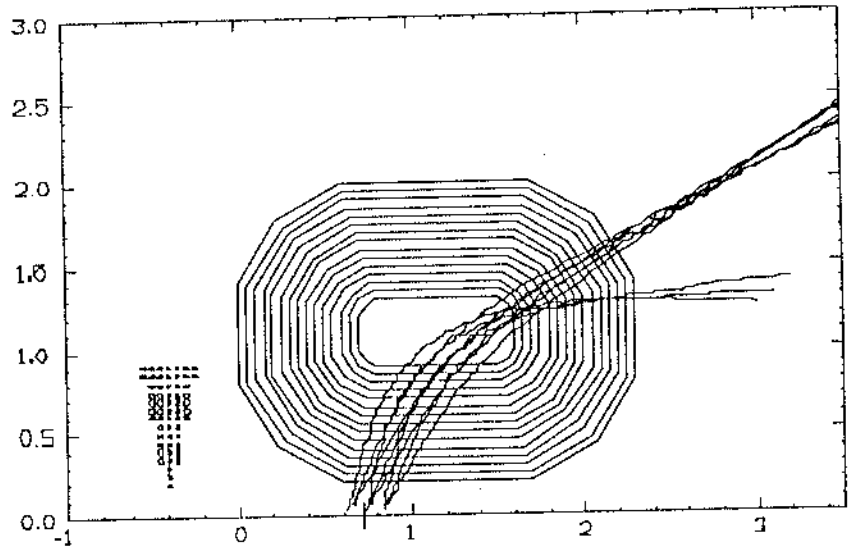

Figure 17. Normal-conducting reference coil: $(x \mid x) = 0$ optics for proton trajectories corresponding to $Q^2 = 0.1$, 0.3, and 0.5 GeV^2 from a 20-cm target. Filamentary circuits were distributed to approximate an effective uniform current density of 0.56 kA/cm^2 in each of eight azimuthally symmetric coils. Note the triangular profile of the windings. Dimensions are in meters.

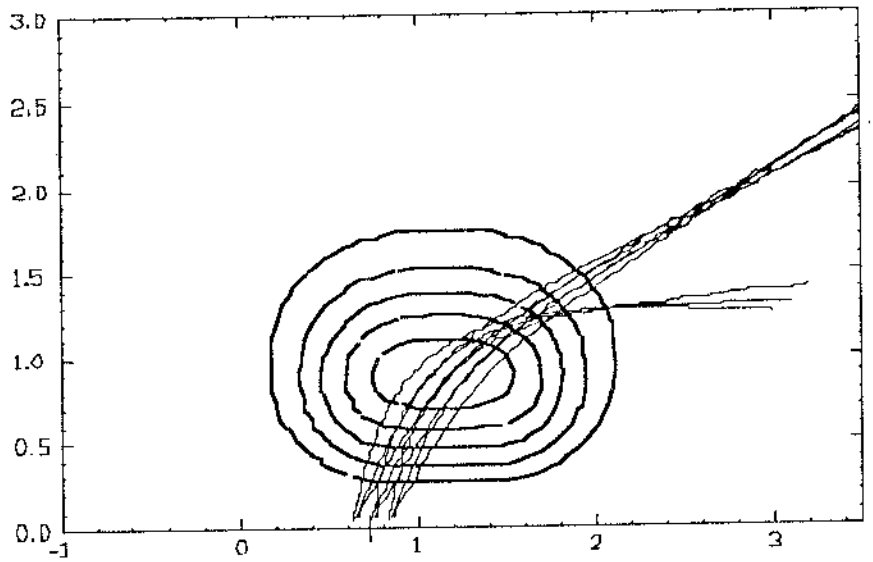

Figure 18. Normal-coil median-plane magnetic field contours at 2-kgauss intervals. The trajectories of Figure 17 pass through the peak field region. Dimensions are in meters.

Table 5. Reference Normal-Conducting Spectrometer

• Configuration:	Normal-conducting Toroid (Iron free)
• Optics:	$(x \mid t) = 0$
• Central Momentum:	550 MeV/c @ $\theta = 68°$
• P_{max}:	800 MeV/c @ $\theta = 60°$
• Resolution:	$\Delta p/p < 5$ % $\Delta\theta < 3°$ $\Delta Q^2/Q^2 < 10$ %
• Φ acceptance:	~ 45 % of 2π
• Magnetic fields:	$\int B \cdot dL$ ~ 1.3 Tesla-meter
• Number of coils:	8
• Turns/coil:	228
• NI_{tot}	6.4 MA-turns
• Line power (max):	4.6 MW
• Cooling water (max):	750 gpm
• Coil weight:	32 tons
• Spectrometer weight:	62 tons

$400 per hour of running time. The cost of the eight normal-conducting coils in the spectrometer is estimated to be about $ 1.11 M. This number is based on an average cost of about $ 38/kg-Cu (fabricated) reported in recent bids for similarly constituted coils intended to be incorporated in the BLAST spectrometer [BL91].

Because both fabrication costs and power requirements scale with the volume of the coils, the success of the cost-optimization of this spectrometer can be assessed in terms of volume changes associated with modifications of the reference configuration. We are interested in the partial derivatives of V with respect to R, A, B, r, and δ as defined in Figure 16. The fractional change in volume is then:

Table 6. Volume Change Coefficients.

x	$\frac{1}{V}\frac{\partial V}{\partial x}$
R (cm)	0.028 (cm^{-1})
A (cm)	0.005 (cm^{-1})
B (cm)	0.005 (cm^{-1})
r (cm)	-0.0075 (cm^{-1})
δ (degrees)	0.091 ($degree^{-1}$)

$$\frac{\Delta V}{V_0} \approx \frac{1}{V}\frac{\partial V}{\partial R}(R - R_0) + \frac{1}{V}\frac{\partial V}{\partial A}(A - A_0) + \frac{1}{V}\frac{\partial V}{\partial B}(B - B_0)$$

$$+\frac{1}{V}\frac{\partial V}{\partial r}(r - r_0) + \frac{1}{V}\frac{\partial V}{\partial \delta}(\delta - \delta_0) \qquad (11).$$

The coefficients are listed in Table 6.

We first consider the question of whether the reference coil can be further reduced in size while maintaining a constant conductor cross-section. Figure 19 shows a coil that is about 3 % smaller in volume than the reference. It can be seen that this smaller coil is no longer capable of attaining a zero-magnification focus at low Q^2. Even for the higher Q^2 points shown, the focus is somewhat degraded with respect to that found in Figure 17. This suggests that the reference design is very close to the minimum size consistent with the required kinematic range and performance.

Now let us consider a reduction in the cross-section of the windings. Figure 20 shows a coil having only 75% of the number of amp-turns that are found in the reference design. In this case, the conductor volume is smaller by about 20 %. As would be expected, the bend angle of the extreme ray is reduced from 30° to 26°, and the Q^2 dispersion is only about 17 % of that of the reference. From the discussion in Section 2.2.3, we know that performance roughly comparable to that of the reference design can be achieved with this reduced conductor cross-section by making the size of the coil larger. An example of this is illustrated in Figure 21. Here the bend angle is 28° and the dispersion falls within 15 % of

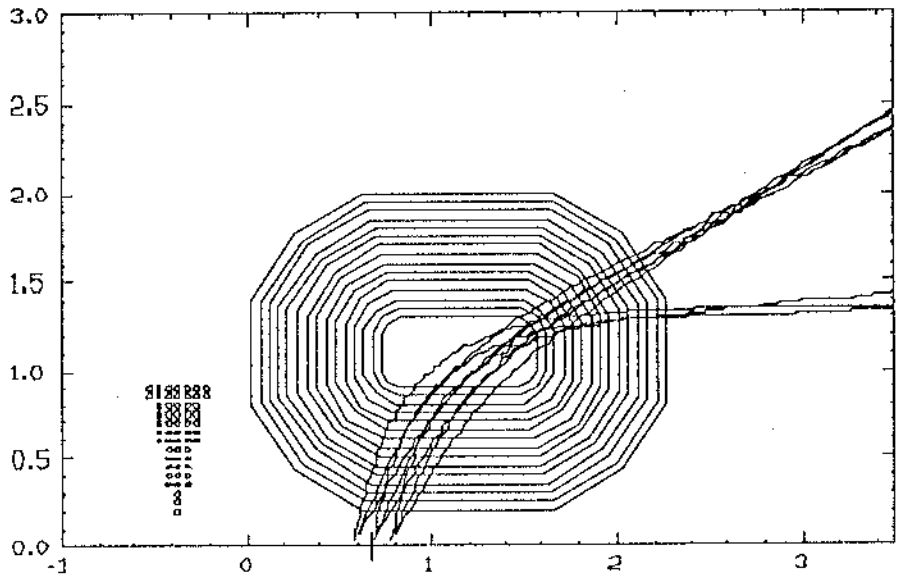

Figure 19. An NC coil 3 % smaller than the reference. Proton trajectories corresponding to $Q^2 = 0.1$, 0.3, and 0.5 GeV^2 from a 20-cm target. The low Q^2 focus is lost.

that of the reference. But the increase in coil size has also increased the conductor volume back to 95 % of the reference value, effectively eliminating any cost advantage associated with fewer windings. At the same time, the focal plane has become 50 % longer (60 % more area) which probably implies additional instrumentation and shielding costs. Note, however, that the path-length for the highest Q^2 rays has increased by 20 to 25 % which would have positive consequences for the time-of-flight measurement.

From the examples of this section, we conclude that the reference design for the normal-conducting spectrometer can be considered to be cost optimized in that it is not possible to effect significant reductions in either fabrication or operational expenses without also substantially reducing the performance of the device.

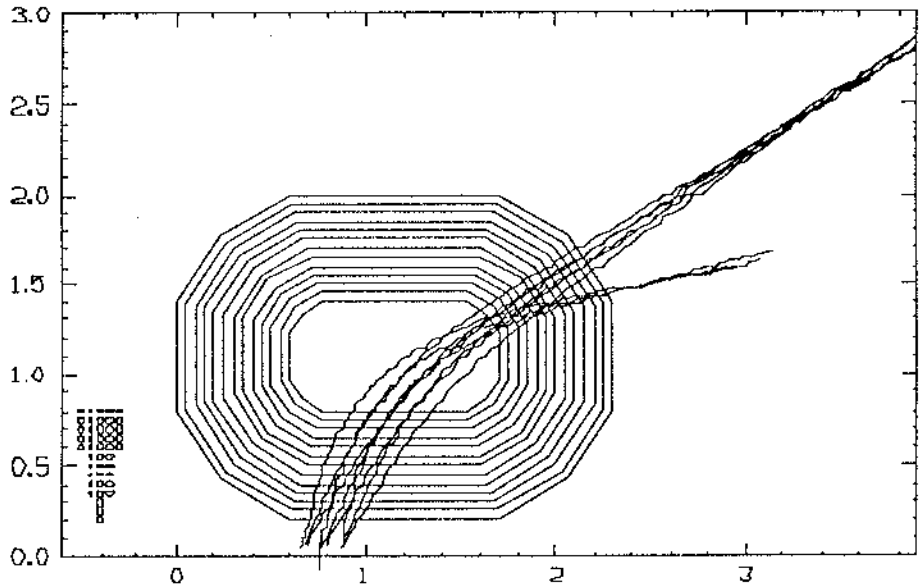

Figure 20. An NC coil with 75 % fewer windings than the reference. Proton trajectories corresponding to $Q^2 = 0.1$, 0.3, and 0.5 GeV^2 from a 20-cm target. The higher Q^2 trajectories are poorly resolved.

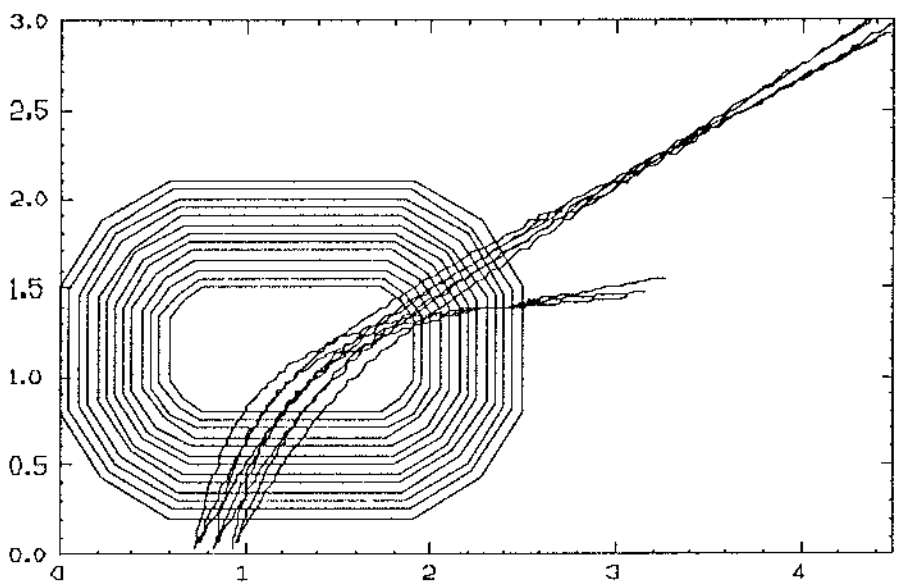

Figure 21. An NC coil with fewer windings than the reference must be made relatively larger to achieve comparable performance.

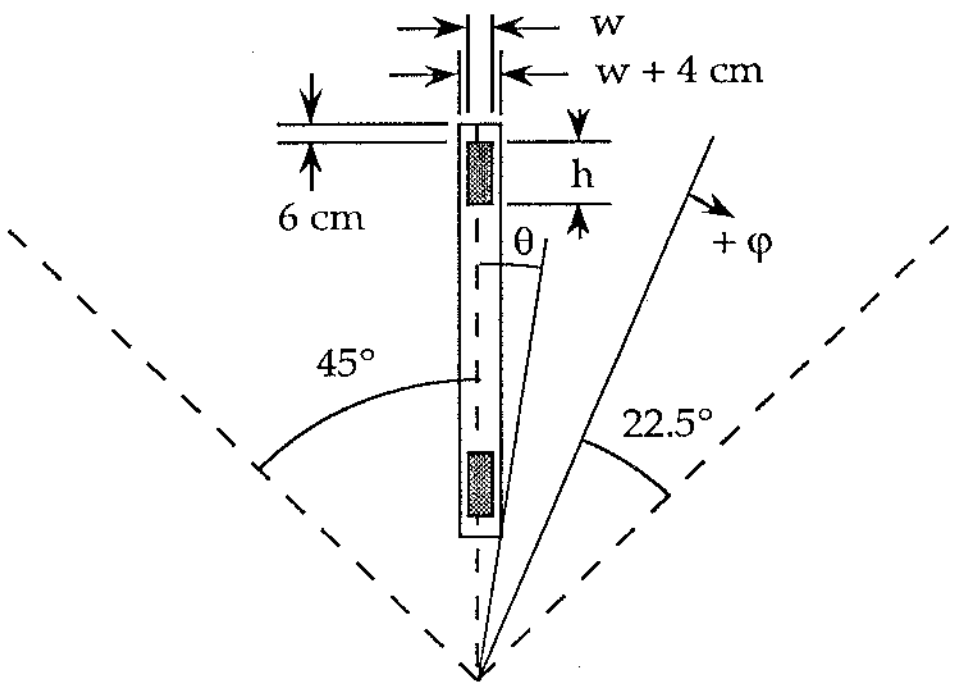

Figure 22. Schematic cross section of the SC coil showing the conductor (w x h, shaded), and the relative dimensions of the coil case.

2.2.3. Super Conducting Spectrometer Optimization

For the super-conducting spectrometer optimization, the currents and spacing of filaments were fixed to correspond to an effective average current density of $\sigma = 5.0$ kA/cm^2 in the coil section. Our intention was to base the optical design on a very conservative conductor configuration. The conductor is described in Section 3.1, and is discussed in detail in Section 9.3.1 of [TD93]. It has an over-all cross section of 0.5- x 2.0 cm. Because of the relatively high current density, it is neither practical nor necessary to require a wedge-shaped coil profile near the symmetry axis. It is assumed that the conductor will be wound in a double-pancake configuration. This winding arrangement keeps the leads on the outer perimeter of the coil, simplifies the connections and splices, and produces a uniform rectangular cross section as shown in Figure 22. Also shown in the figure are the dimensional allowances required by the coil case. The design of this case combines the functions of winding-bobbin and coil support and incorporates the cooling channel [TD93]. For reference in the following discussion, a specification of the SC coil profile is given in Figure 23. Here, the optical effects of entrance-edge rotations (δ) tend to be an

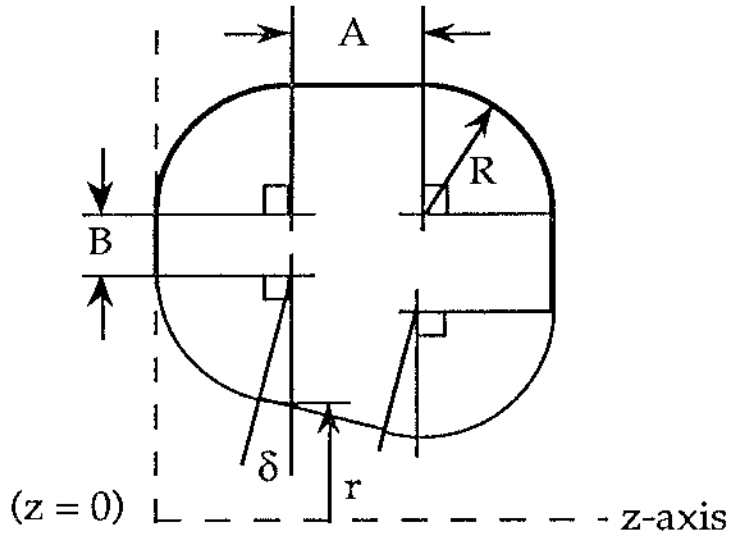

Figure 23. Generalized SC-coil perimeter profile.

order of magnitude greater than those of corresponding exit-edge rotations, and we find that there is no practical reason to attempt to make use of the latter.

From the examination of optimization criteria above (Sections 2.1, and 2.2.1), if the two toroids are to have similar performance characteristics, we know that the overall physical size of the SC spectrometer will be roughly comparable to that of the NC design of Figure 17. In the SC case however, we do not have the same kind of strong correlation between performance and the costs related to conductor volume (i.e. fabrication and power) that we found for the NC option in Section 2.2.2. The cost of the conductor does not dominate the cost of the device , and the power consumption is small. As a consequence, the optimization problem becomes one of maximizing the azimuthal acceptance, the trajectory bend angles, and the Q^2-dispersion ($0.1 < Q^2 < 0.5$) in the context of the physical constraints presented by a common cryostat. In particular, the maximum diameter that an integral cryostat-tank can have is only about 4.0 meters. This is the largest size permitted by the dimensions of the Hall-C entryway. A larger device would require a significant increase in the amount of assembly and testing time needed inside of the experimental hall. Also, it is important that the optical focal-surface be constrained to lie outside of the cryostat in order to simplify the particle-detection instrumentation as much as possible.

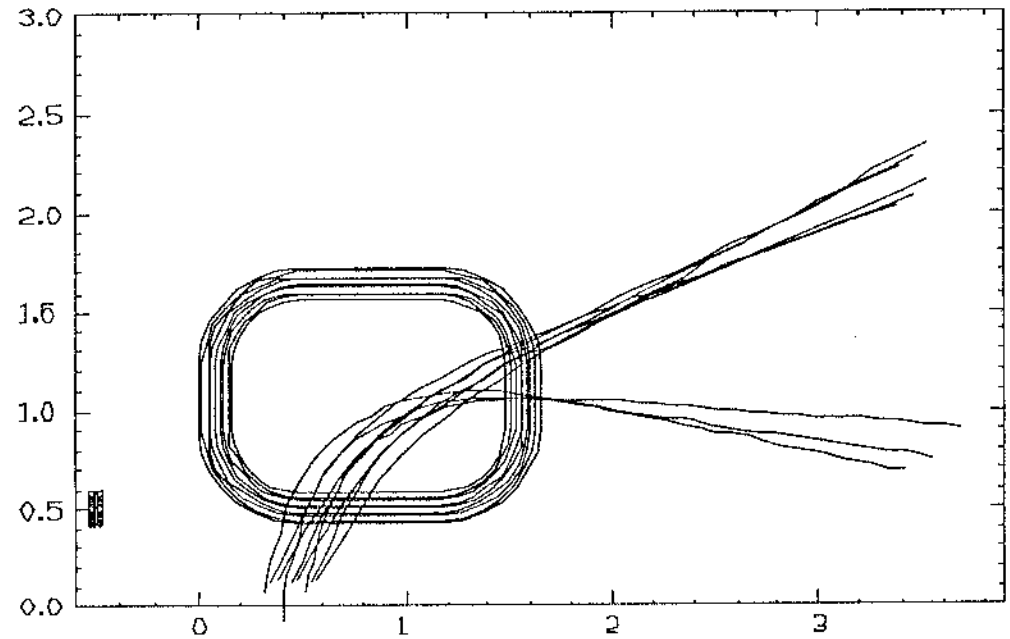

Figure 24. Symmetric SC coil. Trajectories corresponding to $Q^2 = 0.1$, 0.3, and 0.5 GeV^2/c^2 are shown for a 20-cm target. I = 0.7 MA, dimensions are in meters.

As before, the process of optimization is computation intensive. Referring to Figures 22 and 23, in order to maximize the azimuthal acceptance, we want to make r as large as possible consistent with a maximum radius for the outer return of the conductor of about 1.7 meters. In addition, the number of windings and the length of the coil need to be kept as small as possible consistent with achieving the BdL required for line-of-sight shielding, the $(R|z) = 0$ optical condition, the Q^2-resolution requirement, and the $0.1 < Q^2 < 0.5$ GeV^2/c^2 dynamic range; all over the full ϕ–acceptance.

The best solution that was obtained for a symmetric coil profile ($\delta = 0°$ in Figure 23) is shown in Figure 24. The target is 20-cm long, and trajectories corresponding to $Q^2 = 0.1$, 0.3, and 0.5 GeV^2/c^2 are shown. The Q^2 bite and dispersion are within acceptable limits, but the focus at low-Q^2 still falls very close to the coil edge. The usual means of moving the focal surface farther away by reducing the current and increasing the coil size (Sections 2.1.2 and 2.1.3) is precluded by the 4-meter limit on the overall cryostat diameter.

Another method of moving the focal surface, the effective edge-rotation associated with the change in field profile at the ends of the coil (see Section 2.1.3), has been exploited as much as possible consistent with the focal

requirement. In this connection, it is of interest to consider the effect that the coil radius of curvature, R, has on the outward movement of the focal surface. Symmetric coils optimized with R = 40 and R = 55 cm are shown in Figures 25 and 26 respectively. Although minor differences in the optics can be seen between the two cases, there is no significant difference in the position of the low-Q^2 focus relative to the coil edge.

We know from the example in Section 2.1.1 that a physical entrance edge rotation also can be useful in moving the location of the focal surface in cases where an 'edge' is sufficiently well defined. We also expect, from the general discussion in Section 2.1.2, that the field gradient associated with the width of the inner run of the SC coil shown in Figure 24 will be quite large over a distance of order 20 cm. Because this distance is relatively small on the scale of the field volume, it is likely that a reorientation of the inner run of the windings of the coil relative to the central axis will provide an additional degree of freedom that can affect both the location of the focal surface and the Q^2 dispersion. This reorientation is specified by the angle δ shown in Figure 23.

The geometry of the resulting optimized coil is shown in Figure 27. The physical entrance-edge rotation is $\delta = -5°$. The conductor cross section is 8 x 18 cm, and the total current in each of the eight coils is 0.72 MA-turns. In the figure, median-plane proton trajectories, corresponding to $Q^2 = 0.1, 0.2, 0.3, 0.4$, and $0.5\ \mathrm{MeV}^2/c^2$, are shown coming from a 20-cm target. The Q^2 dispersion is considerably greater than that seen in the symmetric coil of Figure 24. Also note that the focus for low Q^2 falls farther from of the boundary of the coils. A contour plot of the median-plane magnetic fields, B_ϕ, is shown in Figure 28. The peak field is about 1.7 T. The field drops to zero on the symmetry (z) axis, and also falls rapidly with increasing radius. Notice that the proton trajectories enter and exit the maximum-field region largely normal to the contour lines. A comparison of Figure 28 with the field-profile of Figure 18 shows that, as would be expected, the field gradient across the entrance edge is much greater for the SC coil than for the NC. In the plane of a coil, the maximum value of the magnetic field is of order 3 Tesla.

With regard to concerns about the specific cost-optimization of this coil, we note that a 10% change in the amount of coil (number of turns or profile) would correspond to only about a 1% change in the overall cost of the device. This is

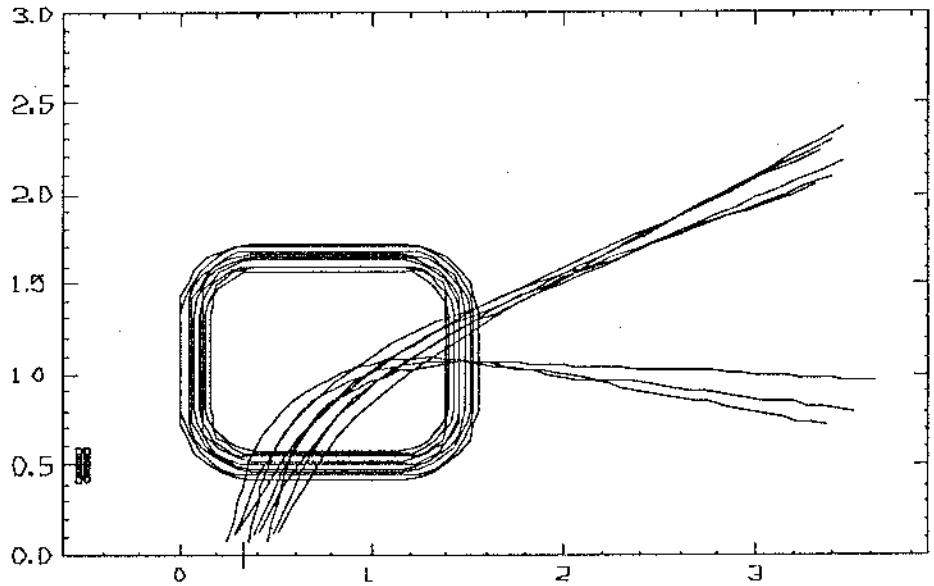

Figure 25. Symmetric SC coil with R = 40 cm. Trajectories corresponding to Q^2 = 0.1, 0.3, and 0.5 GeV^2/c^2 are shown for a 20-cm target. I = 0.7 MA, dimensions are in meters

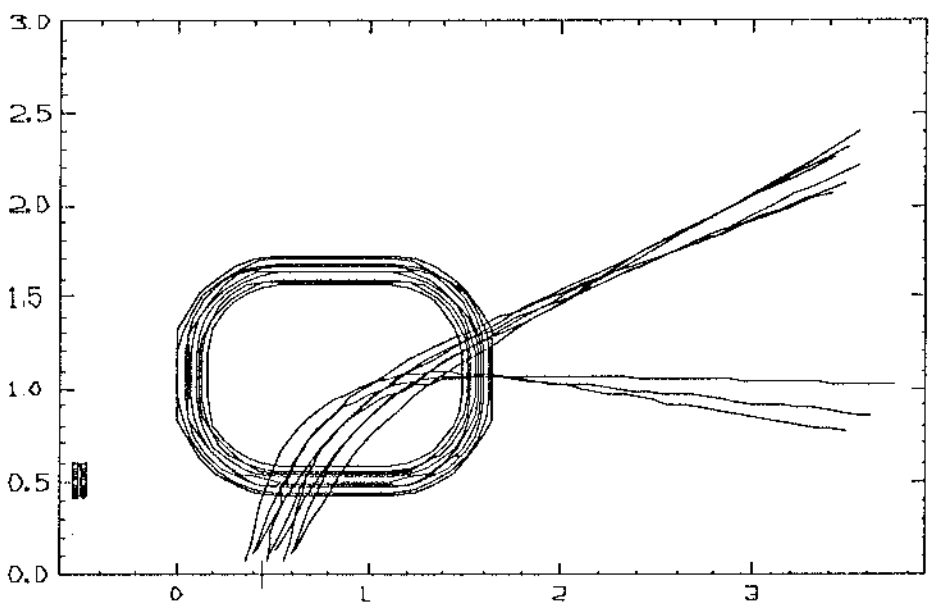

Figure 26. Symmetric SC coil with R = 55 cm. Trajectories corresponding to Q^2 = 0.1, 0.3, and 0.5 GeV^2/c^2 are shown for a 20-cm target. I = 0.7 MA, dimensions are in meters

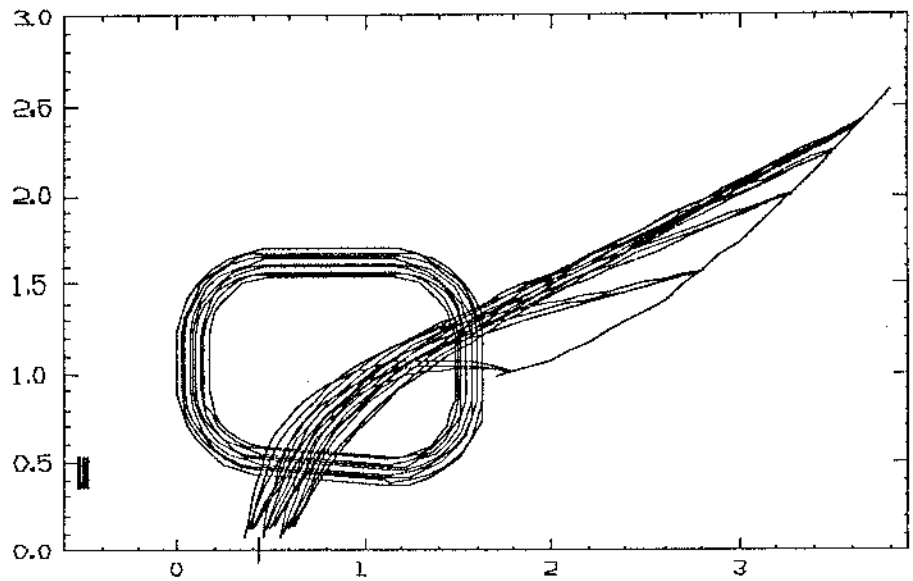

Figure 27. Optimized super-conducting coil: $(x \mid x) = 0$ optics for proton trajectories corresponding to $Q^2 = 0.1, 0.2, 0.3, 0.4$, and $0.5\ GeV^2$ from a 20-cm target. Filamentary circuits were distributed to approximate an effective uniform current density of $5.0\ kA/cm^2$ in each of eight azimuthally symmetric coils. Note the rectangular cross section of the windings. Dimensions in meters.

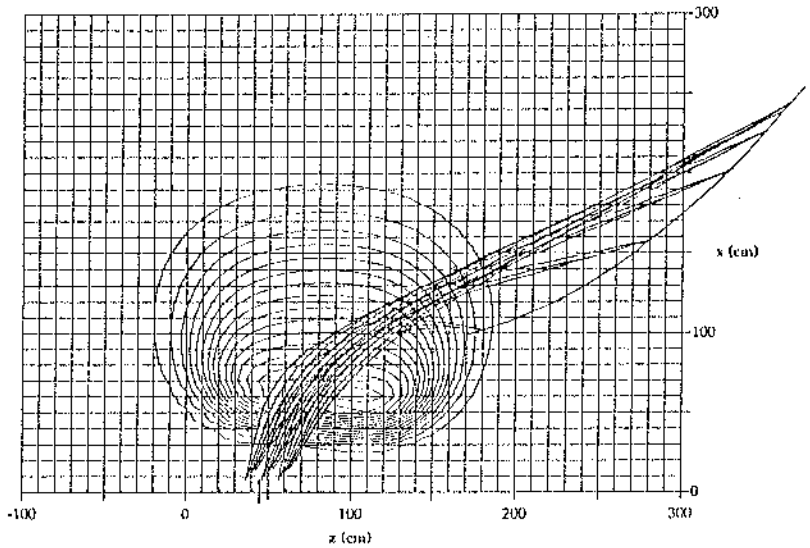

Figure 28. Super-conducting coil median-plane magnetic field contours at intervals of 1 kgauss. The trajectories of Figure 27 are superimposed.

Table 7. Optimized SC G^0-spectrometer current distribution referred to the geometry of Figures 22 and 23.

h	18 cm
w	8 cm
r	42 cm
R	50 cm
A	65 cm
B	28 cm
δ	-5°
z (target)	44 cm
I_{coil}	0.72 MA

the case because the costs associated with the cryostat, the coil cases, the support system, and the detectors are essentially constant with changes in the size or shape of the coil at the 10% level.

A specification of the current distribution for the optimized SC toroidal spectrometer is given in Table 7. The important optical characteristics and performance of the G^0 spectrometer are considered in detail in Section 3.

3. Expected Performance

3.1. Description of the Proposed Spectrometer

The G^0 spectrometer is an iron-free toroid consisting of eight super conducting coils symmetrically disposed about a central beam axis, all housed in a common liquid-nitrogen heat shield and cryostat. The cryostat is cylindrical, 4 m in diameter, and 2.0 m in length. Scattered particles bent in the magnetic fields of the spectrometer pass through a thin window and are detected outside of the cryostat vessel in detector arrays consisting of plastic-scintillator paddles and photo-tubes. A cryogenic scattering target, connected to an independent cooling loop, is located along the axis, well within the central region of the spectrometer. Each of the eight coils has a total of 144 turns wound in 4 layers. The conductor is 20-strand NbTi Rutherford cable soldered into a Cu matrix, insulated with a

half-lapped layer of 0.1-mm Kapton, with an over-all cross section of 0.5 x 2.0 cm. It will carry a current of 5.0 kA at 4.5 K in a maximum magnetic field of 3.5 T. The conductor is wound on aluminum bobbins that are incorporated into permanent coil-case assemblies. The liquid-He cooling channels are located within the coil cases, and do not come into direct contact with the conductor. The plumbing of the channels is arranged to accommodate the forced flow of He gas for cool-down, and thermal siphoning in the steady state. The details of the mechanical, cryogenic, and electrical design of the spectrometer are discussed in [TD93].

The optimized spectrometer coil-configuration is illustrated in Figure 27. Less than half of the azimuthal angular range about the axial target is occupied with conductors ($\theta < 8.5°$ referred to Figure 22) and the diameter of the central (axial) aperture is of order 60 cm. Median-plane proton trajectories corresponding to $0.1 < Q^2 < 0.5\ GeV^2/c^2$, originating at points in a 20-cm long axial target are illustrated in the figure. It can be seen that the distribution of Q^2 at the focal plane is independent of where in the target the respective particle originated, and indicates that the desired zero-magnification condition $(x/t) \sim 0$ has been achieved. Central trajectories are deflected by angles between 35° and 85°, and the focal plane can be well shielded from target line-of-sight. The distribution of constant-Q^2 proton trajectories over the focal surface corresponding to the full azimuthal acceptance of one sector of the toroid ($-12° < \phi < +12°$) is shown in more detail in Figure 29. If the radial dependence of the magnetic fields were uniform in ϕ, the Q^2 curves would appear to be arcs of circles. Fields near the conductors are somewhat higher than those on the median plane and tend to bend nearby trajectories more strongly, giving rise to the somewhat 'elliptical' and forward-bending contours that are seen in the figure. The focal surface lies at an average angle of about 40° with respect to the central axis. The Q^2 dispersion is quite reasonable. We note that some of the detectors will lie relatively near the spectrometer coils where the magnetic fields are high, and that, consequently, light guides will be required between the scintillators and respective phototubes. These latter can be positioned to the rear of the spectrometer where the fields are much lower (Section 3.6). Local magnetic shielding of phototubes in the higher field region is a less desirable option because of the potential for asymmetric distortion of the spectrometer optics.

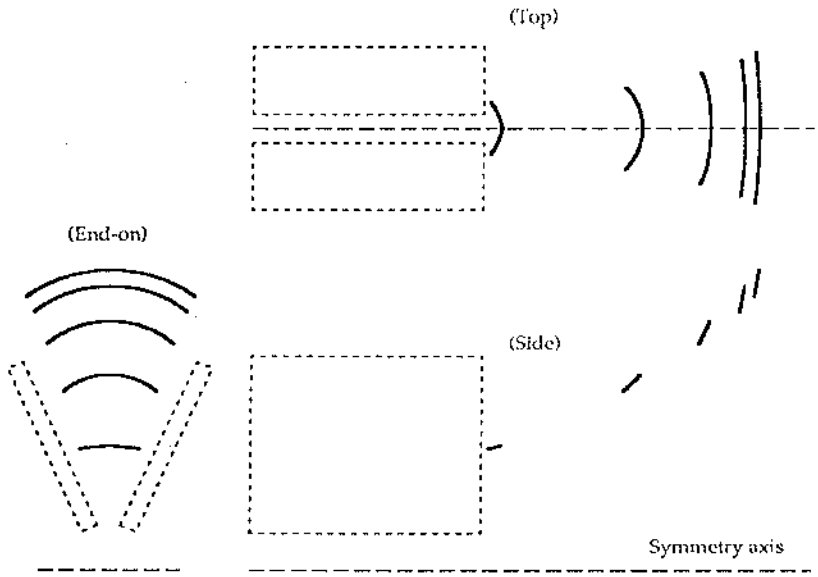

Figure 29. Orthographic projections of lines of constant Q^2 on the focal surface of one sector for $Q^2 = 0.1, 0.2, 0.3, 0.4$, and $0.5\ GeV^2/c^2$. The locations of the two adjacent coils are indicated by the dashed boxes

In the following Sections 3.2 to 3.10, we will evaluate the expected performance of the optimized super-conducting G^0 spectrometer in greater quantitative detail.

3.2. Magnetic Field and Trajectory Computations

Because the super-conducting Rutherford cable occupies a relatively small fraction of the cross sectional area of the conductor [TD93], it is natural to approach the problem of computing realistic magnetic fields for the SC toroidal spectrometer by considering filamentary currents. Beyond this however, the method is particularly convenient in that the location of a filamentary current-segment can be easily specified by two points in space, and the contribution to the magnetic fields determined from a rather simple analytic Biot-Savart expression:

$$B_\phi = \left(10^{-4}\right)\cdot\frac{I}{R}\cdot\left[\sin\alpha_{n+1} - \sin\alpha_n\right] \quad \text{(kG, A, cm).} \tag{12}$$

R is the normal distance to a line passing through the segment, and the α's are the angles to the segment endpoints ordered sequentially around the circuit. One additional advantage to this method is the relative ease with which computations for more general conductor geometries can be verified by comparisons with the limiting cases of infinite wires and circular loops which have very simple analytic solutions.

We note that in modeling and optimizing a large device with eight coils, limited symmetry, and long particle-paths, the speed of any computation becomes an important consideration. In this regard, the way in which circular arcs of conductor are approximated by linear current-filament segments is of concern. The simplest approximation , and the easiest to construct, uses the chords that connect points on the arc of radius r. A better method, and one which generally requires many fewer segments for a given precision, uses the chords of a circle of radius R constructed so that the average deviation between a chord and a segment of arc of radius r is zero over its length:

$$R = 2 \cdot r \cdot \frac{\sin(\theta / 4)}{\sin(\theta / 2)}. \tag{13}$$

The parameter θ is the angle subtended by the segment. It can be shown that the maximum deviation between the constructed chord and the arc segment anywhere along its length is

$$\Delta_{max} = R \cdot \frac{(1 - \cos(\theta / 2))}{2}. \tag{14}$$

The corresponding RMS deviation is somewhat less than about half as large as Δ_{max}.

The actual particle trajectories were computed with a fast routine that integrates over circular arcs, the radii of which are determined by a quadratic extrapolation of the average magnetic field over the arc length. The scale of the integration step is set by a transit-time parameter DT.

The absolute accuracy of a trajectory computation depends on the three parameters: DT, θ, and N, the number of current filaments used to approximate the cross section of the real coil. In the interest of minimizing computation time, it is important that DT and θ be as large, and N as small as possible consistent

with the size of the spectrometer and the precision required in the result. An effort was made to understand the ways in which these quantities are coupled.

The required computational precision depends on the demands of the experimental measurement and on the intrinsic optical-performance of the spectrometer. It also is influenced by the tolerances that are maintained in the fabrication and alignment of the device. These latter issues will be discussed in detail in Section 3.8. In the course of the initial optimization and survey work, it was concluded that an absolute accuracy of order ~ ± 1 mm in the computed location of particle tracks in the vicinity of the detectors would be sufficient for the purpose of establishing and evaluating the spectrometer design. Relative accuracies can be expected to be considerably better than what is reflected in an absolute limit because changes in the integral magnetic fields (BdL) across the useful volume of the spectrometer tend to be monotonic and slow.

Because both the scale and the actual configuration of the spectrometer have an important impact on magnetic-field gradients and the lengths of trajectories, reasonable values for the parameters DT, θ, and N were established in three stages.

First, we note that, in lowest order, the fields of a sector of a toroidal spectrometer are similar to the fields of a clamshell spectrometer, and that these, in turn, are not unlike the fields associated with an infinite line of current. The latter fields are easily computed (equation 12); but, more importantly, the path of a particle moving in these fields can be expressed in closed parametric form:

$$R(k,\lambda) = R(k,0)\cdot e^{k\cdot(\cos\lambda - 1)} \qquad \text{(cm)}$$

$$Z(k,\lambda) = R(k,0)\cdot k\cdot \int_0^{\lambda} \cos\delta \cdot e^{k(\cos\delta - 1)}\cdot d\delta \qquad \text{(cm)}$$

$$k = \left(1.668\cdot 10^4\right)\cdot \frac{P}{I} \qquad \text{(MeV/c, A)} \qquad (15)$$

At each point, the independent parameter λ corresponds to the slope of the tangent to the particle path in the Z-R plane. In a context that is similar to that of the toroidal spectrometer, these equations provide a simple means of both verifying the trajectory-computation routine and understanding its dependence on DT. As an example, a value of DT = 5×10^{-10} sec results in deviations between

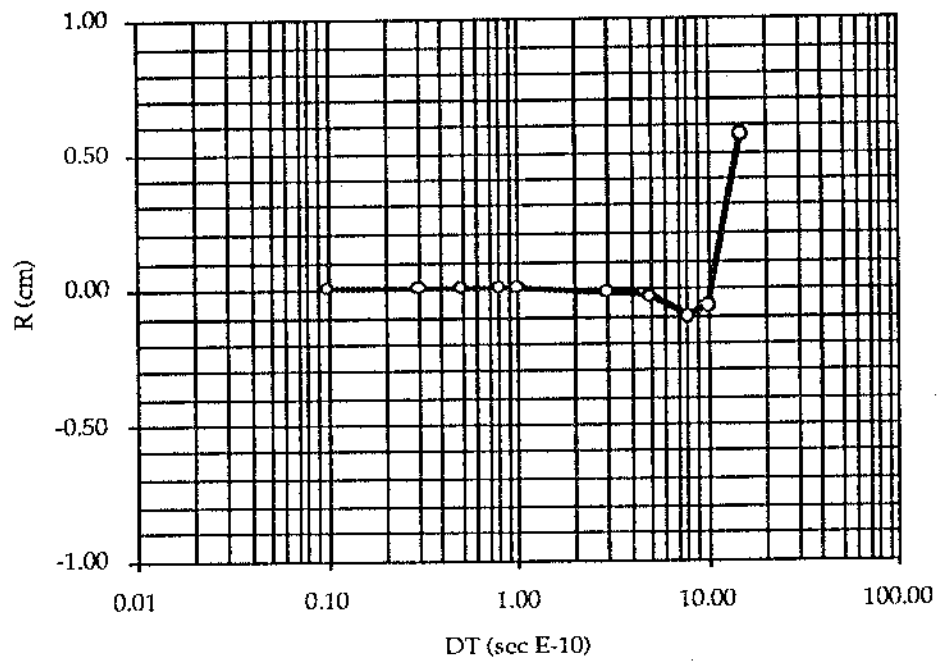

Figure 30. Relative radial coordinate at z = 3.5 m, corresponding to $Q^2 = 0.3\ GeV^2/c^2$, as a function of the trajectory integration parameter, DT.

the analytically and numerically computed trajectories that are less than 0.5 mm over path lengths of 4 m .

Next, we consider trajectories computed in the fields of a realistic SC toroid. Figure 30 shows the intersection of a proton trajectory, corresponding to $Q^2 = 0.3\ GeV^2/c^2$, with a plane situated at z = 350 cm, plotted as a function of the parameter DT. The intersection is expressed as a deviation from its asymptotic value of R = 210.81 cm. It can be seen that the trajectory converges rapidly, and that for $DT < 10^{-9}$ sec the absolute accuracy is of order ± 1 mm. For $DT < 5 \times 10^{-10}$ sec, it is better than 0.5 mm. This result is similar to that reported in the previous paragraph for absolute convergence to an analogous analytic trajectory.

Finally, we examine the ways in which the accuracy of a trajectory computation depends on the particular distribution of filaments, as specified by N and θ, that is chosen to represent the currents in a real coil. As an absolute reference we can take the case where each turn of the embedded SC Rutherford-cable is modeled

Table 8. Proton trajectory intersections with a plane at z = 300 cm for various filamentary approximations to the real coil. $\phi = 10°$, and $DT = 5 \times 10^{-10}$ sec.

θ (deg.)	N 8 coils	N: coils 1 and 2	N: coils 3 to 8	R (cm) Q^2=0.1	R (cm) Q^2=0.2	R (cm) Q^2=0.3	R (cm) Q^2=0.5	cpu (rel.)
4.5°	**144**	**144**	**144**	**59.28**	**164.54**	**201.12**	**225.03**	**1.00**
6.0°	144	144	144	59.30	-	201.14	225.04	0.75
9.0°	144	144	144	59.37	-	201.21	225.09	0.50
9.0°	->	36	9	59.18	164.50	201.10	225.02	0.06
9.0°	->	18	9	59.13	164.47	201.08	225.00	0.04
9.0°	->	9	9	58.97	164.37	201.00	224.93	0.03

with a separate filament (e.g.. N = 144), and where, for the circular arcs, $\Delta_{RMS} < 0.1$ mm (i.e. $\theta = 4.5°$). To be specific, we consider an eight-coil spectrometer having the geometry illustrated in Figure 24. We examine the intersections of proton trajectories corresponding to $Q^2 = 0.1, 0.2, 0.3$, and 0.5 with a plane located at z = 300 cm. In order to enhance the sensitivity of the computations to the micro structure of the coils, we also take the initial azimuthal angle of the trajectories to be $\phi = 10°$. The radial coordinates of the respective intersections for the reference case are listed in the first row Table 8. It can be seen from the table that the accuracy of the computations decreases slowly as θ is increased, with the greatest sensitivity to the change being at low Q^2. We might expect that the trajectories in a particular sector would show greater sensitivity to the number of filaments used to represent the coils that bound that sector (e.g.. coils 1 and 2) than to the number used in coils that are farther away (e.g.. coils 3 to 8). A number of examples for various values of N in the near and far coils are also listed in Table 8. It can be seen that, for instance, a [9° x 18 x 9] approximation generally can meet the absolute accuracy requirement while saving a factor of 25 in computation time relative to the full reference model.

3.3. Focal Surface

Points on the zero-magnification focal surface were determined by locating the minimum dispersion-plane waist associated with bundles of trajectories coming from a 20-cm long axial target. A grid of focal-points was computed for fifteen Q^2 values in the range of 0.08 to 0.60 GeV^2/c^2 at initial azimuthal angles $\phi = 0, 30, 60, 90, 120, 150$, and 180 mr as measured from the sector median-plane. The coordinate system is illustrated in Figure 31. It was found that the intersection of the focal surface with the median-plane ($\phi = \Phi = 0$) could be very well parameterized by a quadratic relation between the cylindrical coordinates R and z (axis), as is shown in Figure 32. For other azimuthal angles, the radial dependence of the surface differs from the median-plane value by a term that varies with Φ^2. The complete parameterization of the focal surface is given by

$$R(\Phi, z) = [b + m \cdot (z - h)^2] - [B \cdot z^2 \cdot \sin(\frac{\pi}{D}(z - H))] \cdot \Phi^2 \quad . \qquad (16)$$

The parameters in this equation were determined from least-square fits to the data set and are listed in Table 9. The dimensions of R and z are in cm, and Φ in mrad. All of the curvatures vary slowly, which has positive implications for the instrumentation of the focal surface with shaped plastic scintillators.

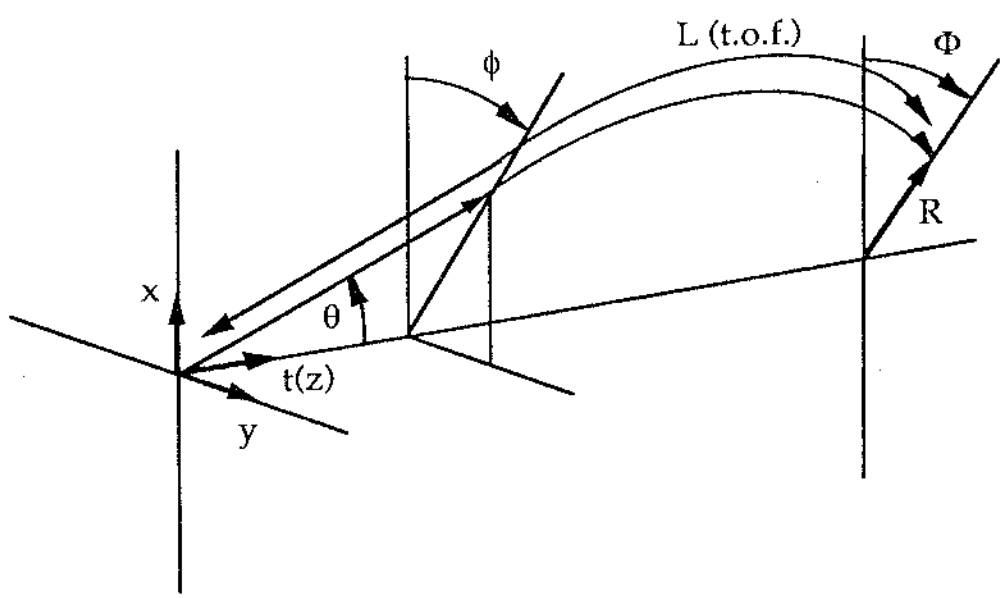

Figure 31. Definition of the coordinate system . The t(z)-axis is the symmetry axis of the spectrometer, and the vertical lines lie in the median plane of a sector.

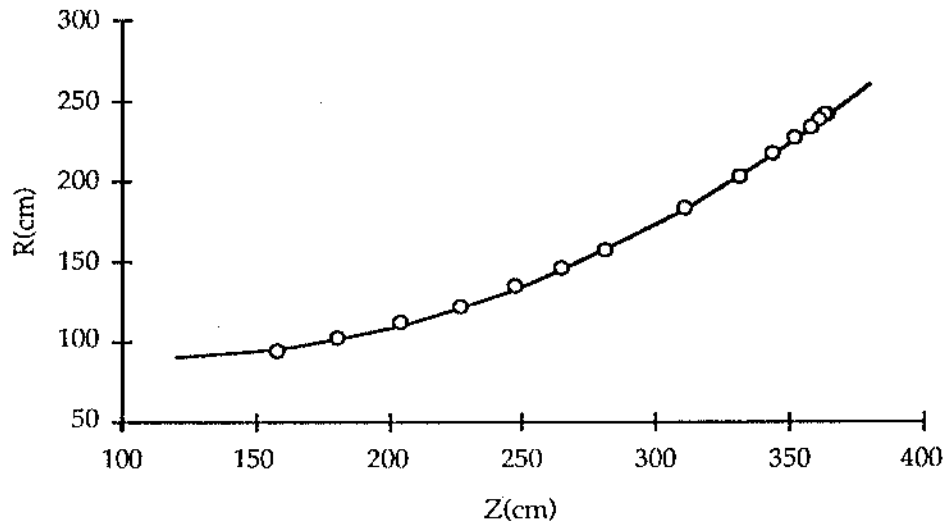

Figure 32. Median-plane focal surface. A quadratic fit to fifteen points corresponding to values of Q^2 in the range 0.08 to 0.60 GeV^2/c^2 is indicated.

Table 9. Focal Surface Parameterization

b	90.388
m	2.3736×10^{-3}
h	113.22
B	1.203×10^{-9}
D	122.0
H	264.0

3.4. Optics Characterization

In order to examine the characteristics of this spectrometer in greater quantitative detail we have determined effective first order transfer-matrix elements which relate changes in experimentally observed quantities at the focal surface to changes in initial variables. Of interest are the target-to-focus path length, L_f, which is related to the time-of-flight; the radial distance, R_f, from the symmetry

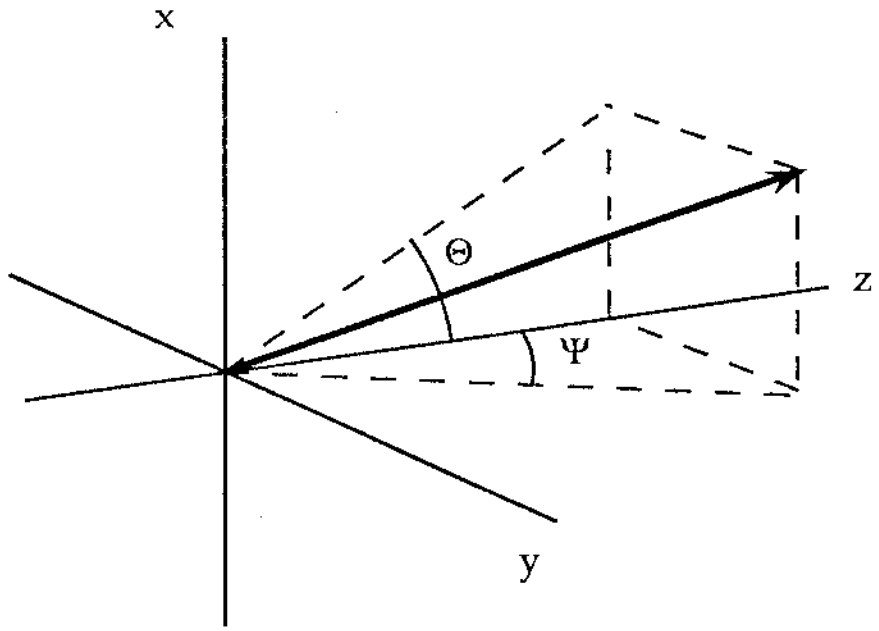

Figure 33. Definition of the angles Θ and Ψ which define the direction of a trajectory at the focal surface.

axis to the point of intersection with the focal surface; and the azimuthal angle, Φ_f, that the radial vector to the point of intersection makes with the median-plane of the spectrometer sector. The coordinate system is illustrated in Figure 31. It is also useful to know the direction of a particle trajectory as it intersects the focal surface. The direction can be specified by the angles Θ and Ψ as shown in Figure 33.

It is convenient to expand the matrix elements about a momentum- and phi-dependent central ray corresponding to elastically scattered protons from the center of the target:

$$V_f(p,\phi) = V_o(p,\phi) + \Sigma\ (V\,|\,w)\Delta w$$

$$V_o(p,\phi) = (ap^3+bp^2+cp+d) + (ep^3+fp^2+gp+h)\,|\,\phi\,| + (ip^3+jp^2+kp+l)\phi^2$$

$$(V\,|\,w) = (Ap^3+Bp^2+Cp+D) + (Ep^3+Fp^2+Gp+H)\,|\,\phi\,| + (Ip^3+Jp^2+Kp+L)\phi^2 \qquad (17)$$

where the focal surface coordinates $V_f = \{R_f, Z_f, L_f, \Phi_f, \Theta_f, \Psi_f\}$ are related to the central trajectory coordinates $V_o = \{R_o, Z_o, L_o, \Phi_o, \Theta_o, \Psi_o\}$, and to the initial coordinates $w = \{\theta, t(z), y, x, I\}$, by the p- and ϕ- dependent matrix elements $(V \mid w)$. Deviations, $\Delta w = (w - w_o)$, are measured with respect to the central coordinates $\{\theta_o, \phi_o, I_o, x_o, y_o, t_o\} = \{\theta_o(p(Q^2)), 0, 720000, 0, 0, 44\}$. The dimensions are mrad, MeV/c, Å, and cm, and

$$\theta_o(p,Q^2) = \cos^{-1}\left[\frac{1}{p}\cdot\left(P_e - (P_e - M\cdot\frac{Q^2}{2M^2})\cdot\cos\left[2\cdot\sin^{-1}\sqrt{\frac{\frac{M}{2}\cdot\frac{Q^2}{2M^2}}{\frac{P_e^2}{M} - P_e\cdot\frac{Q^2}{2M^2}}}\right]\right)\right] \tag{18}$$

where

$$\frac{Q^2}{2M^2} = \sqrt{1+\left(\frac{p}{M}\right)^2} - 1 \tag{19}$$

The momentum of the incident electron beam is $P_e = 3000$ MeV/c. The coefficients in the equations (17) are listed in Tables 10 to 15, and were obtained from least-square fits to partial derivatives computed for trajectories corresponding to $Q^2 = 0.08, 0.10, 0.12, 0.14, 0.16, 0.20, 0.25, 0.30, 0.35, 0.40, 0.45, 0.50$ and 0.55 GeV^2/c^2, at $\phi_o = 0, 30, 60, 90, 120, 150, 180$, and 210 mr. This parameterization was found to provide a very good fit to the trajectory data.

Because of its very large acceptance, an overview of the optical characteristics of this spectrometer is best obtained by considering plots of the quantities of interest as functions of Q^2 and the azimuthal angle ϕ. The magnification, or $(R \mid z)$ transfer-matrix element is plotted in Figure 34. It can be seen that the magnification is quite small in the central region and for lower Q^2, and that even at the extremes of the acceptance it has values that remain less than about 0.3. The larger magnifications are associated with longer trajectories, and with the deviations from azimuthal uniformity found in the magnetic fields near the coils. We next consider the momentum dispersion and the dispersion of the scattering angle θ. These quantities are plotted in Figures 35 and 36 respectively. The momentum dispersion is reasonably large. It has little ϕ dependence, and is almost constant for larger values of Q^2, but then drops rapidly below $Q^2 \sim 0.2$.

Table 10. Focal-surface: central-ray parameters.

	Z	R	Φ	L	Θ	Ψ
a	6.072E-07	-1.071E-06	4.939E-13	1.248E-07	7.064E-06	3.671E-12
b	-1.929E-03	1.357E-03	-8.047E-10	-1.169E-03	-1.536E-02	-6.655E-09
c	1.942E+00	-1.602E-01	3.273E-07	1.626E+00	1.152E+01	3.833E-06
d	-2.663E+02	4.574E+01	-1.694E-05	-2.090E+02	-2.494E+03	-6.952E-04
e	7.088E-10	-5.586E-10	-2.295E-09	2.942E-10	1.675E-09	8.115E-09
f	-1.539E-06	8.302E-07	3.847E-06	-8.484E-07	-3.515E-06	-1.795E-05
g	1.052E-03	-3.551E-04	-1.625E-03	6.955E-04	2.433E-03	1.421E-02
h	-2.211E-01	4.116E-02	1.348E+00	-1.651E-01	-5.274E-01	-3.147E+00
i	-2.502E-11	-9.417E-13	3.159E-12	-2.101E-11	-2.249E-12	2.820E-11
j	4.398E-08	4.739E-09	-5.119E-09	3.814E-08	1.025E-08	-4.974E-08
k	-2.437E-05	-5.082E-06	3.764E-06	-2.222E-05	-1.025E-05	2.902E-05
l	4.004E-03	1.199E-03	-1.204E-03	3.854E-03	1.305E-03	-6.184E-03

Table 11. Focal-surface: (V | θ) parameters.

	(Z | θ)	(R | θ)	(Φ | θ)	(L | θ)	(Θ | θ)	(Ψ | θ)
A	4.156E-09	-1.193E-09	-6.939E-16	7.327E-10	2.539E-08	-7.943E-16
B	-8.833E-06	-6.289E-07	1.831E-12	-3.513E-06	-4.715E-05	1.185E-12
C	6.452E-03	3.320E-03	-1.655E-09	4.410E-03	2.830E-02	-5.363E-10
D	-9.815E-01	-8.709E-01	6.719E-07	-6.573E-01	-4.535E+00	2.057E-07
E	1.633E-11	6.170E-12	-3.452E-11	1.632E-11	1.209E-11	9.538E-12
F	-2.779E-08	-1.114E-08	6.099E-08	-2.782E-08	-2.007E-08	-1.725E-08
G	1.458E-05	6.424E-06	-3.216E-05	1.468E-05	1.101E-05	1.237E-05
H	-2.336E-03	-1.160E-03	2.644E-03	-2.376E-03	-1.813E-03	-3.874E-03
I	2.848E-13	1.291E-14	1.532E-13	2.953E-13	-4.877E-13	-3.087E-13
J	-5.256E-10	-3.167E-11	-2.213E-10	-5.444E-10	8.506E-10	5.950E-10
K	2.975E-07	1.277E-08	8.613E-08	3.037E-07	-4.830E-07	-3.762E-07
L	-5.283E-05	-1.767E-06	-7.068E-06	-5.314E-05	8.827E-05	7.516E-05

Table 12. Focal-surface: (V | z) parameters.

	(Z | z)	(R | z)	(Φ | z)	(L | z)	(Θ | z)	(Ψ | z)
A	2.164E-09	2.659E-09	-1.472E-14	2.768E-09	-1.286E-07	-1.062E-14
B	-3.093E-06	-4.340E-06	2.631E-11	-5.168E-06	2.516E-04	2.077E-11
C	1.209E-03	2.197E-03	-1.348E-08	3.532E-03	-1.638E-01	-1.263E-08
D	-7.501E-02	-3.245E-01	3.884E-07	-1.808E+00	3.809E+01	1.182E-06
E	1.119E-11	-2.557E-12	3.112E-10	7.217E-12	-1.122E-10	-1.617E-10
F	-2.274E-08	-1.128E-09	-5.484E-07	-1.840E-08	1.886E-07	3.246E-07
G	1.397E-05	2.642E-06	2.920E-04	1.263E-05	-1.026E-04	-2.292E-04
H	-2.758E-03	-6.783E-04	-3.422E-02	-2.642E-03	1.722E-02	6.990E-02
I	-3.838E-13	-2.390E-13	-5.871E-13	-4.789E-13	1.708E-12	8.076E-13
J	5.327E-10	3.738E-10	7.820E-10	7.034E-10	-2.991E-09	-1.577E-09
K	-2.020E-07	-1.636E-07	-2.145E-07	-2.935E-07	1.701E-06	1.027E-06
L	2.358E-05	2.271E-05	-2.058E-05	3.895E-05	-3.057E-04	-2.138E-04

Table 13. Focal-surface: (V | y) parameters.

	(Z | y)	(R | y)	(Φ | y)	(L | y)	(Θ | y)	(Ψ | y)
A	-2.114E-14	1.510E-14	-1.309E-07	-3.111E-15	-5.463E-13	8.396E-08
B	5.487E-11	5.154E-13	2.508E-04	3.249E-11	1.024E-09	-1.712E-04
C	-4.023E-08	-1.783E-08	-1.490E-01	-3.349E-08	-6.162E-07	1.266E-01
D	6.517E-06	4.790E-06	3.021E+01	5.618E-06	1.152E-04	-3.474E+01
E	1.138E-10	1.598E-10	-4.808E-10	1.922E-10	6.253E-10	-2.337E-11
F	-2.469E-07	-2.922E-07	7.870E-07	-3.823E-07	-1.065E-06	3.789E-10
G	1.616E-04	1.647E-04	-4.175E-04	2.311E-04	5.700E-04	2.525E-05
H	-3.104E-02	-2.807E-02	7.073E-02	-4.120E-02	-1.001E-01	-1.019E-02
I	-7.332E-13	-4.550E-13	5.707E-12	-1.177E-12	-5.974E-12	1.086E-12
J	1.951E-09	9.986E-10	-9.094E-09	2.758E-09	1.093E-08	-1.261E-09
K	-1.549E-06	-7.469E-07	4.753E-06	-2.046E-06	-6.684E-06	3.534E-07
L	3.560E-04	1.646E-04	-8.731E-04	4.533E-04	1.332E-03	-6.062E-05

Table 14. Focal-surface: (V | x) parameters.

	(Z | x)	(R | x)	(Φ | x)	(L | x)	(Θ | x)	(Ψ | x)
A	-1.657E-09	-2.238E-09	3.831E-15	-1.668E-09	7.048E-08	-1.318E-16
B	2.156E-06	3.185E-06	-7.918E-12	1.757E-06	-1.329E-04	-1.084E-12
C	-8.021E-04	-1.420E-03	5.702E-09	-1.468E-04	8.071E-02	2.389E-09
D	6.997E-02	1.942E-01	-5.966E-07	-8.597E-01	-1.689E+01	-3.970E-07
E	-1.547E-12	3.237E-11	-1.936E-11	9.482E-12	1.349E-10	4.168E-11
F	2.654E-08	-3.897E-08	-2.506E-08	1.392E-08	-1.783E-07	-8.274E-08
G	-3.022E-05	1.081E-05	4.240E-05	-2.736E-05	6.422E-05	3.326E-05
H	8.037E-03	-1.501E-04	-1.985E-02	8.238E-03	-4.418E-03	-3.516E-03
I	-7.875E-13	-1.270E-12	6.827E-13	-1.267E-12	-3.816E-12	-8.912E-13
J	1.090E-09	1.947E-09	-6.288E-10	1.809E-09	5.977E-09	1.888E-09
K	-4.227E-07	-9.157E-07	2.112E-08	-7.471E-07	-2.903E-06	-1.250E-06
L	3.956E-05	1.324E-04	7.557E-05	8.252E-05	4.365E-04	2.740E-04

Table 15. Focal-surface: (V | I) parameters.

	(Z | I)	(R | I)	(Φ | I)	(L | I)	(Θ | I)	(Ψ | I)
A	-8.271E-12	-4.750E-12	3.880E-18	-6.229E-12	-1.738E-11	3.775E-18
B	1.582E-08	1.179E-08	-7.587E-15	1.343E-08	2.711E-08	-6.771E-15
C	-9.438E-06	-9.243E-06	4.788E-12	-9.132E-06	-1.078E-05	3.829E-12
D	1.227E-03	1.777E-03	-9.930E-10	1.271E-03	-6.501E-04	-6.711E-10
E	-2.187E-14	-1.080E-14	-1.313E-14	-2.324E-14	-1.343E-14	1.019E-14
F	3.659E-11	1.903E-11	2.538E-11	3.905E-11	1.980E-11	-2.349E-11
G	-1.905E-08	-1.065E-08	-1.579E-08	-2.047E-08	-8.877E-09	1.933E-08
H	3.059E-06	1.870E-06	3.808E-06	3.314E-06	1.029E-06	-6.311E-06
I	-2.097E-16	8.832E-17	-5.462E-17	-1.818E-16	5.404E-16	1.665E-16
J	4.097E-13	-1.439E-13	6.945E-14	3.593E-13	-9.199E-13	-3.289E-13
K	-2.494E-10	7.775E-11	-2.241E-11	-2.184E-10	5.010E-10	2.111E-10
L	4.781E-08	-1.244E-08	3.486E-10	4.216E-08	-8.619E-08	-4.338E-08

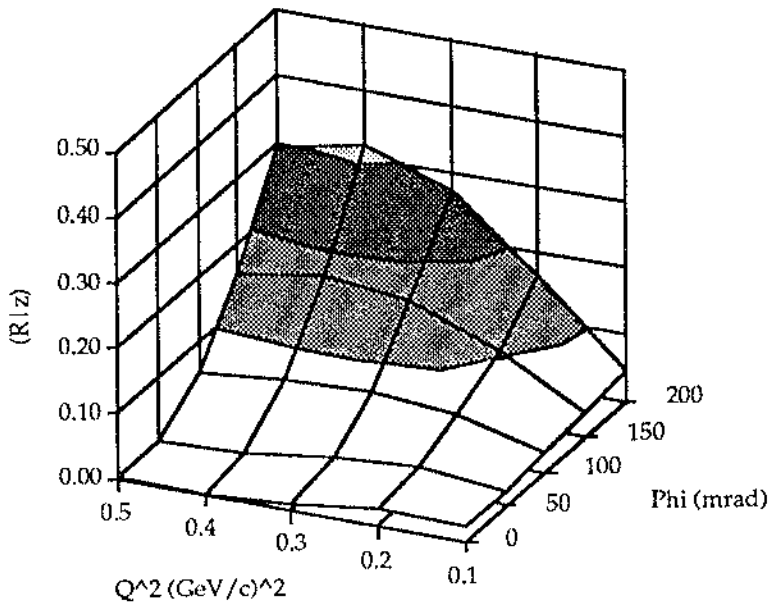

Figure 34. Spectrometer magnification plotted as a function of Q^2 and ϕ.

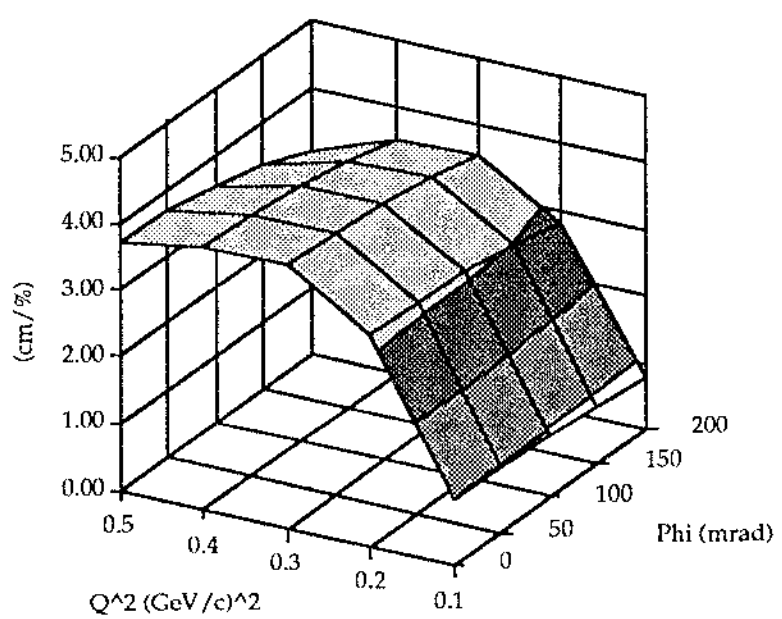

Figure 35. Momentum (p) dispersion plotted as a function of Q^2 and ϕ.

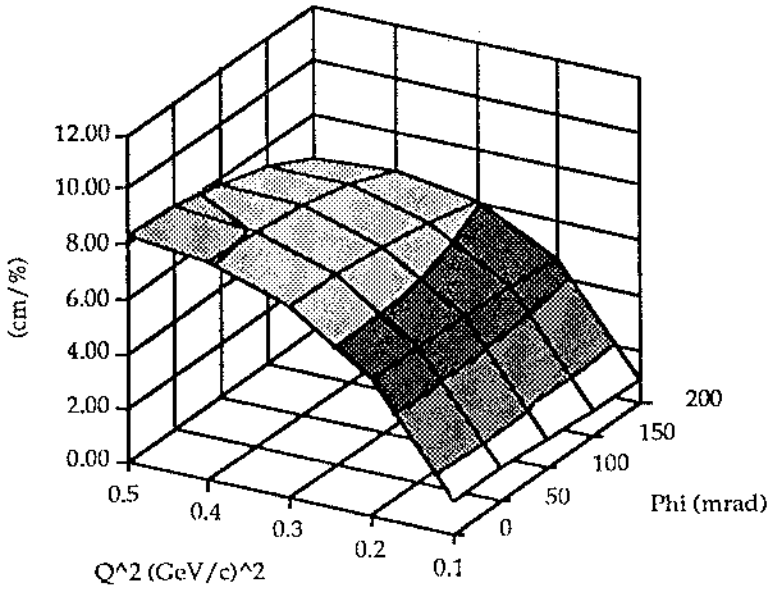

Figure 36. Scattering-angle (θ) dispersion plotted as a function of Q^2 and ϕ.

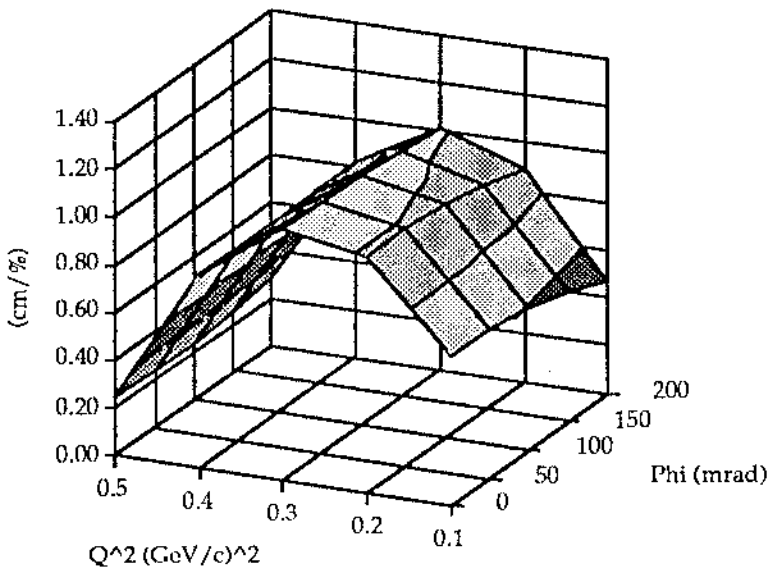

Figure 37. Q^2 dispersion plotted as a function of Q^2 and ϕ.

The dispersion of the scattering angle shows behavior that is very similar to that of the momentum.

From the point of view of the instrumentation and use of the spectrometer, we are actually more interested in the dispersion of the kinematic quantity, Q^2, across the focal surface than we are in that of p or θ. Figure 37 shows the dispersion in the momentum-transfer variable over the kinematic and angular acceptance of the spectrometer. It can be seen that there is little dependence on the angle ϕ, and that the dispersion is largest in the central range of the Q^2 bite.

In the following two sections, we will consider issues related to particle time-of-flight and resolution. The forward-proton and the backward-electron measurements will be discussed separately.

3.4.1. Proton Optics

The entries of Tables 10 to 15 can be used to generate expressions for the quantities R and T, which are measured experimentally by the scintillator ladder at the focal surface, in terms of the initial proton p and θ. Figure 38 shows lines of constant momentum (solid) and scattering angle (dashed) in the R-T coordinate space. Note that the abscissa has been plotted as $(R + m\phi^2)$ to remove the R dependence on the azimuthal angle that was discussed in Section 3.3. In practice this dependence will be eliminated by the actual azimuthal configuration of the plastic detectors (see Figure 29). It can be seen that a position measurement on the focal surface selects a family of momenta and angles which can be uniquely separated by the TOF cut. The open circles shown in Figure 38 indicate the location of five values of Q^2 in the range $0.1 < Q^2 < 0.5\ \mathrm{GeV}^2/c^2$. The intrinsic Q^2 resolution is quite good.

There are a variety of factors that will tend to degrade the intrinsic resolution of the spectrometer. Uncertainties associated with the point of interaction in a long scattering target can contribute to a spread in particle TOF, as can differences in trajectory lengths over the large azimuthal acceptance of a sector. Movement of the incident beam on the target, including intentional rastering, also can translate into smearing motions at the focal surface; and the stability of the magnetic field that defines the optics of the spectrometer is governed directly by the regulation of the coil current. However, under normal circumstances the uncertainties due

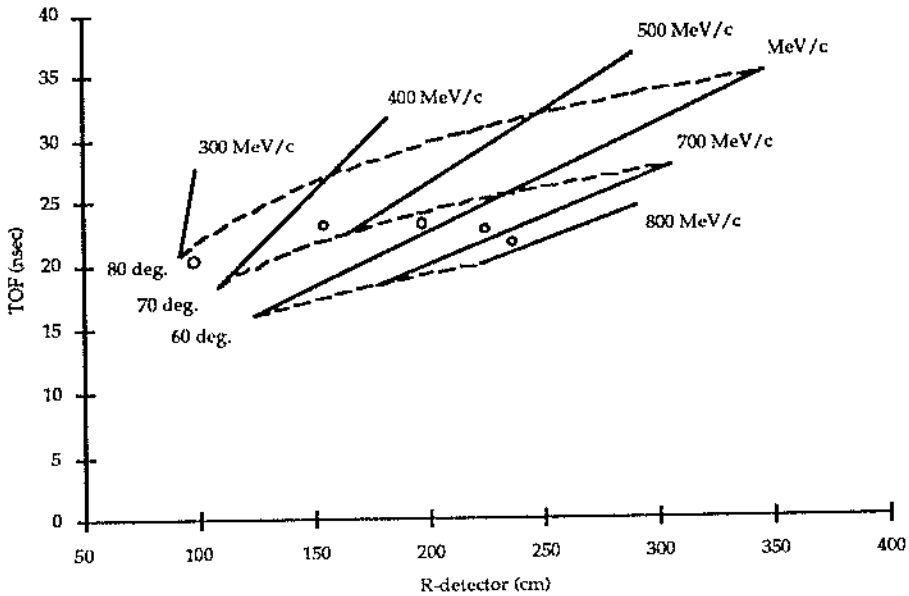

Figure 38. Intrinsic proton optics: TOF vs. position on the focal surface. Lines corresponding to constant p, and q are shown. The open circles indicate the locations of $Q^2 = 0.1, 0.2, 0.3, 0.4$, and $0.5\ GeV^2/c^2$.

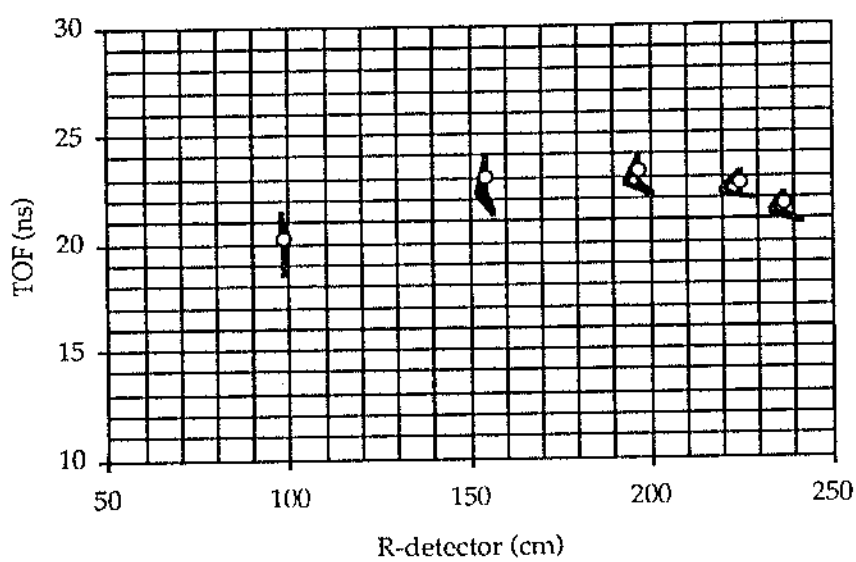

Figure 39. Proton optics: TOF vs. position on the focal surface. Indicated are the envelopes of points corresponding to $Q^2 = 0.1, 0.2, 0.3, 0.4$, and $0.5\ GeV^2/c^2$ coming from a 20-cm target, over the full azimuthal acceptance of the spectrometer.

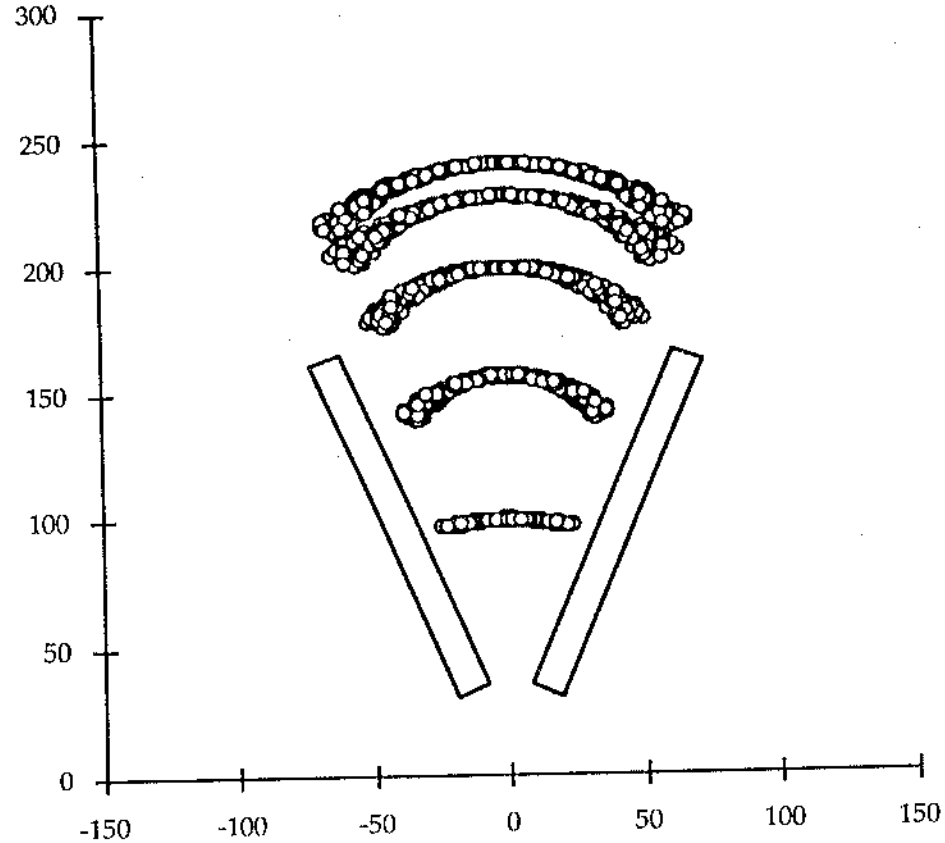

Figure 40. Proton optics: end-on view of the focal surface of one sector. Points corresponding to $Q^2 = 0.1, 0.2, 0.3, 0.4$, and $0.5\ GeV^2/c^2$ from a 20-cm target, are shown over the full azimuthal acceptance of the spectrometer.

to beam motion and current instability are relatively small. They will be examined separately in Sections 3.9 and 3.10. In order to investigate the larger effects of target length and azimuthal angle on the Q^2 resolution, a simple Monte Carlo calculation was done for protons corresponding to $Q^2 = 0.1, 0.2, 0.3, 0.4$, and $0.5\ GeV^2/c^2$. In each case, the particle origins were distributed over a 20-cm long axial target, and azimuthal angles were selected to fill the sector acceptance (nominally $-12° < \phi < +12°$). The results are plotted in the R-T plane of Figure 39. It can be seen that the envelopes of the points for each value of Q^2 remain tightly distributed in the vicinity of the central values, which are indicated by the open circles. Most of the TOF variation can be attributed to the 20-cm target length. It is clear that timing resolution much better than about

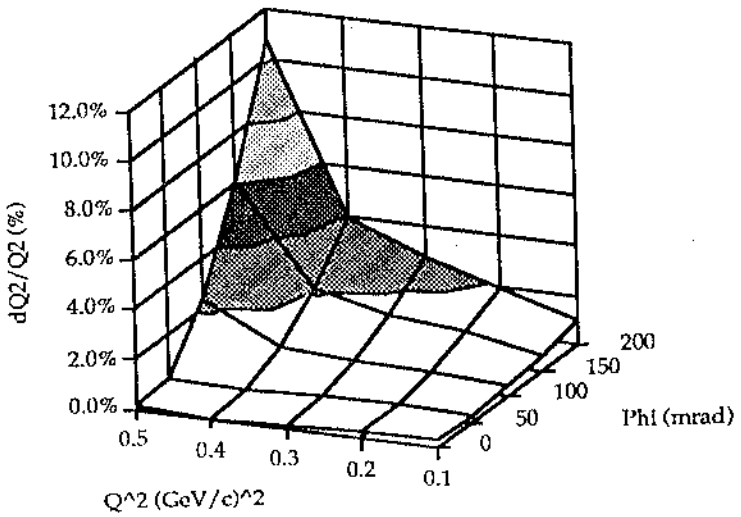

Figure 41. Proton optics: Q^2 resolution corresponding to particles from a 20-cm target over the full azimuthal acceptance of the spectrometer.

± 1 nsec is not required if a long target is employed, although the measurement of smaller time-intervals may be of value in dealing with background issues.

It is also of interest to examine the azimuthal distribution of trajectories at the focal surface. An end-on (y vs. x) plot of the Monte Carlo calculation for protons corresponding to $0.1 < Q^2 < 0.5\ \mathrm{GeV}^2/c^2$ in increments of 0.1 is shown in Figure 40. It can be seen that most of the reduction in the radial (R) resolution that appears in Figure 39 occurs at the extremes of the azimuthal acceptance.

The results of the Monte-Carlo computation can be combined with the dispersion functions that were determined in the previous section to provide a quantitative estimate of the kinematic resolution that can be achieved with simple detectors. The effective Q^2 resolution across the focal surface is plotted in Figure 41. We see that over most of the acceptance, the Q^2 resolution is on the order of a few percent or less, and that even at large azimuthal angles it is always better than ~ 10 %. This performance satisfies the design resolution-requirement. For reference, the momentum and scattering-angle resolutions are given in Figures 42 and 43 respectively.

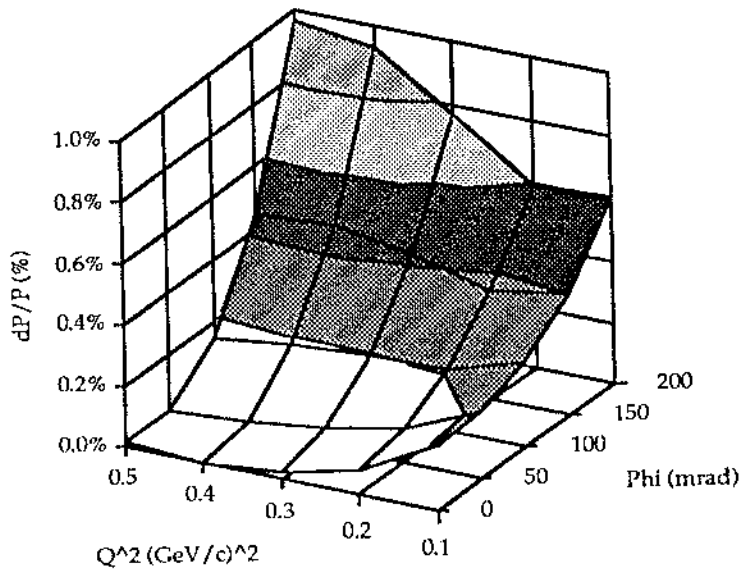

Figure 42. Proton optics: Momentum resolution corresponding to particles from a 20-cm target over the full azimuthal acceptance of the spectrometer.

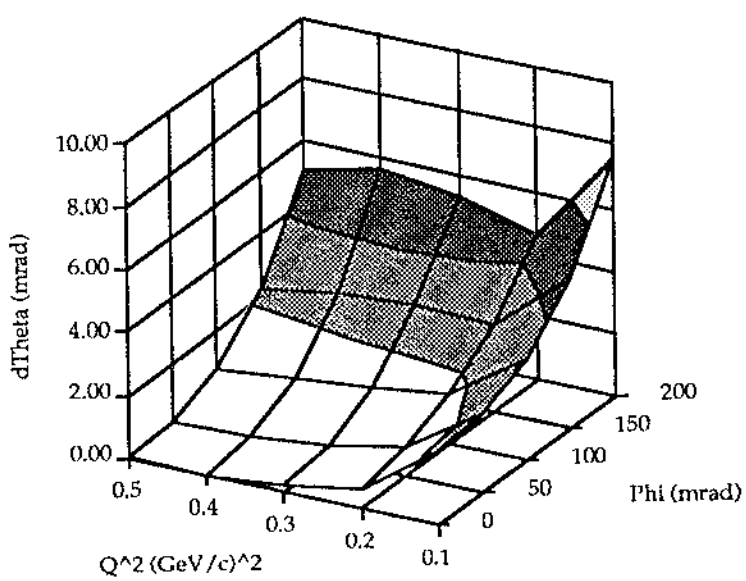

Figure 43. Proton optics: θ resolution corresponding to particles from a 20-cm target over the full azimuthal acceptance of the spectrometer.

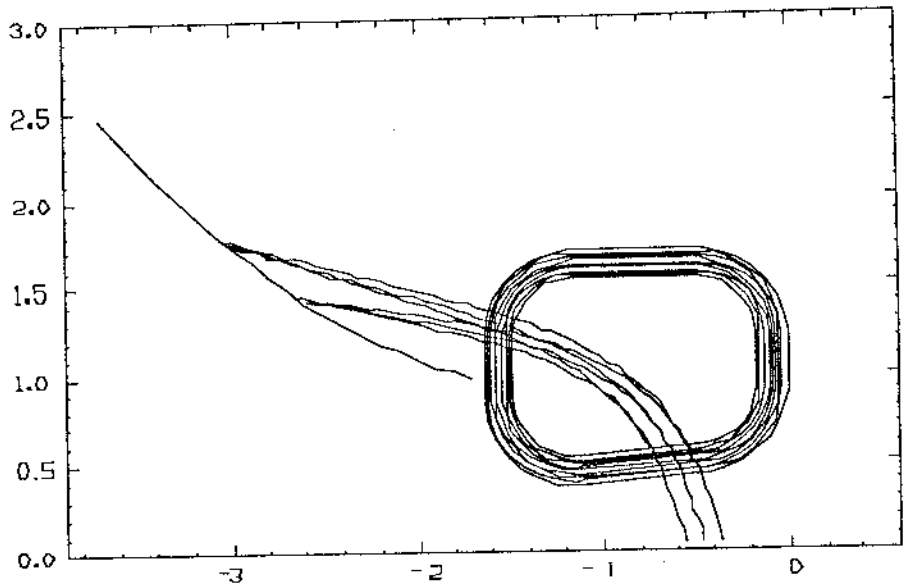

Figure 44 Electron optics: Spectrometer rotated to measure electrons scattered at 110°. Shown are elastic and threshold-inelastic electrons corresponding to $Q^2 = 2\ GeV^2/c^2$. Full magnetic field.

3.4.2. Electron Optics

For the backward electron-measurements the spectrometer is turned by 180°. At a scattering angle of $\theta = 110°$, typical trajectories corresponding to elastic and inelastic (threshold pion) scattering are illustrated in Figure 44. As was discussed in Section 1.3.3 above, because the electrons of interest for the backward measurement are relativistic, time of flight does not provide the relatively clean scattering-angle and momentum separation that is possible in the case of forward protons. This can be seen from Figure 45. The open points show the R-T focal-surface locations of electrons scattered at $\theta = 110°$ (70°), for p = 200, 250, 300, and 350 MeV/c. The Lines contiguous to each point indicate the range of variation, for each momentum, that corresponds to a change in scattering angle of ± 2.5°. The respective momenta have been moved onto an appropriate part of the focal surface by reducing the magnetic fields of the spectrometer to 65 % of the peak value. Notice that the lines of constant-p and constant-θ are compressed, and almost lie along a single curve in the R-T space. It is clear from the figure that the actual momentum resolution that is achieved

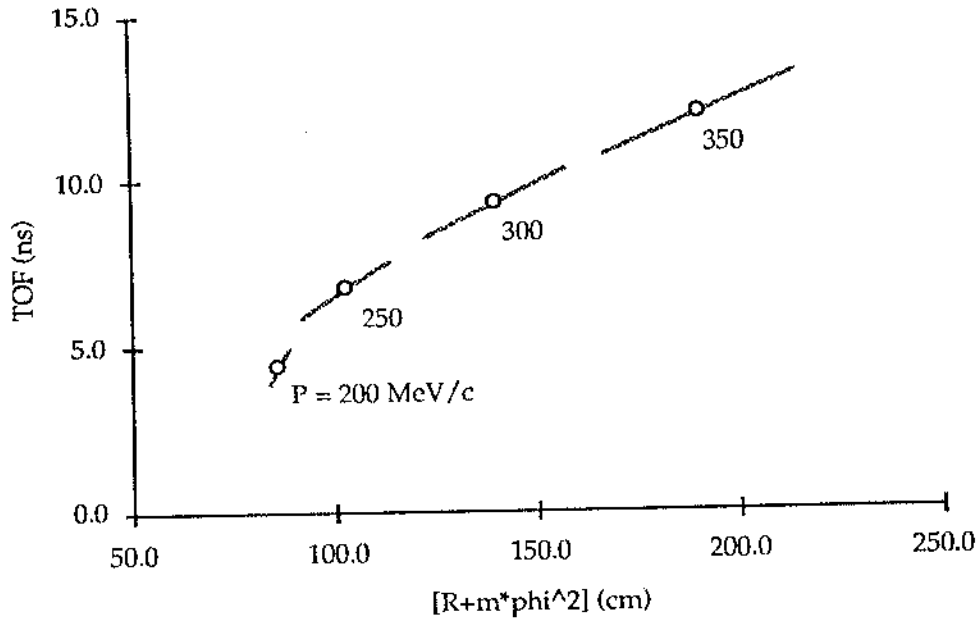

Figure 45. Intrinsic electron optics: Focal-surface intercept and TOF dependences on p and θ. The open points correspond to θ = 110° at the momentum indicated. The lines contiguous to each point indicate scattering-angle variations of ± 2.5°. 65 % of full magnetic field.

for backward electron measurements will depend on how well the angular acceptance of the spectrometer is defined by collimation.

In Section 1.3.3 we also noted that, for the backward-electron configuration of the spectrometer, a relatively smaller range of Q^2 will be dispersed over the fixed focal-surface detectors than will be the case for the forward proton measurement. This effect can be understood by considering an expression for the variation in the focal surface coordinate with changes in Q^2:

$$\frac{dR}{dQ^2} = (R|p)\cdot\frac{\partial p}{\partial Q^2} + \delta\cdot(R|\theta)\cdot\frac{\partial\theta}{\partial Q^2} \quad . \tag{20}$$

The general kinematic derivatives $(\partial p / \partial Q^2)$ and $(\partial\theta / \partial Q^2)$ were listed in Table 4 for the proton and electron experiments. The matrix elements $(R|p)$ and $(R|\theta)$ are the only spectrometer specific terms in the expression, and the factor δ modifying $(R|\theta)$ is equal to +1(-1) for forward(backward) measurements. As an example, we consider a comparison of the two the cases for

Table 16 A comparison of the rates of change of the focal surface coordinate R with Q^2 for forward protons and backward electrons. In both cases, $Q^2 = 0.3\ GeV^2/c^2$. The magnetic field is reduced by 30% for the electrons.

	$(R\|p)$ cm/MeV	dp/dQ^2 GeV/GeV^2	δ	$(R\|\theta)$ cm/deg	$d\theta/dQ^2$ deg/GeV^2	dR/dQ^2 cm/GeV^2
protons	+0.693	+1.05	+1	+10.45	- 34.5	+ 367.1
electrons	+0.715	-0.53	-1	+ 9.21	+434.8	-4383.5

$Q^2 = 0.3\ GeV^2/c^2$. All of the contributions to equation (20) are listed in Table 16, and it can be seen that dR/dQ^2 is actually about a factor of 12 larger for the backward-electron measurement than for the forward-proton one. An examination of the entries in the table shows that this difference is largely due to the order-of-magnitude difference in $dQ^2/d\theta$ between the forward and backward kinematics. The disparity is exacerbated to some extent by the fact that the terms of equation (20) enter as a sum in the case of electrons, and as a difference for protons. If this situation could be reversed by re configuring the $(x|x) = 0$ optics to change the sign of the $(R|\theta)$ matrix element, dR/dQ^2 would be increased by a factor of three for the protons, but be reduced by only about 15% for the electrons. The sign change would require an outward-bending spectrometer orientation [La91a], and the focal surface would need to be three times longer than that of the presently proposed device to keep the same proton acceptance. The obvious disadvantages of this course outweigh the rather small improvement that would be obtained in the backward electron acceptance.

It is of some interest to note from the entries in the table that the fore and aft difference in dR/dQ^2 would be much reduced if the spectrometer were configured so that $(R|\theta) = 0$. But, as can be seen from the value of $d\theta/dQ^2$, the scattering-angle acceptance of the spectrometer would have to be unrealistically large in order to take advantage of this situation. In practice, the angular acceptance of $(x|\theta) = 0$ spectrometers is always strongly limited by geometric aberrations.

The lower limits on resolution associated with the extended target and the large ϕ-acceptance were examined, and were found to be similar to what was observed for forward protons. This can be seen from Figure 46, which shows the envelopes corresponding to typical backward-electron distributions for elastic

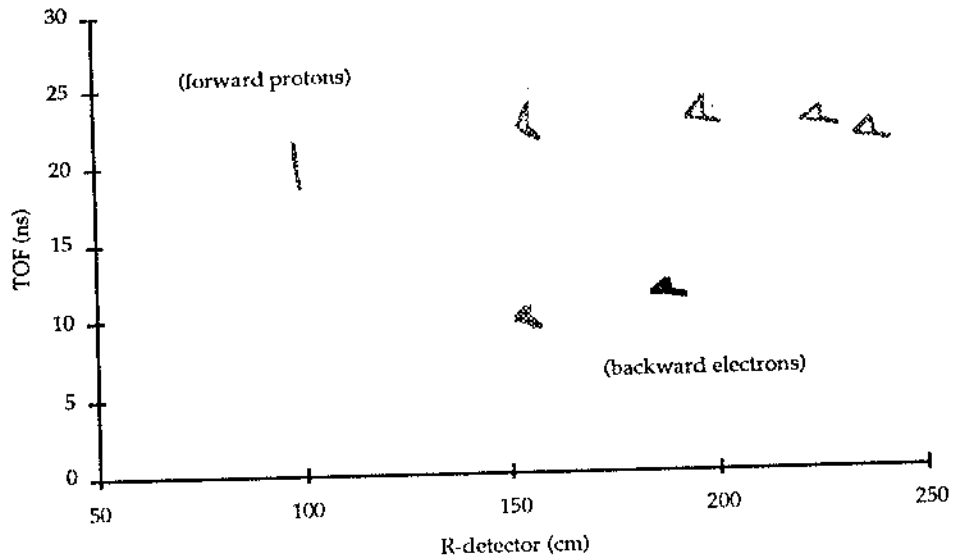

Figure 46. Electron optics: TOF vs. position on the focal surface. Indicated are the envelopes of points corresponding to elastic and threshold-inelastic scattering at $Q^2 = 2.0\ GeV^2/c^2$ coming from a 20-cm target, over the full azimuthal acceptance of the spectrometer. 90 % of full magnetic field. The proton envelopes of Figure 39 are shown for reference.

and inelastic scattering, as well as an overlay of the forward-proton distributions taken from Figure 39.

The minimum momentum-resolution that is required for each backward-electron measurement, at a particular Q^2, is determined by the need to separate the elastic scattering from associated inelastic scattering. This minimum resolution is plotted in Figure 47. If a finite scattering-angle acceptance is considered, the clean separation of elastic and inelastic particles that is evident in Figure 46 is smeared in the manner shown in Figure 48. The trajectory envelopes plotted in the figure reflect contributions from a 20-cm target, the full azimuthal acceptance, and $\Delta\theta$ =50 mrad. The heavy line corresponds to elastic events, and the lighter one to threshold inelastic. A plot of the maximum value of $\Delta\theta$ that is consistent with the minimum momentum-resolution restriction is given as a function of Q^2 in Figure 49. The corresponding solid angle, $\Delta\Omega$, is shown in Figure 50. Up to $Q^2 \sim 0.5$, the solid angle is in the range $800 > \Delta\Omega > 550$ mstr. For backward electrons, much higher values of Q^2 than $0.5\ GeV^2/c^2$ are accessible with this spectrometer. The actual limits on these measurements will reflect the falling

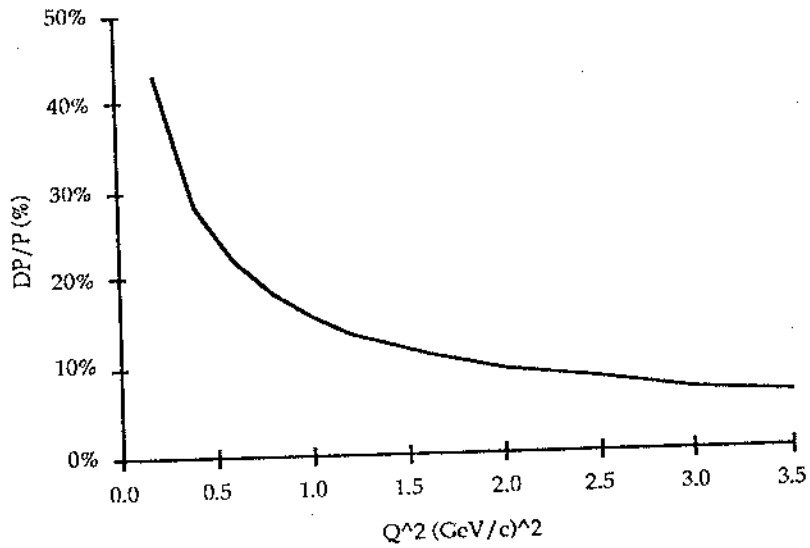

Figure 47. Electron optics: Momentum resolution required to resolve elastic and inelastic scattering.

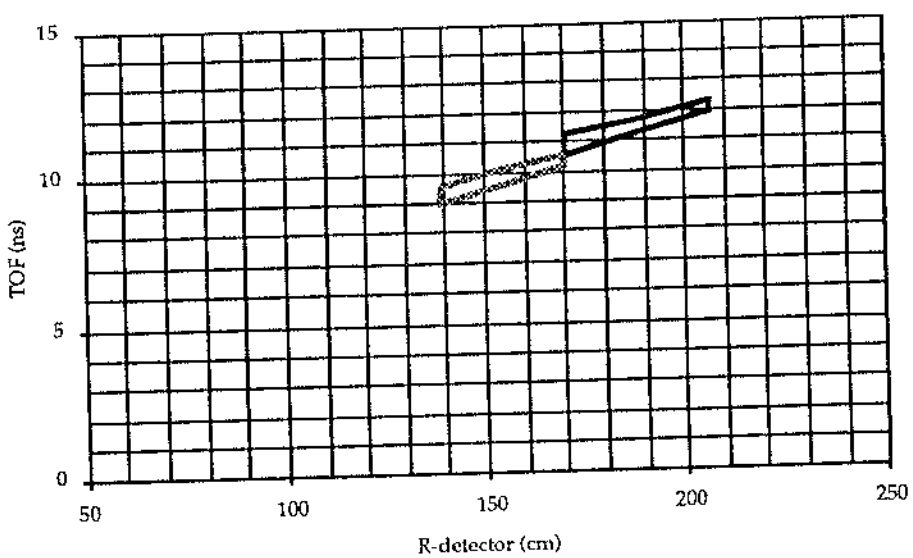

Figure 48. Electron optics: TOF vs. position on the focal surface. Indicated are the envelopes of points corresponding to elastic and threshold-inelastic scattering with $\Delta\theta = 50$ mrad; $Q^2 = 2.0\ GeV^2/c^2$, 20-cm target, full azimuthal acceptance, 90 % of full field.

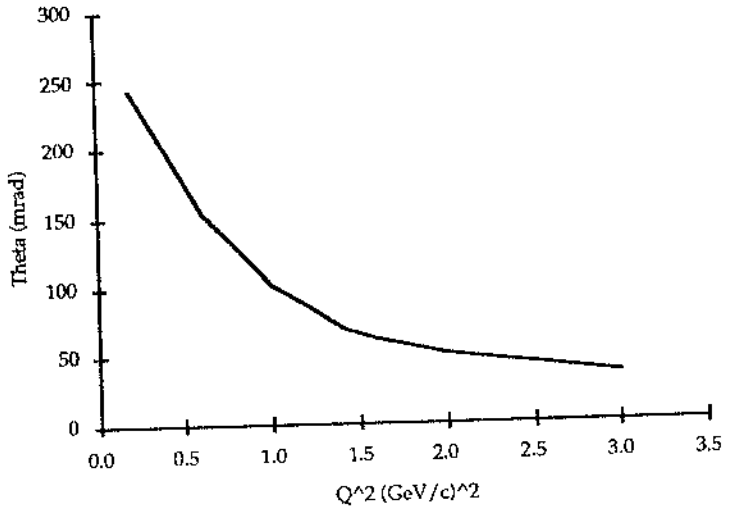

Figure 49. Electron optics: Restriction on scattering-angle (θ) acceptance required to resolve elastic and threshold-inelastic scattering.

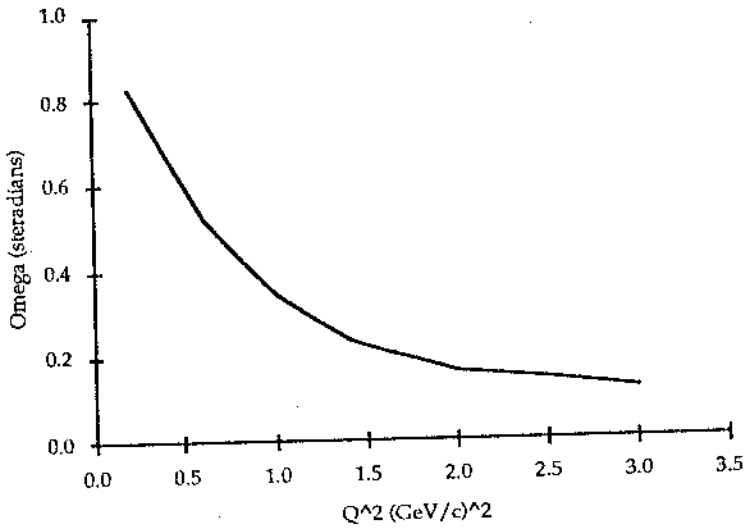

Figure 50. Electron optics: Solid angle corresponding to restricted scattering-angle acceptance of Figure 8.49.

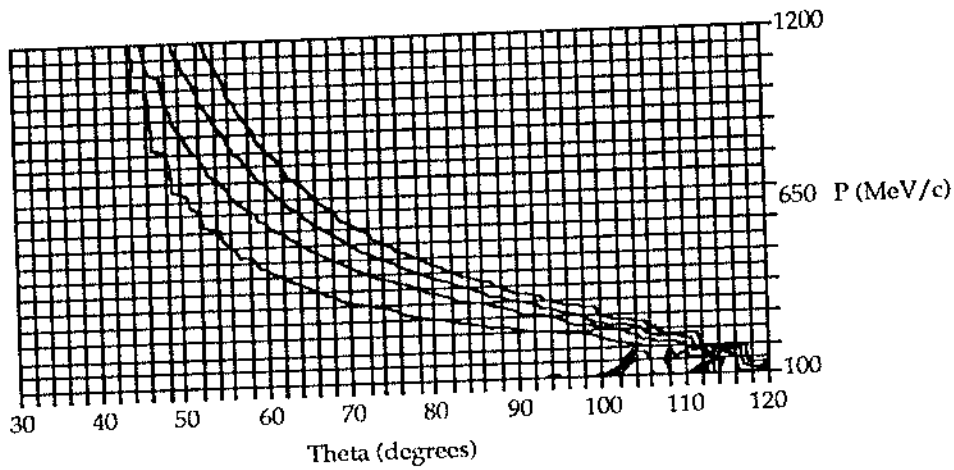

Figure 51. Contour plot indicating the p/θ focal-surface acceptance of the spectrometer detectors with no internal collimation. Contours correspond to R = 100, 150, 200, and 250 cm.

cross section, and how well the scattering-angle acceptance can be restricted by realistic collimation. These issues are examined with Monte Carlo methods in Section 3.3 of [TD93], and it appears that $Q^2 < 3.0\ GeV^2/c^2$ may be reasonable.

3.5. Acceptances and Collimation

The ranges of momenta and the scattering angles of particles that can reach the focal-surface detectors from the target are of real interest for understanding potential background processes. It is important to recognize that although the geometry of this spectrometer appears to be quite open, in fact it will be a straightforward matter to employ collimation in each sector to tightly restrict the kinematic range of particles that hit the focal surface detectors. As a point of reference, Figure 51 shows a contour plot of values of the radial coordinate R, corresponding to the intersection of trajectories with the focal-surface, as a function of the initial p and θ. The contours corresponds to R = 100, 150, 200, and 250 cm, and reflect the actual range of coordinates where the detectors are

located. In the absence of collimation, charged particles with the indicated kinematics could produce signals in the scintillator array. At low momenta, independent of angle, it is not possible for particles to make it to the detectors because of the sweeping effect of the spectrometer fields. At smaller angles, even very high momenta will be precluded because of the location of the detector plane at a relatively large angle (~ 40°) with respect to the target axis. High momenta at large angles pass above the array.

If intercepting collimation is placed inside the spectrometer as illustrated schematically in Figure 52, additional large-momentum small-angle (including line-of-sight) trajectories can be eliminated, as can additional large-angle small-momentum ones. The collimation is located at a waist in the ensemble of extended-target proton trajectories in the kinematic range $0.1 < Q^2 < 0.5\ \mathrm{GeV}^2/c^2$. The plane that defines the orientation of the collimation can be parameterized with the simple expression

$$R = (335.294) - (1.76471)\ Z \qquad \text{(cm)}. \tag{21}$$

Transfer matrix-elements were determined for this plane in the manner described in Section 3.4 for the case of the focal surface. All of the protons of interest pass through a rather small aperture in the collimator plane. This can be seen from Figure 53 which shows an azimuthal (end-on) plot of the points where the protons ($0.1 < Q^2 < 0.5\ \mathrm{GeV}^2/c^2$) intercept the collimator. The points correspond to particles passing from a 20-cm long target into the full azimuthal acceptance of a sector of the spectrometer. It is useful to compare the collimator aperture of Figure 53 with the respective focal-surface plot for the same range of trajectories shown in Figure 40. The kinematic-acceptance of a collimator aperture located between R = 110 and R = 120 cm is plotted in Figure 54. The overlap between the collimator acceptance and that of the focal surface (Figure 51) is indicated by the outlined area in Figure 55, and it can be seen that the combined acceptance tightly brackets the kinematics of the forward-proton measurements (Table 1).

The same general collimation scheme is used to restrict the angular acceptance and provide the required resolution for the backward electron measurements.

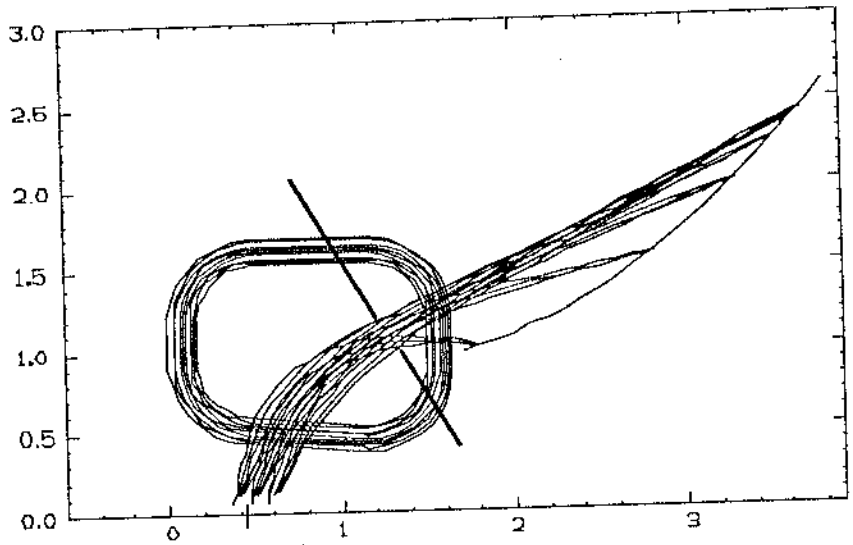

Figure 52. Spectrometer coil section as in Figure 27 indicating the location of the collimation at a waist in the set of proton trajectories.

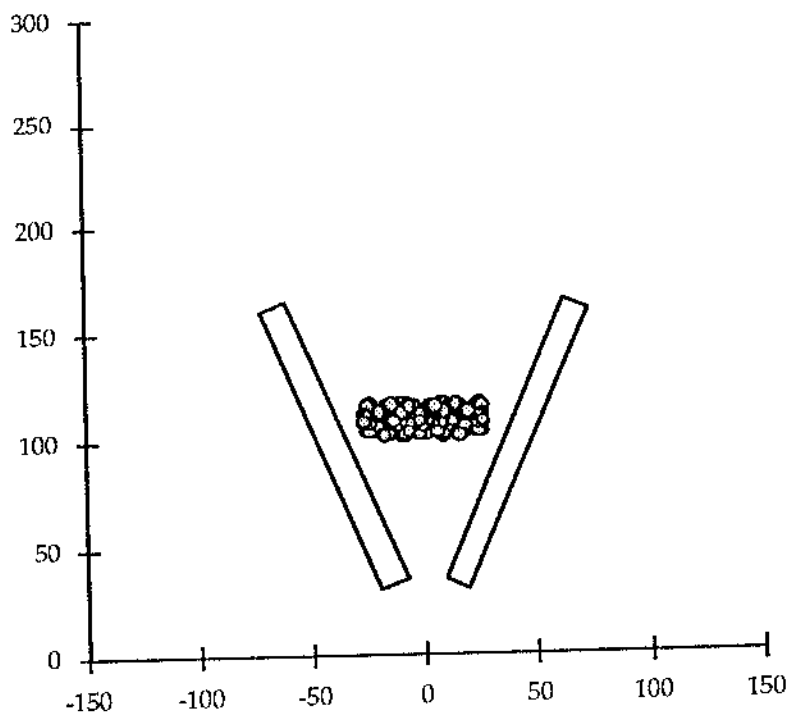

Figure 53. Proton optics: end-on view of the collimator surface of one sector. Points corresponding to $Q^2 = 0.1, 0.2, 0.3, 0.4$, and $0.5\ GeV^2/c^2$ from a 20-cm target, are shown over the full azimuthal acceptance of the spectrometer.

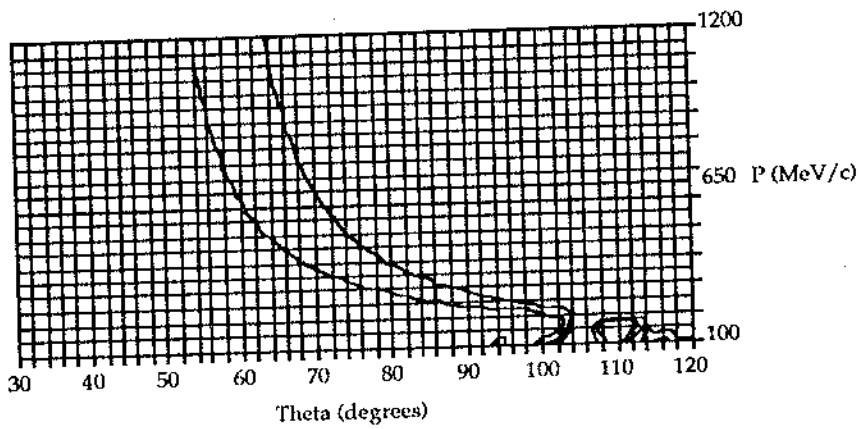

Figure 54. Contour plot indicating the p/θ collimator-surface acceptance of the spectrometer. Contours correspond to R = 110, and 120 cm.

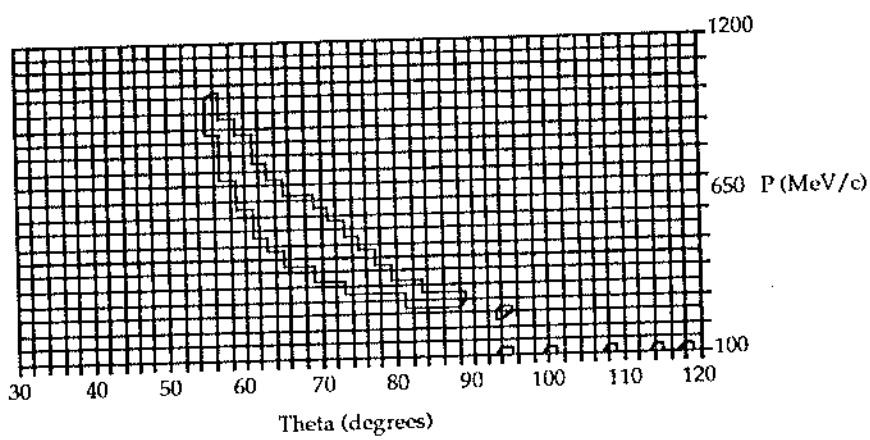

Figure 55. Contour plot indicating the combined p/θ acceptances of the collimator (110 < R < 120 cm) and the focal-surface detectors (100 < R < 250 cm).

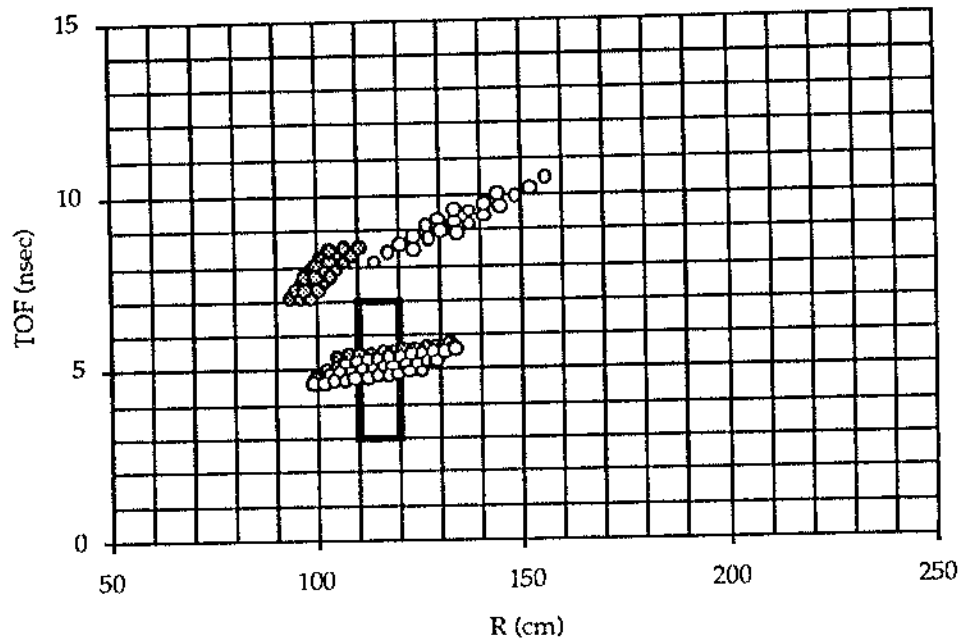

Figure 56. R-T plot of backward electrons that pass through the collimator (black rectangle: 110 < R < 120 cm) and reach the focal surface. Open circles indicate elastic electrons, shaded circles indicate threshold-inelastic. 20-cm target, $Q^2 = 0.6\ GeV^2/c^2$, $\Delta\theta_c \sim 100$ mr.

Figure 56 shows an R-TOF plot of backward elastic and threshold-inelastic electrons, corresponding to $Q^2 \sim 0.6\ GeV^2/c^2$, at both the collimator plane and the focal surface. The elastic electrons are indicated by open circles, and the inelastic by shaded ones. Only those electrons that pass through the collimator aperture at 110 < R < 120 cm are also shown at the focal surface. It can be seen that the elastic scattering is cleanly separated from the inelastic. In this case, particles from the full 20-cm long target were considered, and the scattering-angle acceptance was not otherwise restricted. The particular dimensions of this aperture correspond to a central angular acceptance of $\Delta\theta \sim 100$ mr.

Because the required scattering-angle acceptance changes with the value of backward Q^2 (Figure 49), it is desirable to design the collimator-slit so that the edges can be moved independently.

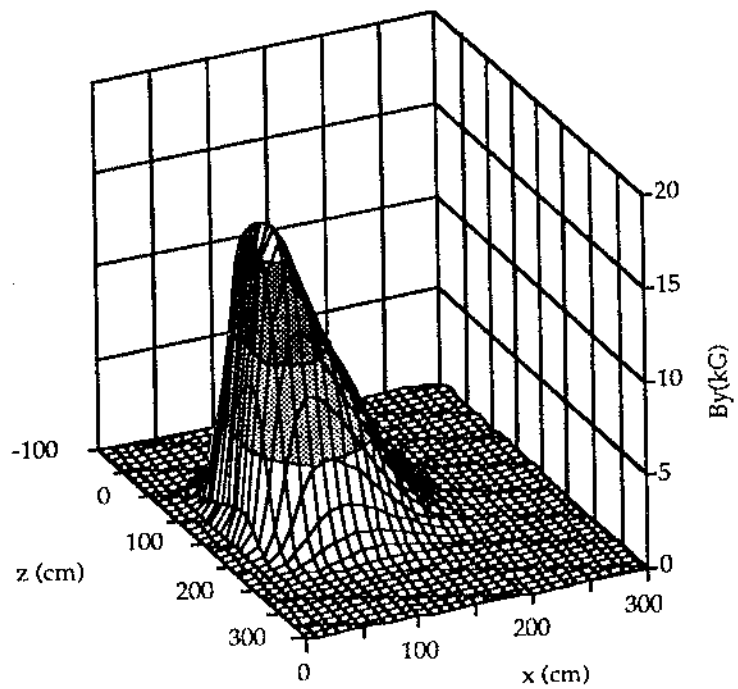

Figure 57. Median-plane magnetic fields B_y.

The quantitative performance of the collimator in defining the backward electron resolution is also examined in Section 3.3 of [TD93].

3.6. Fringe Fields

The extent and distribution of magnetic fringe-fields is of concern because of the effect that stray fields can have on the operation of nearby detectors and other electronic equipment. There are also questions associated with the possibility that structural and other iron in the vicinity of the spectrometer might divert a sufficient amount of flux to distort the particle optics in an asymmetric way. The magnetic fields extend farthest from the spectrometer on the median planes of the sectors between pairs of coils. These median-plane fields are plotted in Figure 57. Because of the symmetry of the spectrometer, there are no magnetic fields along the beam axis. Away from the axis the fields rise rapidly to a peak value of about 1.7 Tesla. For typical particle trajectories BdL ~ 1.6 T-m. The magnetic fields drop rapidly outside the boundaries of the coils. In order to examine this drop-off in more detail, contour lines corresponding to 10, 20, and

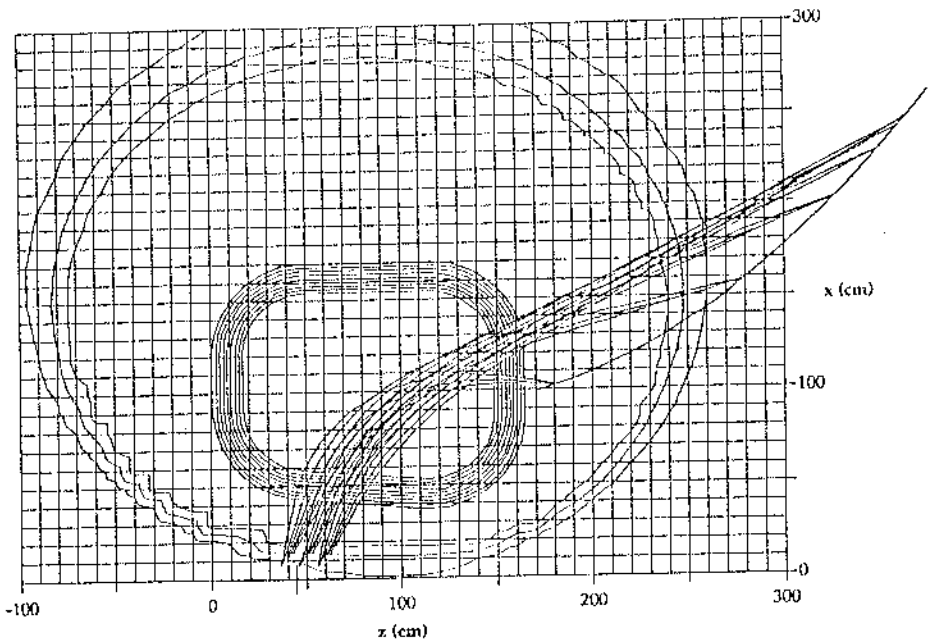

Figure 58. Median-plane fringe-field contours at 10, 20, and 30 Gauss overlaid by the spectrometer profile of Figure 27.

30 Gauss are shown in Figure 58, together with an overlay of the coil profile and the array of proton trajectories. It can be seen that the fields drop to values of order 10 Gauss or less at a radius of 3.0 m. Within this radius all structural components must be made of non-magnetic materials. Light pipes are necessary so that the photo tubes can be kept back of a plane located at about z = 250 cm. The fact that the beam line is situated 4 meters above the floor of the experimental hall means that there is some latitude in the choice of components used to move, support, and align the base of the spectrometer; although we have attempted to keep any iron fixtures at as large a distance as possible. The spectrometer support is discussed in Section 9.10 of [TD93].

3.7. Magnetic Forces

The magnetic forces that act on the coils are an important component in the design of the coil case, the clamping mechanism, and the various support systems that maintain the accurate alignment of the elements of the spectrometer. The limits on deflections and misalignments are discussed in Section 3.8. A

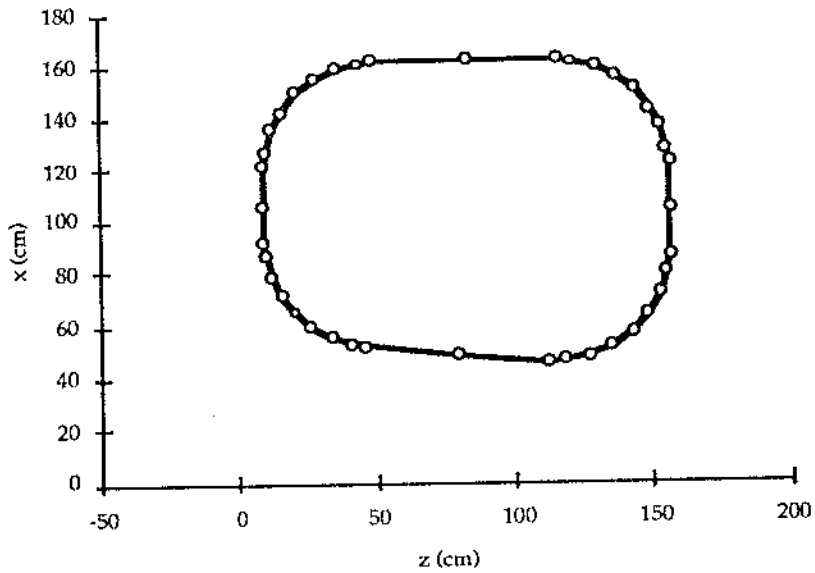

Figure 59. Reference coil-outline indicating the locations of points at which the total resultant magnetic force-per-unit-length acting on the current distribution were computed.

complete ANSYS finite-element analysis of the structural deflections caused by gravity and magnetic interactions was carried out as part of the engineering design effort. The results of this work are reported in [TD93]. Approximate calculations of the magnetic forces acting on the coils were made as part of the optical design and optimization, and are summarized in this section.

Figure 59 shows an outline corresponding to the optimized coil profile of Figure 27. The open points along the perimeter indicate the locations at which the total resultant magnetic force-per-unit-length acting on the current distribution were computed. A plot of the forces acting in the plane of one coil is given in Figure 60. The points correspond to those shown in Figure 59, and all forces act to expand the coil. The largest forces are those on the coil windings that run nearest to the symmetry axis of the toroid. In the symmetric 8-coil spectrometer, the out-of-plane components cancel. Although the coils will be shut down under a fault condition, it is of interest to consider the transverse forces that act on a coil when the current in an adjacent coil is turned off. These forces are indicated by the black points plotted in Figure 61. It can be seen that

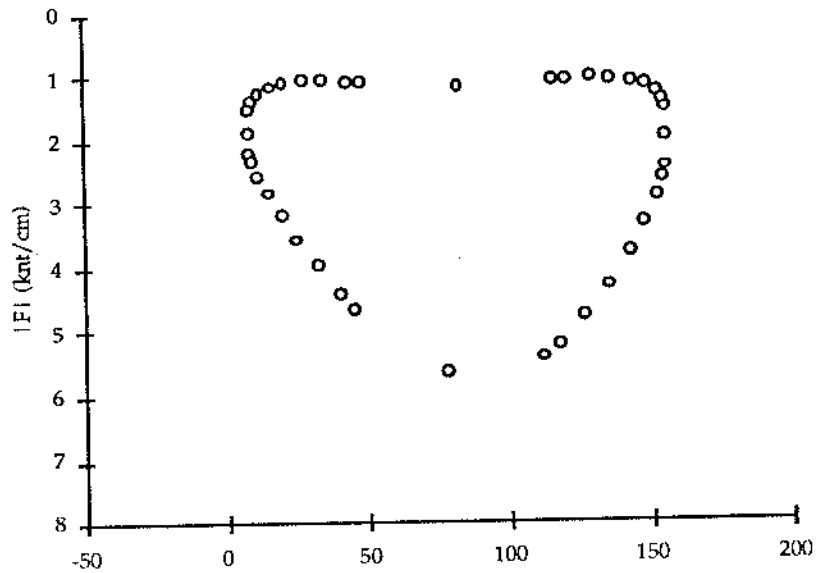

Figure 60. Total resultant magnetic force-per-unit-length acting on the coil current distribution ($|F_{x+z}|$). All forces act to expand the coil. In the symmetric 8-coil spectrometer the out-of-plane forces (F_y) cancel.

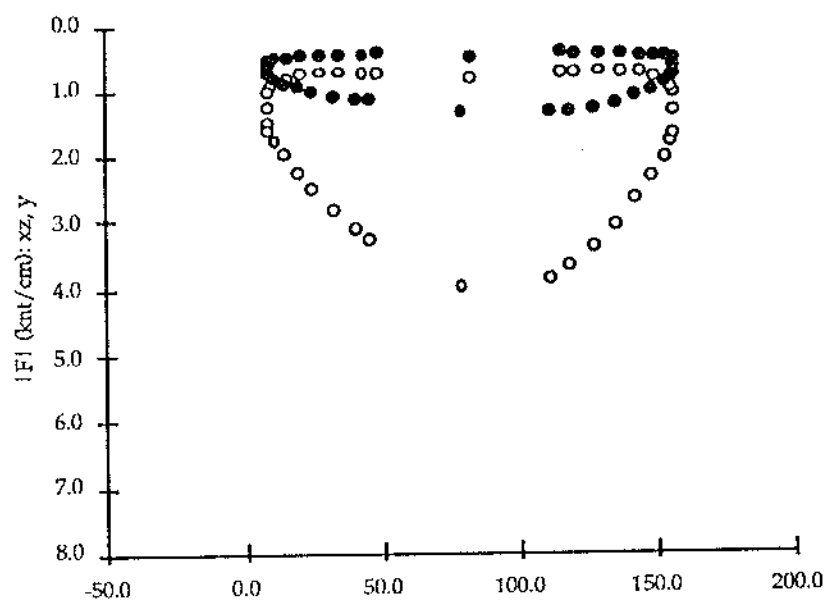

Figure 61. Magnetic force-per-unit-length acting on the current distribution in one of eight coils, with the current in an adjacent coil turned off. The in-plane forces ($|F_{x+z}|$) are indicated by the white points; the out-of-plane forces ($|F_y|$) by the black.

forces of order 1 knt/cm would develop along the inner run of the coil under this condition.

3.8. Alignment and Deflection Tolerances

A realistic evaluation of permissible deviations in the location and orientation of the elements that make up the spectrometer and the detector array is an important part of the design process. We have investigated the question of alignment and deflection tolerances by examining the changes in the focal-surface intersection coordinates for trajectories in a sector of the spectrometer, that arise from changes in the orientation of an adjacent coil. In particular, the derivatives of R with respect to the three translations and three rotations illustrated in Figure 62 were computed for protons with $0.1 < Q^2 < 0.5$ GeV$^2/c^2$ and $0 < \phi < 200$ mrad. The derivatives are plotted in Figures 63 through 68.

One way to establish tolerance limits is to require that uncertainties in the focal-surface coordinate due to misalignments do not exceed the uncertainties that arise from the long scattering target. These latter are plotted in Figure 69. The difficulty with this approach is that the extended target uncertainties are very small over much of the focal surface, and rather tight tolerances result, as can be seen from the first row of Table 17. A better approach is to relate the tolerance limits to a corresponding minimum achievable Q^2-resolution. These tolerances also are listed in Table 17. We note that the Q^2-resolution limit associated with the long target, shown in Figure 41, still tends to dominate at large ϕ and Q^2. The table shows that $\Delta Q^2/Q^2 > 1\%$ requires that the translational uncertainties be of order ± 1 mm, the rotational of order ± 2 mrad, and that the focal-surface coordinates be established at the level of ± 2 mm.

It has been assumed that the tolerances that are maintained in the manufacture of the coils can be kept small enough so that the over-all average location of the conductor can be considerably better than of order ± 1 mm. Small turn -to-turn variations are not very important. This latter point can be verified by considering variations in the linear-filament approximation for the curved sections of the coils that was discussed on Section 3.2. For example, $\theta = 9°$ corresponds to $\Delta_{max} = \pm 0.8$ mm in the location of individual filaments. Over the lengths of the circular arcs, this rather large variation is irregularly distributed relative to the reference ($\theta = 4.5°$), and Table 8 shows that $\Delta R < 1$ mm.

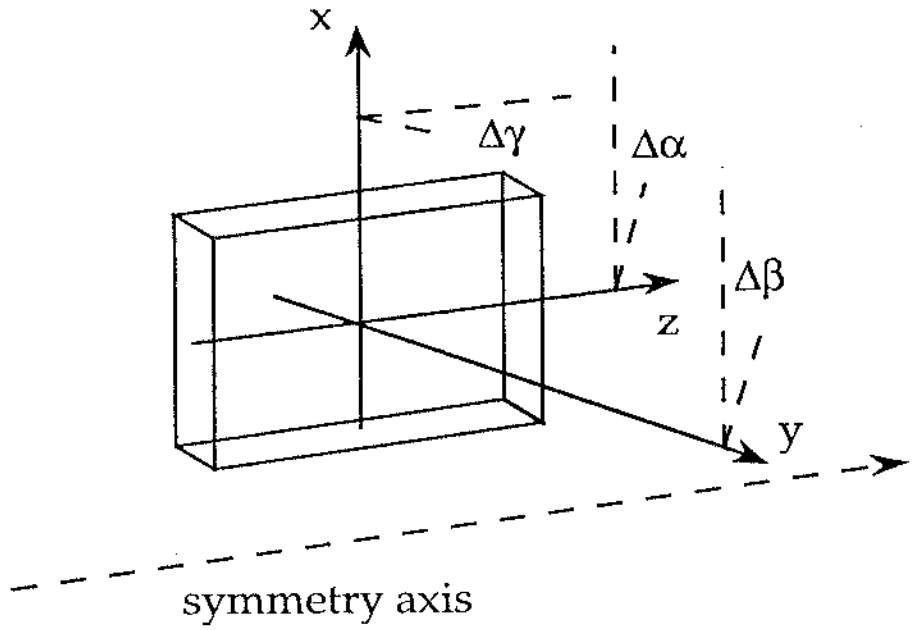

Figure 62. Illustration of the coil translations and rotations considered in the analysis of displacement tolerances.

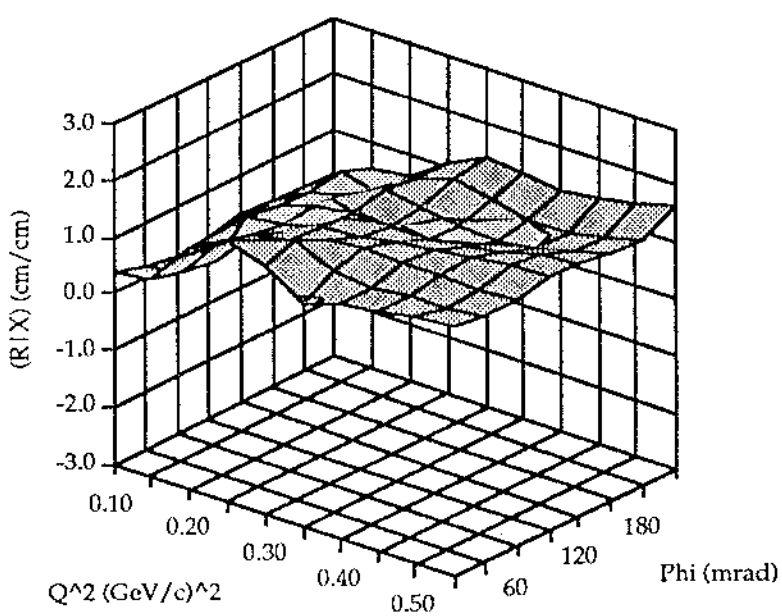

Figure 63. Coil displacement uncertainty: motion along x-axis.

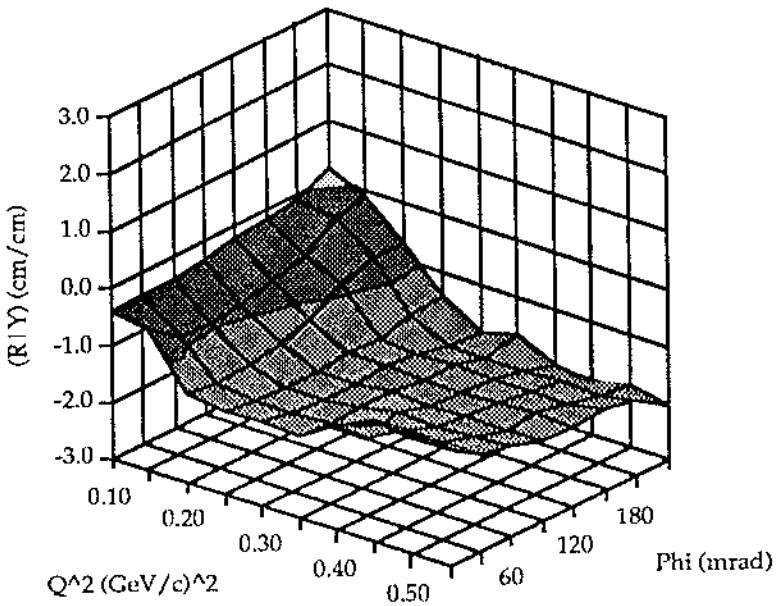

Figure 64. Coil displacement uncertainty: motion along y-axis.

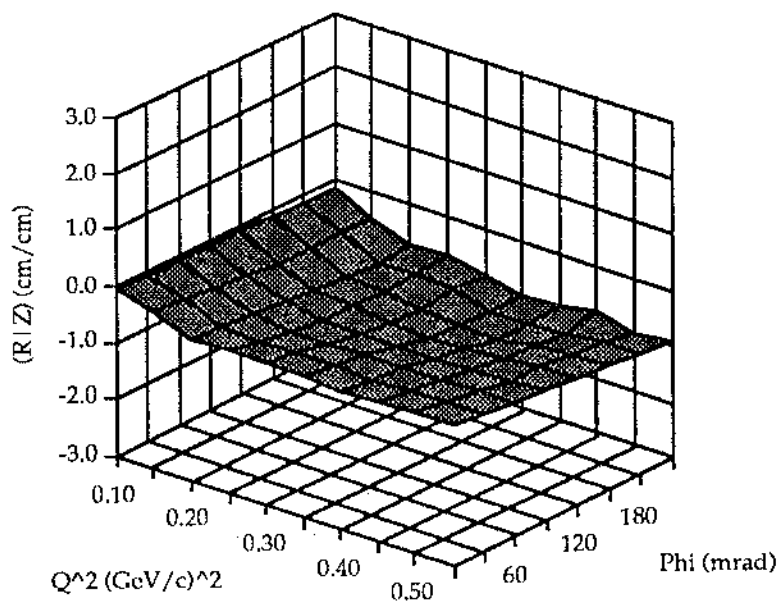

Figure 65. Coil displacement uncertainty: motion along z-axis.

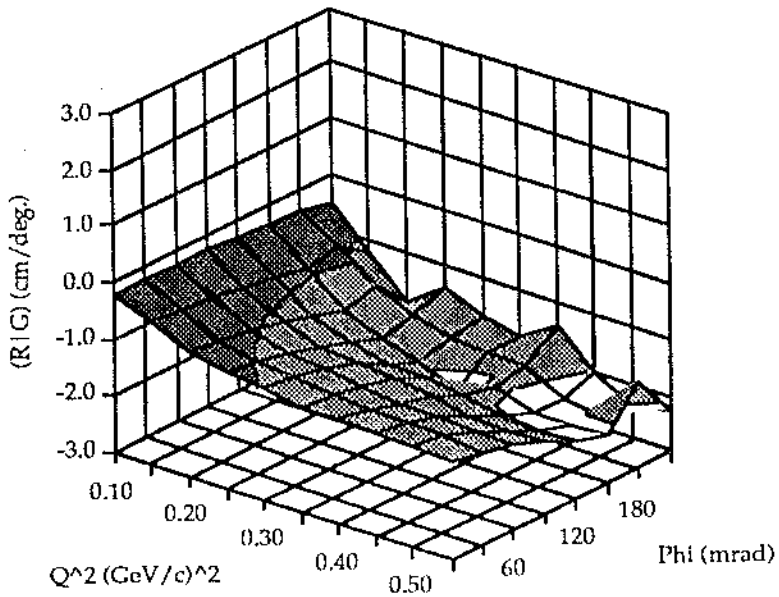

Figure 66. Coil displacement uncertainty: rotation about x-axis (γ).

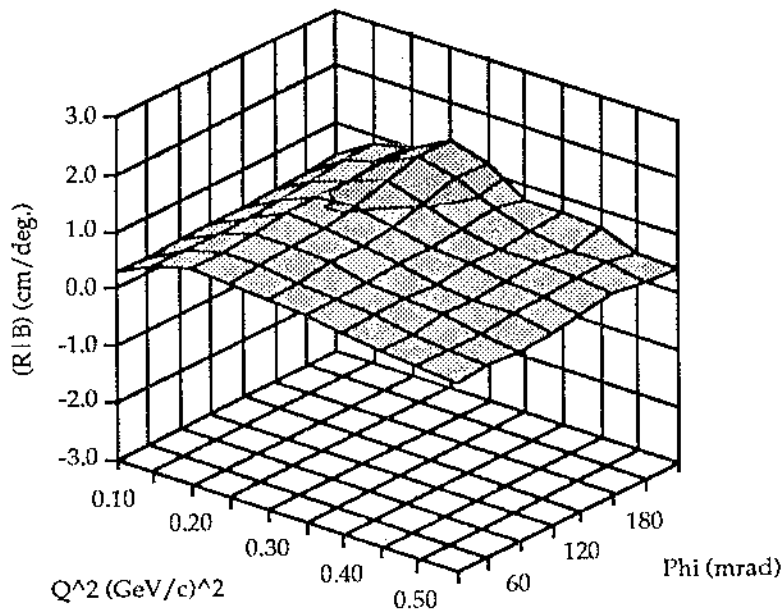

Figure 67. Coil displacement uncertainty: rotation about y-axis (β).

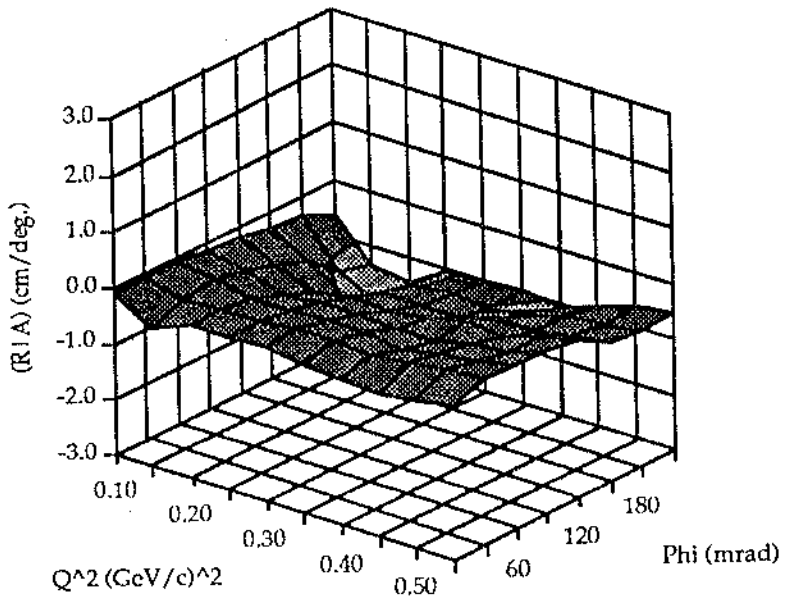

Figure 68. Coil displacement uncertainty: rotation about z-axis (α).

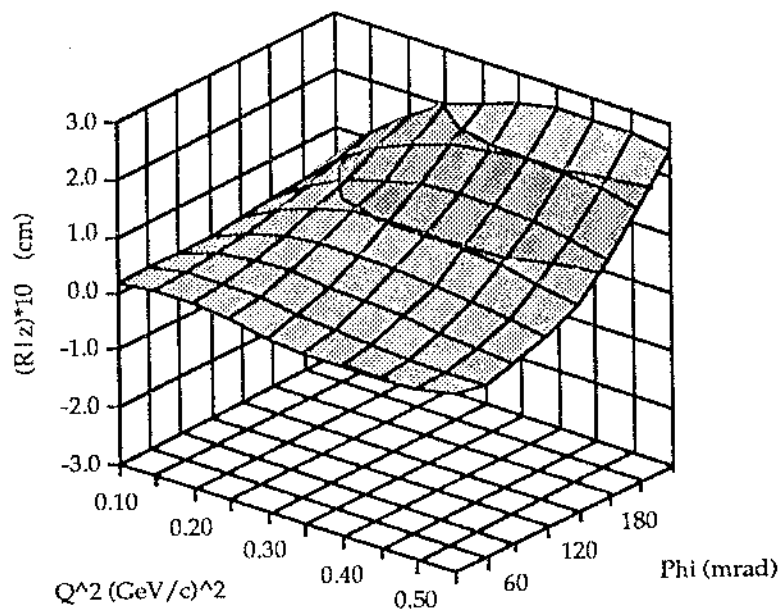

Figure 69. Focal plane radial-position uncertainty due to 20-cm long target.

Table 17. Coil location tolerances.

Minimum dQ^2/Q^2	ΔR (mm)	$\Delta x, \Delta y, \Delta z$ (mm)	$\Delta\alpha, \Delta\beta, \Delta\gamma$ (mrad)
Figure 8.41	Figure 8.68	0.1 mm	0.2 mr
> 5 %	~ 10 mm	5 mm	10 mr
> 2 %	~ 5 mm	3 mm	6 mr
> 1 %	~ 2 mm	1 mm	2 mr

3.9. Beam Motion/Rastering

The electron beam will be moved on the target over an area of about 0.2 cm^2, corresponding to a radius of 0.25 cm. Because the $(R|x)$ matrix elements are very small even at the extremes of the azimuthal acceptance, the x-variation would have to be almost a factor of 8 larger than this in the worst case to generate R and T uncertainties equal to those that arise from the length of the target. This can be seen from Figure 70 which shows the ratio of the uncertainty in the focal-surface coordinate due to beam motion in the x-direction ($\Delta x = 0.25$ cm) to the uncertainty associated with the extended target ($\Delta z = 10$ cm). Notice that the worst case correspond to small angles ϕ at large Q^2 where the magnification denominator (Fig 34) is small. In fact, the absolute variation in R associated with this range of motion in x is everywhere less than about 0.7 mm. The $(R|y)$ matrix elements are bigger than the $(R|x)$ and have a more pronounced ϕ-dependence; but Figure 71 shows that even in the worst case it would still be necessary to have at least twice the anticipated y-variation in order to begin to approach the uncertainties that arise from the extended target. Again, the worst cases corresponds to places where the magnification denominator is small. We conclude that beam motion will not be a limiting factor in the performance this spectrometer.

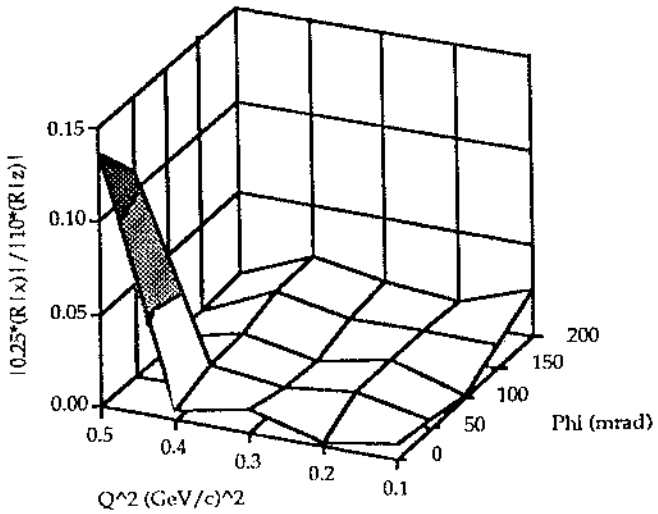

Figure 70. Uncertainty in the focal-surface coordinate due to beam motion in the x-direction ($\Delta x = 0.25$ cm) relative to the uncertainty associated with the extended target ($\Delta z = 10$ cm).

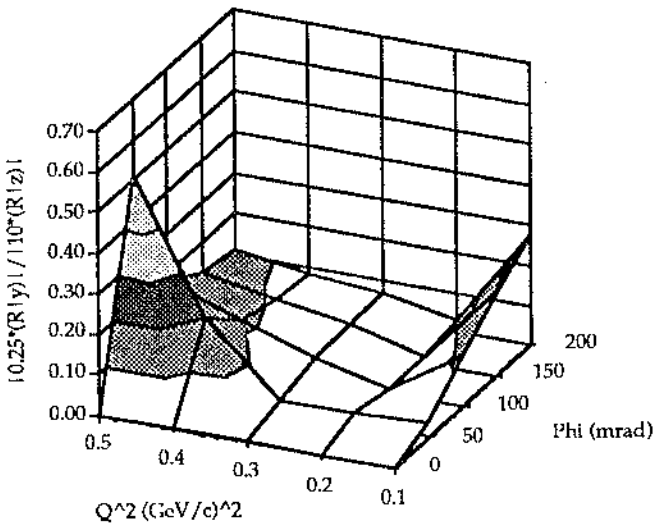

Figure 71. Uncertainty in the focal-surface coordinate due to beam motion in the y-direction ($\Delta y = 0.25$ cm) relative to the uncertainty associated with the extended target ($\Delta z = 10$ cm).

3.10. Current Stability Requirements

The effect of current instabilities on the performance of the device was investigated by means of (X|I) transfer matrix-elements computed from the parameters listed in Table 15. Figure 72 shows a plot of the absolute uncertainty in the focal-plane coordinate corresponding to current variations on the order of $\Delta I/I = \pm 0.01\%$ (10^{-4}). It can be seen that the sensitivity is greatest for the longer trajectories, and that there is little ϕ-dependence. The R-coordinate variation is always less than 0.4 mm. In particular, long-term current variation on the order of 3×10^{-4} would be required to produce uncertainties comparable to those associated with the misalignment tolerances for $\Delta Q^2/Q^2 > 1\%$. (Section 3.8). We note however, that because of the experimental methodology, long-term variations are of secondary importance, and this limit on $\Delta I/I$ is a weak constraint. Short-term variations associated, for example, with power-supply voltage ripple are not a concern because of the large inductance (L ~ 0.33 h) and negligible resistance of the toroid.

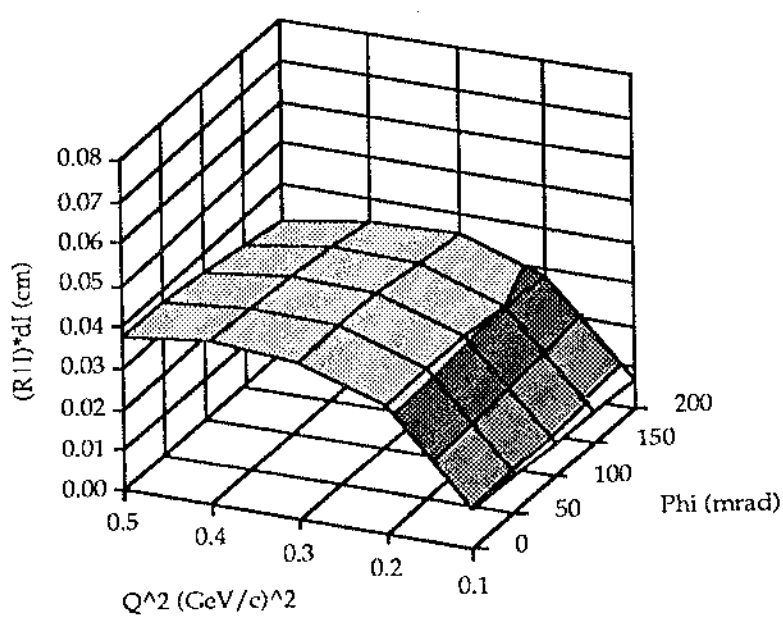

Figure 72. Uncertainty in the focal-surface coordinate due to current variations of order $\Delta I/I = 1 \times 10^{-4}$ (.01 %).

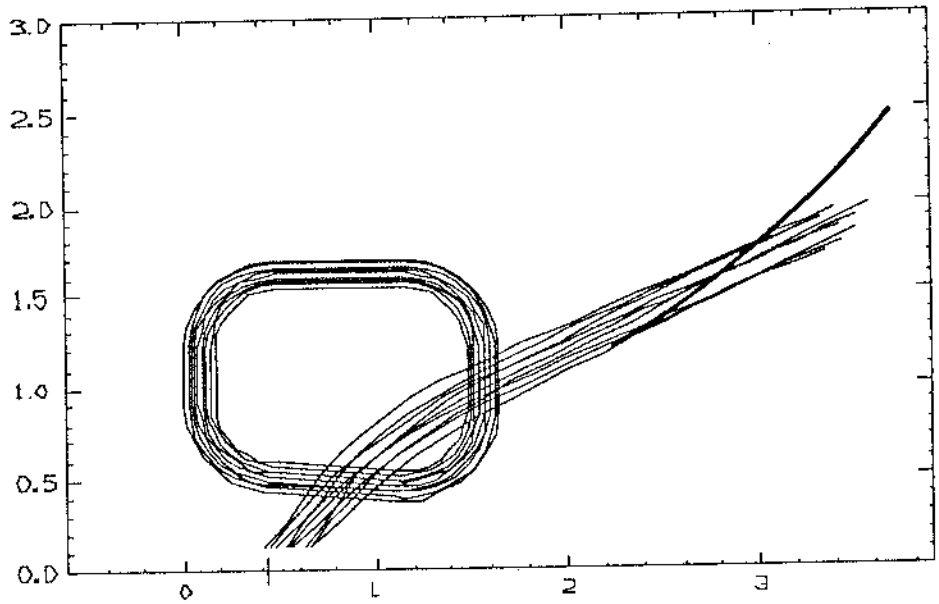

Figure 73. Forward protons: Extended Q^2-range; $E_e = 1.8$ GeV. Trajectories corresponding to $Q^2 = 0.6$, 0.8, and 1.0 GeV^2/c^2 are shown. The location of the upper part of the present focal surface is indicated. Note that the foci for higher-Q^2 rays fall at smaller radii.

3.11. Extended Q^2-range: Forward Protons

An interesting property of the forward proton kinematics is that as Q^2 and the momentum of the proton increase, the scattering angle decreases. This effect tends to limit the Q^2-dispersion at the upper end of the focal surface as can be seen in Figure 37. However, it also implies that for some values of $Q^2 > 0.5$, protons with increasing momentum will be brought back into the higher-field regions of the spectrometer. This is illustrated in Figure 73, which shows trajectories from a 20-cm target corresponding to $Q^2 = 0.6$, 0.8, and 1.0 GeV^2/c^2. The energy of the incident electron-beam has been adjusted to a value of $E_e = 1.8$ GeV in order to have the $Q^2 = 1.0$ trajectories pass through the peak magnetic field. The $(x|x) = 0$ foci are quite good, and fall in the vicinity of the present detector array. Only relatively minor alterations of the instrumentation would be needed to make the high-Q^2 measurements. For this example, line-of-sight shielding is still a possibility, although it would be preferable to have a somewhat greater trajectory bend-angle. This could be accomplished by providing a modest increase in the amount of conductor that is incorporated into the present coil design.

Table 18. G^o Spectrometer Summary

(G^o_E and G^o_M Separation: $0.1 < Q^2 < 0.5$ GeV^2)

• Configuration:	Super-conducting Toroid (Iron-free)
• Number of coils:	8 (in Common cryostat)
• Turns/coil:	144 (4 x 36 windings)
• Superconductor:	NbTi: 20 strand Rutherford cable
• Conductor section (Cu):	0.5 x 2.0 cm (1.0 cm^2)
• Cu : NbTi	1.8 : 1
• Conductor insulation:	0.1 mm Kapton (half lapped)
• Operating current:	5 kA
• Operating temperature:	4.5 K
• Peak Field at conductor:	~ 3 T
• Conductor length/coil:	~ 670 m
• NI_{tot}:	5.76 MA-turns
• Total Inductance:	0.328 h
• Total Stored Energy:	4.3 MJ
• Optics:	$(x \mid t) = 0$ (zero magnification)
• Central Momentum:	560 MeV/c @ $\theta = 69°$
• P_{max}:	800 MeV/c @ $\theta = 61°$
• Trajectory bend-angle:	$35° < \theta_{bend} < 87°$
• Magnetic field:	$\int B \cdot dL$ ~ 1.6 Tesla-meter
• Resolution:	$1\% < \Delta Q^2/Q^2 < 10\%$
• Φ acceptance:	$\Delta\Phi$ ~ 57% of 2π
• Solid angle	
protons:	$\Delta\Omega$ ~ 945 mstr.
electrons:	$800 > \Delta\Omega > 550$ mstr.

4. Summary

In this report we have presented our reasons for concluding that a superconducting zero-magnification toroidal spectrometer is the best device for pursuing the proposed G^0 measurements. The considerations that entered into the performance and cost optimization of this device were also discussed in detail. For reference, some of the more important optical and physical characteristics of the G^0 spectrometer are summarized in Table 18. We emphasize that, in addition to being an optimal instrument for the proposed separation of G^0_E and G^0_M in the range $0.1 < Q^2 < 0.5$ GeV^2, this spectrometer has the capability of extending the backward-electron measurements to $Q^2 \sim 3.0$. With some modification of the detector array, the forward proton measurements might be extended above $Q^2 \sim 1.0$.

5. References

[BL91] A Proposal for the Bates Large Acceptance Spectrometer Toroid. Proposal to MIT/Bates. (5 March, 1991).

[CD90] CEBAF Conceptual Design Report (13 April, 1990).

[La91a] R. M. Laszewski. Status of Parity-Detector Design Studies. UIUC/NPL Technical Report 91-01 (29 January, 1991).

[La91b] R. M. Laszewski. Out-of-Plane Physics and the G^0 Spectrometer. UIUC/NPL Technical Report 91-04 (5 September, 1991).

[La92] R. M. Laszewski. G^0 Spectrometer Reference Optical-Design Optimization. UIUC/NPL Technical Report 92-02 (24 September, 1992).

[PR92] "G^0": Measurement of the Flavor Singlet Form Factors of the Proton. Proposal to CEBAF, PR91-017 (Revised 19 June, 1992).

[ST89] STAR: A Multipurpose Spectrometer System for CEBAF. Progress Report, October 1989 (revised). UIUC/NPL Technical Report 89-68, (1989).

[TD93] G^0 Technical Design Report. UIUC/NPL Technical Report 93-01 (November, 1993).